The Pennsylvania State University

The Graduate School

Department of Energy and Geo-Environmental Engineering

HISTORY DEPENDENT MODELING OF COUNTER-CURRENT FLOW IN POROUS MEDIA

A Thesis in

Petroleum and Natural Gas Engineering

by

Gaoming Li

Submitted in Partial Fulfillment

of the Requirements

for the Degree of

Doctor of Philosophy

May 2003

We approve the thesis of Gaoming Li.

Date of Signature

Abraham S. Grader Professor of Petroleum and Natural Gas Engineering Thesis Co-Advisor Chair of Committee	
Phillip M. Halleck Associate Professor of Petroleum and Natural Gas Engineering Thesis Co-Advisor	
Turgay Ertekin Professor of Petroleum and Natural Gas Engineering George E. Trimble Chair in Earth and Mineral Sciences Chair of Petroleum and Natural Gas Engineering	
Derek Elsworth Professor of Energy and Geo-Environmental Engineering	
Michael A. Adewumi Professor of Petroleum and Natural Gas Engineering Quentin E. and Louise L. Wood Faculty Fellow Graduate Program Officer of Petroleum and Natural Gas Engineering	

Abstract

Gravity-driven counter-current flow occurs in reservoir processes such as gas storage in an aquifer and certain secondary and tertiary recovery processes. In order to operate these processes effectively, it is important to understand and to be able to model the flow process. Both drainage and imbibition processes exist simultaneously when counter-current flow occurs. It has been difficult to model this type of flow process because of the impossibility of assigning a single capillary pressure curve applicable over the entire sample in this situation. The focus of this study is to find a method for accurately representing capillary pressure in counter-current flow.

Gravity-driven counter-current flow experiments have been done in glass bead packs and the spatial and temporal saturation distributions of the core sample obtained with X-ray computed tomography (CT). With the aid of a deterministic reservoir simulator, capillary pressure and relative permeabilities were extracted by matching the saturation distribution with optimization methods (history-matching). This work applies a saturation-history-dependent approach to simulating counter-current flow. From the capillary hysteresis loop, a family of curves (called scanning curves) is constructed connecting the two branches. Each grid block of the sample is assigned a different scanning curve according to its current saturation and saturation history.

This technique was used to simulate previous laboratory experiments in glass bead packs. The simulation reproduced two-dimensional saturation distributions over time with good accuracy. Similar simulations of experiments described in the literature were equally successful. In particular the simulation captured the fluid banks observed in counter-current flow experiments, which cannot be obtained through other methods.

TABLE OF CONTENTS

LIST OF FIGURES

LIST OF TABLES

NOMENCLATURE

ROMAN

D = gradient vector of the objective function

E = energy

G = sensitivity coefficient matrix

H = Hessian matrix

I = attenuation intensity

J = objective function

k = permeability, Darcy

k_r = relative permeability

L = length, ft

p = pressure, psia

q = flow rate

R = Radius of curvature

r_c = Radius of capillary tube

s = saturation

v = flow velocity

X = unknown vector

Z = atomic number

GREEK

γ = interfacial tension

μ = viscosity, cp; attenuation coefficient

ϕ = porosity, fraction

ρ = density, lbm/ft^3

SUBSCRIPTS

abs = absolute

avg = average

b = bulk

ba = benzyl alcohol

c = capillary

d = decane

m = length, ft; rock matrix

f = fluid

nw = non-wetting phase

o = oil

w = water; wetting phase

g = gas

r = residual

SUPERSCRIPTS

calc = simulation result

d = drainage

exp = experiment

i = imbibition

ABBREVIATIONS

CT = Computed Tomography

BA = benzyl alcohol

D = decane

Pc = capillary pressure

W = water

ACKNOWLEDGEMENTS

I would like to express my sincere appreciation and gratitude to my thesis advisors Dr. Abraham S. Grader and Dr. Phillip M. Halleck for their valuable assistance and guidance during this study. I also thank Dr. Turgay Ertekin, Dr. Derek Elsworth, and Dr. Michael A. Adewumi for their participation in my thesis committee and for their comments and suggestions. Appreciation is extended to all my friends and graduate student colleagues for their useful discussion and encouragement.

I am deeply indebted to my wife Xiuli Dong and all my family members for their constant love, support and understanding.

I gratefully acknowledge the financial support from the Energy Institute of the Pennsylvania State University and DOE for this work.

CHAPTER 1

INTRODUCTION

Petroleum engineers design and optimize hydrocarbon recovery processes. The production of petroleum reservoirs by primary, secondary, or tertiary processes involves the simultaneous flow of two or more fluids. Multiphase flow occurs during water or gas drive and some enhanced oil recovery (EOR) processes such as in-situ combustion and carbon dioxide flooding. Reservoir engineering designs, oil recovery predictions, and evaluation of enhanced oil recovery processes require knowledge of relative permeabilities, and capillary pressure. With the development of new recovery techniques, the interest in determining relative permeabilities and capillary pressures has intensified.

Gravitational, capillary, and viscous forces play an important role in hydrocarbon recovery processes. When the gravitational force is much larger than viscous force, counter-current flow may occur (Walsh and Moon, 1991). The possible occasions for counter-current flow include primary and secondary migration of hydrocarbons, gas storage in an aquifer, steam-assisted gravity drainage processes, and some enhanced oil recovery processes. Many researchers (Briggs and Katz 1966, Templeton et al. 1962, Barbu et al. 1999, Karpyn 2001, Al-Wadahi et al. 2000) have done some experiments and simulation of gravity driven counter-current flow.

In a closed system, both drainage and imbibition occur at the same time in different locations during counter-current flow. The question that arises is: which capillary pressure curve should be used in the simulation of such a process? If both

capillary pressure curves are used, there will be a saturation and capillary discontinuity in the transition zone. The goal of this work is to find an answer to this question faced in modeling counter-current flow and hence to provide a mechanistic understanding of counter-current flow. The factors that favor the formation of fluid banks during counter-current flow are also studied.

1.1 Fluid Flow in Porous Media

Hydrocarbons are generated, migrated and stored in porous and permeable media. Several mechanisms of fluid flow through porous media govern migration and production processes. The primary mechanism is the flow under pressure gradient. Darcy equation is used to describe the laminar viscous flow driven by this mechanism. Ignoring the gravity effect, the equation is represented as,

$$v = -\frac{k}{\mu}\frac{dp}{dx} \tag{1.1}$$

where k is absolute permeability representing the conductivity of the porous medium, μ is the fluid viscosity. The velocity v is proportional to the pressure gradient dp/dx. The negative sign is because the flow direction is opposite to the increasing pressure direction.

If multiple fluids flow simultaneously in the porous medium, a modified Darcy equation is applied to each fluid in the following form:

$$v_i = -\frac{kk_{ri}}{\mu_i}\frac{dp_i}{dx} \tag{1.2}$$

where k_{ri} is the relative permeability, which can be viewed as a modification factor for multiphase flow.

The combination of Darcy equation, which represents the momentum conservation, and the mass continuum equation in porous media form the basis of reservoir simulation and other reservoir engineering problems.

Multiple fluids co-exist in reservoir rocks, so multiphase flow is of great importance for oil recovery processes including primary, secondary and tertiary recovery

stages. In secondary and tertiary recovery processes, injection of another fluid is often implemented to produce the remaining hydrocarbons in the reservoir left by the previous recovery stage. The base for the displacement calculation with two phases is the frontal displacement theory introduced by Buckley-Leverret (1942) and expanded by Welge (1950). This theory has been extended to three-phase problems by Grader and O'Meara (1988).

In the past, the investigation of multiphase flow was mainly done in laboratories with the assumption that the core samples are homogeneous. With the development of some advanced visualization techniques, such as X-ray CT, experiments in multiphase flow have been greatly improved. The above assumption either can be confirmed or be eliminated with the aid of high quality images and information obtained from the image analysis.

The recent multiphase flow study has been extended to the micro-scale or pore scale modeling and experiments. The interactions between fluids and pore structures can be observed in experiments and many macro-scale phenomena have been successfully modeled at the pore scale. The pore scale modeling and experiments will yield a better understanding of the physical aspect of multiphase flow.

1.2 Relative Permeability

The standard description of multiphase flow in porous media is based on the generalization of Darcy equation, which is rigorous for the flow of a single fluid in porous media. Wyckoff and Botset (1936) introduced a permeability reduction factor for each fluid, called relative permeability in multiphase flow conditions. The heuristic interpretation for the reduction of permeability is that the available channel of a fluid is reduced with introducing another fluid in the porous medium. The interactions such as viscous drag between fluids also contribute to this reduction. Knowledge of relative permeability is important in predicting flow behavior of different fluids in porous media. Two categories of methods have been widely used for measuring relative permeabilities in laboratory: the steady-state method and the unsteady-state method. A third method is the centrifuge technique, which is not commonly used. In the steady-state method, fluids are injected into the core sample at a fixed fractional flow until steady-state conditions are obtained. The relative permeabilities are calculated with the generalized Darcy equation if the pressure drop, flow rate and other properties of the core (such as absolute permeability) and fluids (such as viscosity) are known. The unsteady-state method was developed by Welge (1952) and Johnson et al. (1959), often called Welge-JBN method. In this method, the Buckley-Leverett (B-L) theory (Buckley and Leverett 1942) is applied to calculate the relative permeability. In order to accurately determine relative permeability from experimental data, many empirical or theoretical models or correlations were proposed, such as Corey model (Corey, 1956) and stone model (Stone, 1973). Grader and O'Meara (1988) extended Welge-JBN method from two-phase to three-phase flow and Siddiqui et al. (1996) verified this method experimentally.

Nowadays, with the development of numerical simulators, automatic history matching has been widely used for determining relative permeabilities from experimental data.

1.3 Capillary Pressure

In dealing with multiphase processes, it is necessary to consider the effect of the forces acting at the interface when two immiscible fluids are in contact. In this case, the fluids are separated by a well-defined interface with a few molecular diameters in thickness. At the interface, molecules are surrounded by different type of molecules, so the forces acting on it are not balanced. The unbalanced forces create a membrane-like surface (Amyx 1960). The free surface energy may be defined as the work necessary to create a unit area of new surface. The origin of this work is that, when the surface is extended, molecules must be brought from the interior to the surface against the inward attractive forces. This free energy in the surface is of fundamental importance to many problems relating to the equilibrium of surface. Surface tension is just a simplified mathematical representation of free surface energy (Adam 1941). Interfacial tension is used for the interactions between two general fluids instead of surface tension, which specifically refers to the interface of air and another fluid.

An important consequence of the existence of free surface energy is capillarity. If a liquid surface were curved, the pressure is greater on the concave side than on the convex side by an amount, which depends on the interfacial tension and on the curvature (R). This is because the displacement of a curved surface results in an increase in area as the surface moves towards the convex side, and work has to be done to increase the area. This work is supplied by the pressure difference (capillary pressure) moving the surface (Adam 1941).

Capillary rise phenomenon has been known for a long time, but the physical explanation was not on the right track until 1743 when Clairaut explained it with the

attractions between particles of fluids and solid. The mathematical representation of capillary pressure was derived in 1800s by Young, Laplace, Gauss, and Poisson, which is known as Young or Laplace equation:

$$p_c = \sigma\left(\frac{1}{R_1}+\frac{1}{R_2}\right)$$

where $p_c = p_1 - p_2$, is the capillary pressure, defined as the pressure difference between the non-wetting phase and the wetting phase; σ is the interfacial tension; R_1 and R_2 are the radii of the two principle curvatures. The capillary pressure in a capillary tube is reduced as follows:

$$p_c = \frac{2\sigma\cos\theta}{r_c}$$

where θ is the contact angle and $\boldsymbol{r_c}$ is the inner radius of the capillary tube.

The study of capillary phenomena in porous media was initiated by Washburn (1921). The pioneering work in measuring the capillary pressure in petroleum engineering was done by Leverett (1941). Capillary pressure in a reservoir is a function of properties of rocks and fluids, the saturation of each fluid, the pore size distribution, and even the saturation history. In his study, Leverett determined the capillary curve from height-saturation experiments with a clean unconsolidated sand pack in a tube. He also proposed a method of correlating capillary pressure data for a reservoir, called the *J*-Leverett function. Other commonly used methods for measuring capillary pressure include mercury injection and centrifuge methods.

The saturation dependence of capillary pressure (capillary hysteresis) has been observed for a long time. Morrow and Harris (1965) studied the characteristics of

capillary hysteresis with a modified suction potential technique, which is consistent with Everett's independent domain theory of permanent hysteresis (Morrow 1970). In many oil recovery processes such as water alternating gas (WAG) process, only the drainage and imbibition capillary pressure curves are not enough to describe the process and the intermediate scanning curves are required to correctly model them. However, it is difficult to routinely measure capillary pressure loops and their intermediate scanning curves. Many investigators (Killough 1976, Tan 1990, and Kleppe et al. 1997) came up with some mathematical representations of capillary scanning curves, which can be conveniently applied in reservoir modeling.

1.4 Gravity-Driven Counter-Current Flow

Counter-current flow, which is different from co-current in that fluids flow in opposite directions, might occur in many reservoir processes, such as primary and secondary migration of hydrocarbons, gas storage in an aquifer, steam-assisted gravity (SAGD) drainage process and some secondary and tertiary recovery processes. Counter-current flow driven by spontaneous imbibition has been of interest in fractured systems during water flooding. Several investigators studied this subject (Mattax and Kyte 1962, Blair 1964, Bourblaux and Kalaydjian 1990, and Babadagli 2000). The focus of this work is gravity-driven counter-current flow.

Gravity drainage is a recovery process, in which gravity is the dominating driving force. It is an effective oil recovery process under favorable conditions: high vertical permeability, an favorable oil relative permeability, high vertical continuity, a large density deference, low oil viscosity, and long oil drainage times after the region has been invaded (Richardson 1989). The importance of the gravity force in oil recovery has been recognized since the 1940s. The first theoretical treatment of vertical oil segregation was presented by Cardwell and Parsons (1949) using Darcy equation and the continuity equation. In their calculation, capillary pressure is ignored. Terwilliger et al. (1951) implemented Buckley-Leverett immiscible displacement theory on gravity drainage, which showed a close match to the experiments with steady-state relative permeability and static capillary pressure. Their experiments showed that the recovery is inversely proportional to rate. King and Stiles (1970) reported a very high displacement efficiency (87%) and Dumore and Schols (1974) discovered a very low residual oil saturation (5%) by gravity drainage. Hagoort (1980) studied the recovery performance by gravity

drainage. He found that gravity drainage in water wet reservoirs at connate water saturation can be a very effective oil-recovery process and the oil relative permeabilities are the key factors in this process.

Gravity driven counter-current flow in a closed system was first theoretically studied by Fayers and Sheldon (1959) and Sheldon et al. (1959). They extended the Buckley-Leverret theory for this special case, which has a zero total flow rate and infinite fractional flow. The actual flow rate was used instead of the fractional flow. Templeton et al. (1962) did an experimental study and attempted to predict saturation changes with the above-mentioned extended Buckley-Leverret theory using final saturation profile as the capillary pressure curve. They encountered difficulties in the calculation because of the lack of knowledge of drainage and imbibition capillary pressures and relative permeabilities. Briggs et al. (1966) conducted gravity driven counter-current flow experiments in a closed system in an attempt to describe gas storage in aquifers and they also numerically simulated this process. In the development of a gas storage aquifer field, gas preferentially moves into high permeability layers after it is injected into a reservoir through injection wells. Later on, water above the gas layer moves down due to the gravity force and gas counter-currently moves up. **Figure 1.1** shows the development of gas bubbles in an aquifer (from Briggs et al. 1966). The mechanistic understanding of this counter-current flow process will help reservoir engineers to estimate how long it takes to form gas bubble, which, in turn, help plan efficient gas storage operations. A more recent study by Walsh and Moon (1991) investigated counter-current flow in dipping reservoirs during water or gas injection. Several authors have noticed counter-current flow process in steam-assisted-gravity drainage (SAGD) process (Mokrys and Butler 1993, Das and

Butler 1996, Nasr et al. 2000) and the corresponding improved method - VAPEX process (Mokrys and Butler, 1993). Both are effective methods to improve the heavy oil recovery.

Recently, several experiments in counter-current flow have been done by Barbu et al. (1999) and Karpyn (2001). Al-Wadahi et al. (2000) extracted relative permeabilities and capillary pressure from Barbu's experiments using neuro-simulation modeling. He concluded that the relative permeabilities counter-current flow are smaller than that of the co-current flow and the capillary pressure is similar to the final saturation profile, which is an S-shaped curve.

Figure 1.2 shows the schematic saturation profiles in the vertical position of a counter-current flow process started from an evenly distributed saturation. Initially, the heavy wetting phase is at the top and the light non-wetting phase is at the bottom. Because of the density difference, the upper part undergoes a drainage process with decreasing wetting phase saturation and lower part undergoes an imbibition process with increasing wetting phase saturation. If both imbibition and drainage capillary pressure curves are used for the lower and the upper parts respectively, there will be a discontinuity in the transition zone. This research provides an approach based on saturation history to eliminate this discontinuity.

In Briggs and Katz (1966) and Karpyn (2001) experiments, the formation of fluid banks was reported. **Figure 1.3** shows a typical fluid bank in a schematic counter-current flow process. The mechanism of the formation of these banks and the influence of these banks on the counter-current flow process is discussed in this work.

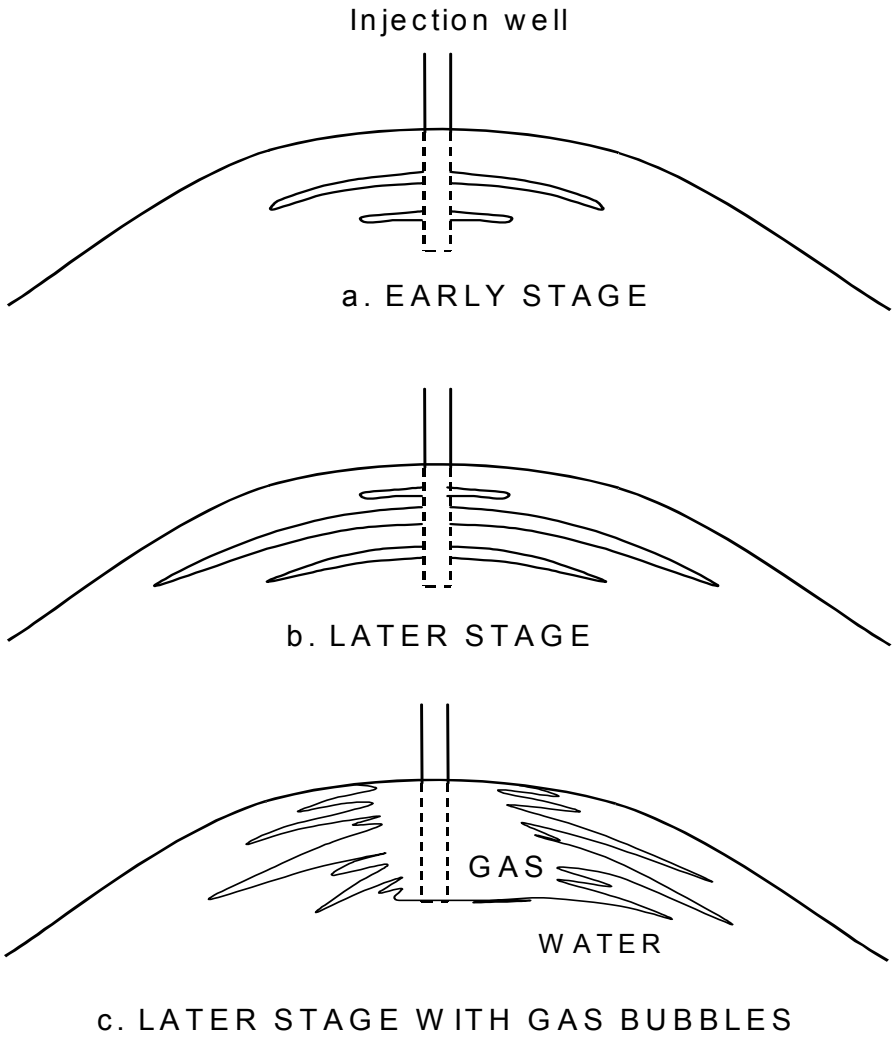

Figure 1.1: Development of gas bubbles in an aquifer (from Briggs et al. 1966).

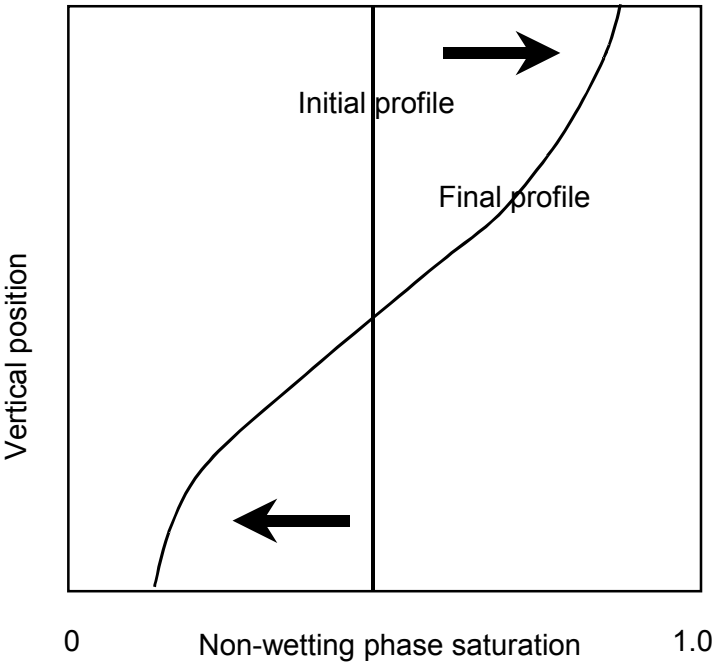

Figure 1.2: The schematic of saturation changing path in a counter-current flow process.

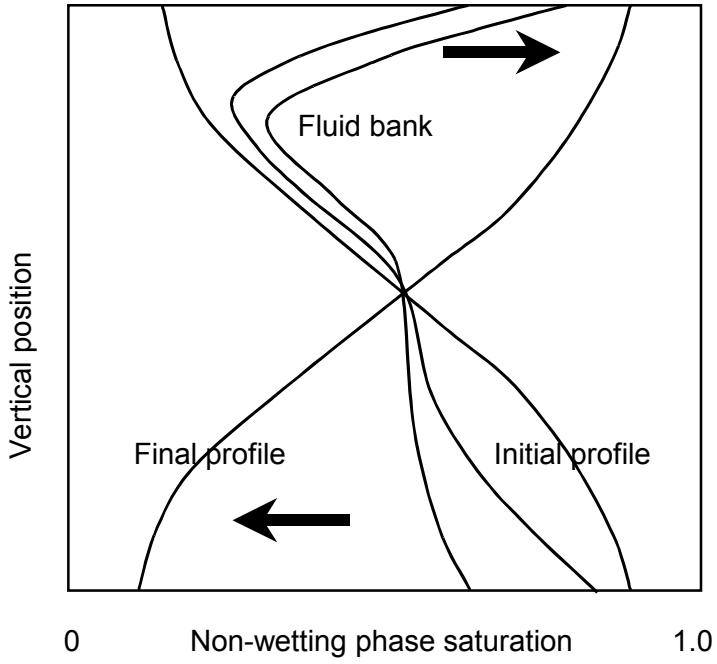

Figure 1.3: The schematic of the formation of a fluid bank in a counter-current flow process.

CHAPTER 2

OBJECTIVES AND APPROACH

Objectives

The main objectives of this work are:

1. To provide a mechanistic approach for modeling counter-current flow in porous media with and without fluid banks.
2. To gain physical understanding of counter-current flow in porous media including the formation of fluid banks.
3. To provide a methodology for extracting capillary pressures and relative permeabilities from counter-current fluid flow experiments.

Approach

The approach for obtaining the objectives consists of conceptual and numerical inverse modeling of counter-current fluid flow experimental observations. The main variables of interest are capillary pressure and relative permeabilities. The inverse modeling procedure consists of forward simulation and multi-variable parameter optimization.

CHAPTER 3

METHODOLOGY

In this research, the saturation maps of porous media samples obtained by an X-ray Computed Tomography (CT) scanner constitute the experimental data. Numerical reservoir simulation coupled with automatic-history matching was used to obtain relative permeabilities and capillary pressures. Several optimization methods have been tested for this purpose. Because of the complexity of counter-current flow, saturation history dependent modeling was implemented based on capillary hysteresis.

3.1 Computed Tomography (CT)

X-ray CT is a non-destructive imaging technique that provides three-dimensional distribution of properties such as density and nuclear atomic number. In 1972, Housfield designed the first medical X-ray CT scanner based on Radon's tomography theory, which can be used to derive the analytical equations relating projections to parameters of the investigated object. This technique was introduced into petroleum industry in the late 70s, with the primary purpose of rock characterization.

The application of X-ray CT in investigating enhanced oil recovery processes was introduced by Wang and Avral (1984). After that, many other researchers (Cromwell et al. 1984, Hove et al. 1985, Wellington and Vinegar 1985&1987, Withjack and Akervoll 1988, Chatzis et al. 1989, Hove et al. 1990, Lenormand et al. 1990, Liu et al. 1990, Ganapathy 1993, Hicks et al. 1994, Yamamoto et al 1997) investigated its feasibility and applications in water flooding, CO_2 displacement, water alternating gas (WAG) process

and other enhanced oil recovery processes. Effects of heterogeneity of the core, fingering, dispersion of flood fronts and end-effects were observed and studied with its help.

An X-ray CT scanner mainly consists of four parts: X-ray source, detector, sample translation system, and data processor. The X-rays are attenuated as they penetrate the sample. The degree of the X-ray attenuation is captured by the detector. From projections at different angles, the data processor can generate a cross-sectional image of the sample by using a backward algorithm based on Radon transformation. A series of cross-sectional images can be obtained by changing the position of the sample thus generating three-dimensional data sets describing the sample such as porosity and fluid saturation. Wellington and Vinegar (1987) and Hunt et al. (1988) presented a detailed description about different generations of scanners.

Jasti et al. (1993) presented a non-traditional X-ray CT scanner (microfocal X-ray CT scanner) where a cone-shaped, diverging X-ray beam was used to generate 2D transmission images. Unlike traditional X-ray CT scanner, a 3D reconstruction is created directly instead of creating a series of 2D slices. This allows direct measurement of 3D geometric and topological properties of porous media on a microscale. The source-to-object distance is adjusted to achieve the necessary balance between spatial resolution and maximum object size.

Attenuation intensity is the unique property measured by an X-ray CT scanner. From Beer's Law, the attenuation intensity before and after going through the sample is:

$$I = I_0 \exp\left(-\int \mu(x, y) dL\right) \tag{3.1}$$

where I_0 is the incident X-ray intensity and I is the intensity remaining after it passes the sample. $\mu(x,y)$ is 2D distribution of attenuation coefficients. The projection value of CT scanning can also be expressed as:

$$\ln(I/I_0) = -\int \mu(x,y)dL \tag{3.2}$$

According to the Radon transformation, CT images can be reconstructed after getting projection values at different angles.

For one pixel,

$$I = I_0 e^{-\mu(x,y)L} \tag{3.3}$$

where μ is the linear attenuation coefficient. This coefficient is a function of bulk density and atomic number:

$$\mu = a\rho_b + b\rho_b Z^{3.8}/E^{3.2} = \mu_{compton} + \mu_{photoeclectric} \tag{3.4}$$

where a is an energy independent constant and b is a constant. The first term of the above equation mainly represents the Compton scattering effect and the second term accounts for the photoelectric effect. These two effects occur at different energy level, the former at above 100kv and the latter below 100kv. Based on this phenomenon, the dual-energy X-ray CT was developed for co-determination of density and nuclear atomic number. Kantzas (1990) presented a detailed discussion on the physical principles of X-ray CT and its applications.

The porosity can be derived from the linear attenuation coefficient of a rock saturated with fluid using a bulk volume model.

$$\mu_b = \mu_m(1-\phi) + \mu_f\phi \tag{3.5}$$

where μ_m is the linear attenuation coefficient of the rock matrix and μ_f is the linear attenuation coefficient of the fluid. Then,

$$\phi = \frac{\mu_b - \mu_m}{\mu_f - \mu_m} \tag{3.6}$$

The above method is called single-scanning method, but it requires an estimate of μ_f and μ_m. The implementation is completed by saturating the sample with a single fluid and taking one scan. Another method to obtain porosity is a double-scanning method, in which the CT scanner scans the core sample twice and each time the sample is saturated with different fluids.

$$\mu_{b1} = \mu_m(1-\phi) + \mu_{f1}\phi \tag{3.7}$$

$$\mu_{b2} = \mu_m(1-\phi) + \mu_{f2}\phi \tag{3.8}$$

Solving for ϕ gives:

$$\phi = \frac{\mu_{b1} - \mu_{b2}}{\mu_{f1} - \mu_{f2}} \tag{3.9}$$

The porosity of each pixel can be calculated by:

$$\phi_{pixel} = \phi_{avg} \times \frac{CT_{wet} - CT_{vacuum}}{(CT_{wet} - CT_{vacuum})_{avg}} \tag{3.10}$$

where ϕ_{avg} is the average porosity of the core; CT_{wet} is the CT number when the core is saturated with a fluid and CT_{vacuum} is the CT number after the core is place under vacuum. The porosity distribution can be obtained thereafter.

When the rock is fully saturated with two phases, the bulk attenuation coefficient can be calculated with Equations (3.7) and (3.8), respectively. Suppose these two phases

coexist in the pore space with saturation S_1 and S_2 for each phase, the attenuation coefficient is:

$$\mu_b = \mu_{b1} S_1 + \mu_{b2} S_2 \tag{3.11}$$

Substituting Equations (3.7) and (3.8) into Equation (3.10) yields:

$$\mu_b = \mu_m (1-\phi) + \mu_{f1} \phi S_1 + \mu_{f2} \phi S_2 \tag{3.12}$$

Based on the above equations, there are a couple of methods to calculate fluid saturation. If the attenuation coefficients are known, the saturation is easy to calculate by combining equation (3.11) with $S_1 + S_2 = 1.0$.

$$S_1 = \frac{\mu_b - \mu_{b1}}{\mu_{b2} - \mu_{b1}} \tag{3.13}$$

Another method is subtracting the CT number of 100% saturated core sample (Equation 3.7) from that of the partially saturated core sample (Equation 3.11) and then combining with $S_1 + S_2 = 1.0$. The result is:

$$S_1 = \frac{\mu_b - \mu_{b1}}{\phi(\mu_{f2} - \mu_{f1})} \tag{3.14}$$

If the attenuation coefficients of the matrix and two fluids are known, the saturation can be calculated from Equation (3.11):

$$S_1 = \frac{(\mu_b - \mu_m) - \phi(\mu_b - \mu_{f2})}{\phi(\mu_{f1} - \mu_{f2})} \tag{3.15}$$

The saturation distribution can be obtained by:

$$(S_1)_{pixel} = \frac{CT_{wet} - CT_{f1}}{(CT_{wet} - CT_{f1})_{avg}} \times \frac{\phi_{avg}}{\phi} \times (S_1)_{avg} \tag{3.16}$$

where CT_{f1} is the CT number when the core is saturated with fluid 1.

3.2 History Matching

History matching is a procedure in which reservoir parameters such as permeability, porosity, relative permeabilities and capillary pressure are modified in a forward model (reservoir simulator) to obtain a reservoir representation that matches the observed reservoir performance.

The first report on history matching was from Kruger (1961). From then on, this technique has been extensively used in reservoir characterization and description. Archer et al. (1973) introduced this technique to determine relative permeabilities from coreflood experiments. Chavent et al. (1980) extracted relative permeabilities as well as capillary pressures with automatic history matching. With the development of computers, the application of automatic history matching in coreflood analysis has been studied by many researchers (Kerig et al. 1987, Watson et al. 1986, Richmond et al. 1988, Jennings et al. 1988, Yang and Watson 1991, Nordtvedt et al. 1993, Akin and Demiral 1997, Akin and Kovscek 1999).

In this study, the observed data are temporal and spatial saturations determined with a CT scanner and the model parameters are relative permeabilities and capillary pressure. The absolute permeability was measured from the pressure drop and flow rate by using Darcy equation and the porosity distribution was obtained from the CT scanner. The forward model is a commercial reservoir simulator Eclipse® 100, which is a black oil simulator. Appendix A gives a typical data file for this simulator.

Figure 3.1 is a schematic representation of history matching method. The forward model used in this method is a commercial reservoir simulator (Eclipse®). The initial conditions, the fluids properties such as capillary pressure, relative permeabilities,

absolute permeability and porosity are input in the numerical simulator and the saturation profiles are extracted. These profiles are compared with the experimental data. If the profiles match satisfactorily, the parameters used in the forward model are the ones that can accurately describe the system. If not, relative permeabilities and capillary pressures are modified with an optimization method (Levenburg-Marquardt method) and put back into the forward model. The parameters are repeatedly optimized until the simulated saturation profiles match the experimental ones.

In the implementation of this method, C-shell programming is applied to extract saturation data from the simulator output files. Then the generated saturation data files are put into an optimizer programmed with C language to generate a new set of parameters. These new parameters are written into files in a format that the simulator can read. The C-shell codes, as well as the C language optimizer codes, are given in appendix B

Mathematically, the comparison between experimental data and model data is described with an objective function, expressed in the following form:

$$J = \sum_{\Omega(x,y,z,t)} \left(S^{cal}_{x,y,z,t}(k_r, p_c) - S^{\exp}_{x,y,z,t} \right)^2 \tag{3.17}$$

where $S_{x,y,z,t}$ is the saturation distribution in the core sample, which is a function of relative permeability k_r and capillary pressure p_c. Relative permeabilities and capillary pressure are automatically adjusted to minimize the objective function J until the process converges.

Model parameters (relative permeabilities and capillary pressure) are functions of saturation. There are different representations for relative permeability curves and the most commonly used is the power law form as in Equation (3.18).

$$k_{ri}=a_i(S_i-S_{ir})^{bi} \tag{3.18}$$

where S_i is the saturation of phase i and S_{ir} is the residual saturation of phase i, a_i and b_i are parameters to be determined.

Al-Wadahi et al. (2000) expressed the capillary pressure as follows

$$p_c=a_{pc}(p^*_c+b_{pc}) \tag{3.19}$$

where p^*_c is a function of final fluid saturation distribution obtained from experiments. a_{pc} and b_{pc} are parameters to be determined.

According to Darcy equation, the velocity of phase i is:

$$v_i = \frac{k_i}{\mu_i}\left(\nabla p_i - \rho_i g z\right) \tag{3.20}$$

The pressure in Equation (3.20) is in a differential form, so parameter b_{pc} in Equation (3.19) does not affect the results from the forward model. Equation (3.19) can be simplified:

$$p_c=a_{pc}p^*_c \tag{3.21}$$

The relative permeability and capillary pressure curves can also be represented as spline function or piecewise function. If the capillary pressure curve cannot be constructed with magnitude scaling of the final saturation profile, it needs to be represented as a spline function or piecewise function. Interested readers on the spline function representation are referenced to Kerig et al. (1987).

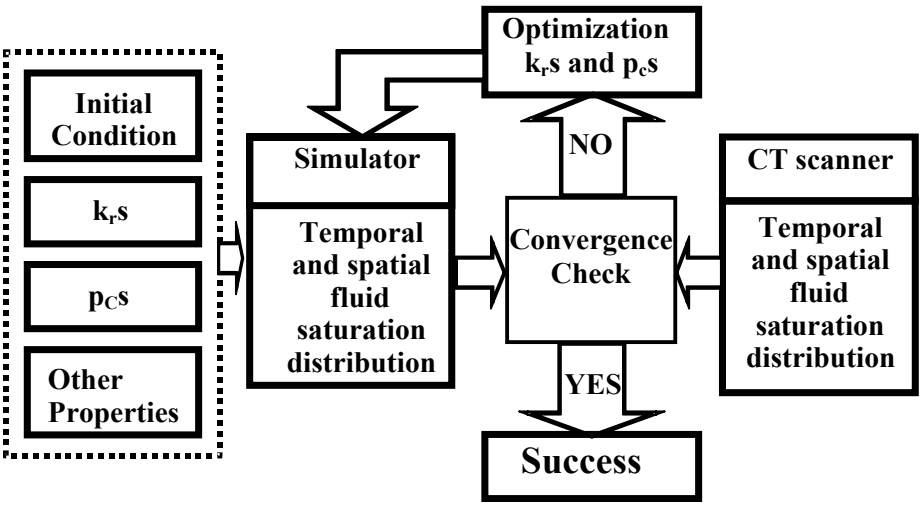

Figure 3.1: Schematic of the history matching method.

3.3 Optimization Methods

There are three categories of optimization algorithms (Wu, 2000): gradient based methods, sensitivity coefficient-based methods, and global optimization methods.

3.3.1 Gradient Methods

3.3.1.1 Steepest Descent Method

Consider the first-order Taylor series expansion of the objective function $J(\mathbf{X})$ at $\mathbf{X}_k$:

$$J(\mathbf{X}_{k+1}) = J(\mathbf{X}_k + \Delta\mathbf{X}_k) \approx J(\mathbf{X}_k) + \boldsymbol{D}_k^T \Delta\mathbf{X}_k \tag{3.22}$$

where $\boldsymbol{D}_k$ is the gradient of the objective function evaluated at $\mathbf{X}_k$:

$$\boldsymbol{D}_k \equiv \nabla J(\mathbf{X})|_{\mathbf{X}=\mathbf{X}_k} \tag{3.23}$$

For $J(\mathbf{X}_{k+1})$ to be less than $J(\mathbf{X}_k)$, the second term of the right-hand side of the Equation (3.22) must be negative:

$$\boldsymbol{D}_k^T \Delta\mathbf{X}_k < 0 \tag{3.24}$$

To get the fastest convergence, this has to be most negative, i.e. its absolute value has the largest value. This condition is satisfied when:

$$\Delta\mathbf{X}_k = -\boldsymbol{D}_k \tag{3.25}$$

Therefore:

$$\mathbf{X}_{k+1} = \mathbf{X}_k - \boldsymbol{D}_k \tag{3.26}$$

To avoid oscillations, a step size constant α is normally used to limit the searching process. The range for α in this research is 0.1~0.5. The parameter updating equation is modified as follows:

$$\mathbf{X}_{k+1} = \mathbf{X}_k - \alpha\boldsymbol{D}_k \tag{3.27}$$

The Steepest Descent method works well when the gradient is large, or far away from the minimum. However, it progresses very slowly in the vicinity of the minimum. The rate of convergence for this method is linear at best (Yang and Watson 1987).

3.3.1.2 Conjugate Gradient Method

The Steepest Descent method is a linear search algorithm. The search directions are orthogonal. For quadratic functions with elliptical contours, this produces a zigzag trajectory of short steps with slow convergence. The Conjugate Gradient method uses conjugate directions instead of negative gradient directions to speed up the convergence rate. For quadratic functions, this method guarantees quadratic termination, which means that it minimizes a quadratic function exactly in a finite number of iterations. The Conjugate Gradient method starts with Steepest Descent method:

$$\mathbf{X}_1 = \mathbf{X}_0 - \alpha \boldsymbol{D}_0 \tag{3.28}$$

Then, in the next steps, it uses the conjugate directions

$$\mathbf{X}_{k+1} = \mathbf{X}_k - \alpha \boldsymbol{P}_k \tag{3.29}$$

where $\boldsymbol{P}_k$ is the conjugate search direction defined by:

$$\boldsymbol{P}_k = -\boldsymbol{D}_k + -\beta_k \boldsymbol{P}_{k-1} \tag{3.30}$$

where

$\beta_k = (\Delta \boldsymbol{D}_{k-1}{}^T \boldsymbol{D}_k) / (\Delta \boldsymbol{D}_{k-1}{}^T \boldsymbol{P}_{k-1})$ due to Hestenes and Steifel, and

$\beta_k = (\boldsymbol{D}_k{}^T \boldsymbol{D}_k) / (\boldsymbol{D}_{k-1}{}^T \boldsymbol{P}_{k-1})$ due to Fletcher and Reeves, and

$\beta_k=(\Delta \boldsymbol{D}_{k-1}{}^T \boldsymbol{D}_k)/(\boldsymbol{D}_{k-1}{}^T \boldsymbol{P}_{k-1})$ due to Polak and Ribiere, and

$\Delta \boldsymbol{D}_{k-1}= \boldsymbol{D}_k - \boldsymbol{D}_{k-1}$

3.3.1.3 Variable Metric Method (Quasi-Newton method)

The search direction of Steepest Descent method and Conjugate Gradient method is based on the first-order approximation to the objective function, so the convergence rate is slow. In order to get a better convergence rate, the second-order approximation is made in Newton's method.

$$J(\mathbf{X}_{k+1})= J(\mathbf{X}_k+\Delta\mathbf{X}_k) \approx J(\mathbf{X}_k)+\boldsymbol{D}_k{}^T \Delta\mathbf{X}_k +1/2\ \Delta\mathbf{X}_k{}^T \boldsymbol{H}_k \Delta\mathbf{X}_k \tag{3.31}$$

where $\boldsymbol{H}_k$ is the Hessian matrix (or second derivative) of the objective function. The search direction is as follows:

$$\mathbf{X}_{k+1}= \mathbf{X}_k - \boldsymbol{H}_k^{-1}\boldsymbol{D}_k \tag{3.32}$$

The rate of the convergence for this method is quadratic, currently the highest sought in practice.

The problem with Newton's method is that the computation of Hessian matrix is very expensive for history matching. The Variable Metric method was introduced in order to avoid direct computing of Hessian matrix. In this method, only the first-order derivative is needed and the Hessian matrix is approximated from previous steps. This method is a multivariable secant method. Therefore, in the Variable Metric method, the search direction is given by:

$$\mathbf{X}_{k+1}= \mathbf{X}_k - \boldsymbol{B}_k\boldsymbol{D}_k \tag{3.33}$$

where $\boldsymbol{B}_k$ is the approximation of the inverse of the Hessian matrix $\boldsymbol{H}_k^{-1}$. While the Hessian matrix is computed at each iteration in Newton's method, Variable Metric method updates $\boldsymbol{B}_k$ at each iteration:

$$\boldsymbol{B}_{k+1} = \boldsymbol{B}_k + \boldsymbol{U}_k \tag{3.34}$$

There are several methods to calculate the updating matrix $\boldsymbol{U}_k$. The most commonly used method is Broyden-Fletcher-Goldfarb-Shanno (BFGS) method (Gill et al. 1981).

$$U_k = \frac{(X_{k+1} - X_k)(X_{k+1} - X_k)^T}{(X_{k+1} - X_k)^T (D_{k+1} - D_k)} - \frac{[B_k(D_{k+1} - D_k)][B_k(D_{k+1} - D_k)]^T}{(D_{k+1} - D_k)^T B_k (D_{k+1} - D_k)}$$

$$+ (D_{k+1} - D_k)^T B_k (D_{k+1} - D_k) V V^T \tag{3.35}$$

$$\text{where } V = \frac{(X_{k+1} - X_k)}{(X_{k+1} - X_k)^T (D_{k+1} - D_k)} - \frac{B_k (D_{k+1} - D_k)}{(D_{k+1} - D_k)^T B_k (D_{k+1} - D_k)} \tag{3.36}$$

3.3.2 Sensitivity Coefficient-Based Methods

3.3.2.1 Gauss-Newton Method

The first order derivative of the objective function J (note: the objective function used in the sensitivity coefficient-based methods is defined as half of that in Equation 3.17 to avoid the appearance of a factor of two in the derivatives) is:

$$\nabla J(\mathbf{X}) = \boldsymbol{G}^T [\boldsymbol{S}^{cal}(\mathbf{X}) - \boldsymbol{S}^{exp}] \tag{3.37}$$

where $\boldsymbol{G}$ is sensitivity coefficient matrix defined as the derivative of the matching data $\boldsymbol{S}^{cal}$ with respect to model parameters **X.**

Then the Hessian matrix is:

$$\nabla(\nabla J(\mathbf{X})) = \boldsymbol{G}^T \boldsymbol{G} - \nabla(\boldsymbol{G}^T) [\boldsymbol{S}^{\text{cal}}(\mathbf{X}) - \boldsymbol{S}^{\text{exp}}] \tag{3.38}$$

The second term of the right-hand side of the above equation is small enough to be neglected, so the Hessian matrix can be approximated with:

$$\boldsymbol{H}(\mathbf{X}) \approx \boldsymbol{G}^T \boldsymbol{G} \tag{3.39}$$

The Gauss-Newton algorithm solves

$$\boldsymbol{H}(\mathbf{X}_k)\, \Delta\mathbf{X}_k = -\nabla J(\mathbf{X}_k) \tag{3.40}$$

Model parameters are updated with:

$$\mathbf{X}_{k+1} = \mathbf{X}_k + \Delta\mathbf{X}_k \tag{3.41a}$$

The Gauss-Newton method can produce an increase in the sum of squares when the requested increment extends beyond the region where the approximation of Hessian matrix is valid. Even in these circumstances, however, this approximation will be a close approximation to the actual Hessian matrix for a sufficiently small region around $\mathbf{X}_k$. Thus a small step in the direction $\Delta\mathbf{X}_k$ should produce a decrease in the sum of squares. Therefore a step factor α is introduced into Equation (3.41a) yields

$$\mathbf{X}_{k+1} = \mathbf{X}_k + \alpha\, \Delta\mathbf{X}_k \tag{3.41b}$$

where α is the step size.

The attractiveness of the Gauss-Newton method is that second order convergence may be achieved using only first order derivatives.

3.3.2.2 Levenberg-Marquardt Method

Levenberg-Marquardt method is a modified Gauss-Newton algorithm. Equation (3.40) is modified to the following form:

$$(\boldsymbol{H}(\mathbf{X}_k)+\lambda \boldsymbol{I})\Delta\mathbf{X}_k = -\nabla J(\mathbf{X}_k) \quad (3.42)$$

Model parameters are updated in the same way as in the Gauss-Newton method. The Levenberg-Marquardt method is a compromise of the Gauss-Newton method and the Steepest Descent method. When $\lambda=0$, it is the Gauss-Newton method and when $\lambda \to \infty$ it is the Steepest Descent method. When Hessian is singular, the Levenberg-Marquardt method makes sure that there is a solution to the problem.

3.3.3 Global Optimization Methods

3.3.3.1 Simulated Annealing Method

Simulated Annealing method is based on the analogy between the simulation of the annealing of solids and solving large combinatorial optimization problems. Simulated Annealing method can be viewed as a sequence of metropolis algorithms evaluated at a sequence of decreasing values of the control parameter. Initially, the control parameter is given a high value and then a sequence of configuration of the combinatorial optimization problem is generated as follows. As in the iterative improvement algorithm, a generation mechanism is defined, so that, given a configuration i, another configuration j can be obtained by choosing at random an element from the neighborhood of i (van Laarhoven and Aarts 1987, and Akin and Demiral 1997).

3.3.3.2 Genetic Algorithm

Genetic Algorithms (GAs) were invented by John Holland (Romero et al. 2000). GAs are randomized search techniques based on the mechanics of natural

selection according to Darwinian evolutionary theory and the "survival of the fittest" principle. They also draw ideas from genetics to describe solutions to the problem under consideration as individuals. To mimic a natural evolution process, GAs start with an initial population of feasible solutions to the problem. Individual solutions are then selected from the population according a stochastic process that favors the individuals with better performance, and their genetic information is recombined and modified following probabilistic transition rules such as the genetic operators, to form a new population. The process is repeated until a convergence is detected, or a specified maximum number of function evaluations or generations is reached (Romero et al. 2000).

3.3.3.3 Tunneling method

The basic idea of this method is to tunnel from one valley of the objective function to another, to be able to find a sequence of local minima with decreasing function values and then ignore all the local minima with larger objective function values than the ones already found. This "ignoring" minima makes the algorithm faster and more efficient than other global optimization algorithms like Genetic Algorithm and Simulated Annealing. The commonly used optimization methods can be used for finding the local minima (Gomez et al. 1999).

3.4 Capillary Hysteresis

Hysteresis phenomena occur in many fields of the nature. Some examples include magnetic hysteresis, electric polarization hysteresis, and capillary hysteresis. A general description of hysteresis is given in **Figure 3.2**. Suppose there are two physical properties x – independent variable and y – dependent variable. When x increases from point 1 to point 2 ($x_1<x_2$), the dependent variable y follows path 1 ($y_1 \rightarrow y_2$), and when x decreases from point 2 to point 1, the dependent variable y follows path 2 ($y_2 \rightarrow y_1$). If path 1 is different from path 2, it is said the relationship between x and y is hysteretic. Sometimes, if infinitesimally small increments are used and enough experimental time is allowed, the hysteresis can be eliminated. This hysteresis is time-dependent hysteresis. If the hysteresis exists no matter how small the increment is and how long the experimental time is, it is called permanent hysteresis. Capillary hysteresis is permanent.

A complete description of capillary pressure for a porous medium consists of bounding capillary pressure curves and intermediate scanning curves, which include primary scanning curves and subsidiary scanning curves. **Figure 3.3** shows a family of capillary pressure curves for a porous medium. $\mathbf{D_0}$ is the primary drainage capillary pressure curve. $\mathbf{D_1}$ and $\mathbf{I_1}$ are the secondary drainage and imbibition capillary pressure curves, respectively. These two curves form a closed loop, called the capillary hysteresis loop. The curves inside the hysteresis loop are scanning curves. These scanning curves are the capillary pressure paths that occur when there is a reversal of direction during a drainage or an imbibition process. For example, during the secondary drainage process, it follows drainage capillary curve $\mathbf{D_1}$. The process stops at point **G** and an imbibition process is initiated. This imbibition process cannot follow the imbibition capillary

pressure curve $\mathbf{I_1}$, simply because of the discontinuity between the starting point (on drainage capillary pressure curve $\mathbf{D_1}$) and the imibibition capillary pressure curve $\mathbf{I_1}$. The process will follow an imbibition-scanning curve **GH** to asymptotically approach curve $\mathbf{I_1}$. A similar process occurs when there is a direction reversal at point **D** during an imbibition process and it follows a drainage-scanning curve starting at point **D**. If there is another direction reversal after the first one, the process is going to follow the subsidiary drainage or imbibition scanning curves, such as **EC**, **HJ** and **JK**.

To study this complex capillary hysteresis, Poulovassilis (1962) applied the independent domain theory developed by Everett and coworkers (1952, 1954a, 1954b, 1955) for sorption hysteresis. From Poulavassilis' method, the drainage-scanning curves can be constructed if the imibibition-scanning curves are known from experiments and vice versa. Philip (1964) reexamined the independent domain theory with similarity hypothesis. In his method, the scanning curves can be constructed with only the hysteresis loop (the secondary drainage and imibibition capillary pressure curves). With a predetermined normalized density distribution function, the hysteresis loop can be completed from only one branch (drainage or imbibition) and hence the family of scanning curves can be approximated. Everett's independent domain theorems are summarized according to experimentally observed capillary pressure behavior following Morrow (1970) and Rojas et al. (2001):

1. The secondary drainage curve, $\mathbf{D_1}$, and the imbibition curve, $\mathbf{I_1}$, form a closed loop, with all the subsequent capillary pressure data points lying on or within this loop.

2. The primary drainage scanning curves, which begin at the imibibition curve, I_1, either meet at the upper intersection of the loop, or asymptotically approach the

secondary drainage curve, $\mathbf{D_1}$, in a region close to the intersection. The primary imbibition scanning curves start from the drainage curve, I_1, and follow the similar behavior.

3. Any point within the hysteresis loop can be reached by many paths. Complete specification of the system at a given pressure-saturation coordinate must include the path by which the point was attained, since the path determines the microscopic distribution of the fluid and future behavior of the system. **Figure 3.3** shows two paths (two imbibition scanning curves) that can reach point **O**.

4. If the system were taken through a series of pressure oscillation, after the *n*th pressure reversal, the system moves toward the point at which the (*n*-1)th reversal occurred, and if the system carried through this point, it moves toward the (*n*-3)th reversal point, and so on. For example, **JK** is the *n*th reversal, and it moves towards point **H**, where the (*n*-1)th reversal occurred. After it passes this point, it will approach the (*n*-3)th reversal point **D**.

The base assumption of the independent domain theory is that a porous medium can be viewed as an assembly of independent pore domains, similar to the concept of a representative volume. Each pore domain has its own hysteretic phenomenon and this hysteretic behavior of each pore domain is independent to other pore domains. The hysteresis of the system is an overall effect of these pore domains. However, pore domains are not independent from each other, and the change of each pore domain may affect its neighbors. The independent domain model was expanded by Enderby (1956) with cooperative pore domains. With the dual site-bond model (DSBM) (Rojas et al.

2001) examined the validity of Everett's theorems. Most of them are valid even when the dependence of pore domains is considered.

Figure 3.4 shows the general behavior of capillary hysteresis with the loop of drainage and imbibition capillary curves and the scanning curves for both drainage and imbibition processes (Morrow and Harris 1965). **Figure 3.4a** shows the imbibition scanning curves. These curves depart abruptly from the drainage capillary pressure curve at the end of a drainage process, and then descend toward the imbibition curve approaching it asymptotically. **Figure 3.4b** shows the drainage scanning curves. These curves start at some specific points on the imbibition capillary pressure curve and asymptotically approach the drainage capillary pressure curve. The behaviors of drainage and imbibition capillary curves and the corresponding scanning curves are consistent with Everett's independent domain theory, which requires the scanning curves converge tangentially onto the bounding curves. The shape of the scanning curves and their behavior at the point of change between types of displacement impact the formation of the fluid banks.

From Poulavassilis' study (1962), the drainage-scanning curves can be constructed if the primary imbibition-scanning curves are known from experiments and vice versa. Philip (1964) reexamined the independent domain theory with a similarity hypothesis. In his method, the scanning curves can be constructed with only the hysteresis loop (the secondary drainage and imbibition capillary pressure curves). With a predetermined normalized density distribution function, the hysteresis loop can be completed from only one branch (drainage or imbibition) and hence the family of capillary scanning curves can be approximated.

Although the above methods for constructing scanning curves are based on fundamental physical models, they are not convenient to apply to reservoir modeling. Killough (1976) and Kleppe et al. (1997) have proposed some mathematical representation methods for capillary pressure scanning curves, and these representations can be readily incorporated into reservoir modeling. In the following, Killough and Kleppe methods are briefly stated.

The method presented by Killough (1976) predicts capillary scanning curves by using weighted average of the complete drainage and imbibition loop. For an oil-gas system, his formula for an imbibition-scanning curve initiated from the drainage curve may be written as:

$$p_c = p_c^d + F\left(p_c^i - p_c^d\right) \tag{3.43}$$

where the weighting factor F is defined as:

$$F = \frac{\dfrac{1}{S_{g1} - S_g + \varepsilon} - \dfrac{1}{\varepsilon}}{\dfrac{1}{S_{g1} - S_{gr} + \varepsilon} - \dfrac{1}{\varepsilon}} \tag{3.44}$$

The function F depends only on the point where p_c left the bounding curve and on a predetermined interpolative parameter for the curvature ε. The normal range for ε is 0.05-0.1 according to Killough (1976). S_{g1} is where the hysteresis occurred and S_{gr} is the maximum residual gas saturation. A similar expression is used for drainage-scanning curves.

The Kleppe method (1997) is based on the strong similarity between the scanning curves and the corresponding drainage and imbibition capillary pressure curves of the

hysteresis loop. An imbibition-scanning curve initiated on the drainage capillary pressure curve at S_g=S_{g1} and ending at S_g=S_{g2} may be defined as:

$$p_c\left(S_g\right) = p_c^i\left(S_g^i\right) \tag{3.45}$$

where

$$S_g^i = S_{gr} + \left[\frac{S_g^i\left(p_c^i = p_{c1}\right) - S_{gr}}{S_{g1} - S_{g2}}\right]\left(S_g - S_{g2}\right) \tag{3.46}$$

applicable in the saturation range: $S_{g1} \geq S_g \geq S_{g2}$. A similar process can be applied to drainage-scanning curves initiated on the imbibition capillary pressure curve.

Figure 3.5 shows the comparison of the scanning curves constructed by these two methods and the match with the experiment from Morrow and Harris (1965). There is a good match between constructed imbibition-scanning curves from both methods and the experimental data shown in **Figure 3.5a**. In **Figure 3.5b**, the drainage-scanning curves from the Killough method have a better match than that from the Kleppe method. The interpolative parameter ε in Killough method is 0.1.

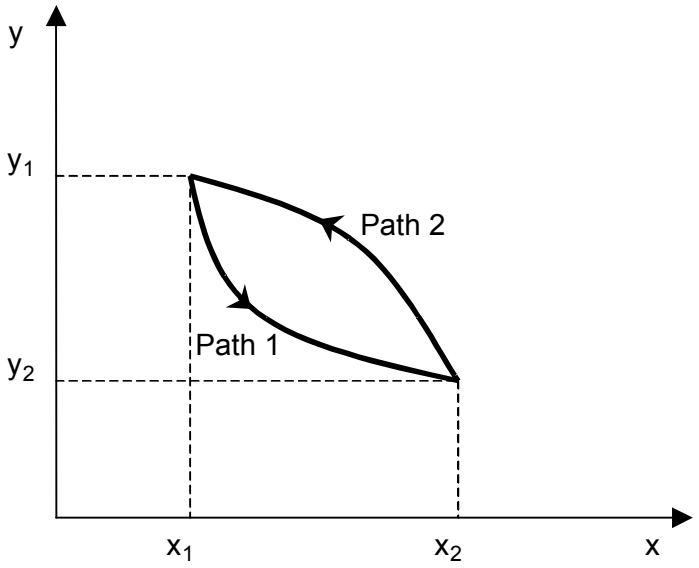

Figure 3.2: General behavior of hysteresis.

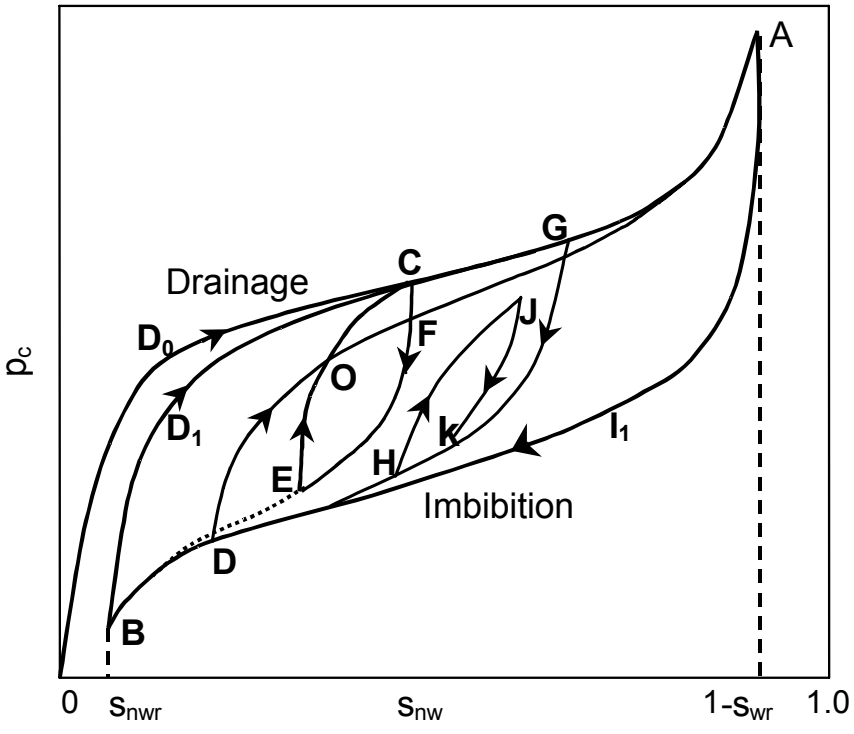

Figure 3.3: Capillary hysteresis loop and scanning curves.

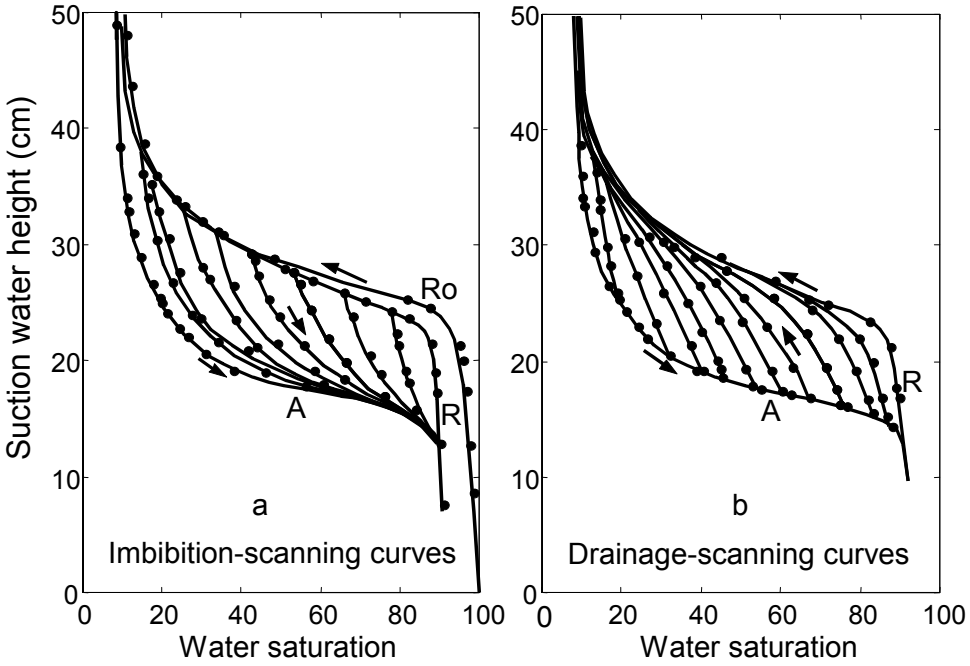

Figure 3.4: Capillary pressure hysteresis loop (from Morrow and Harris 1965).

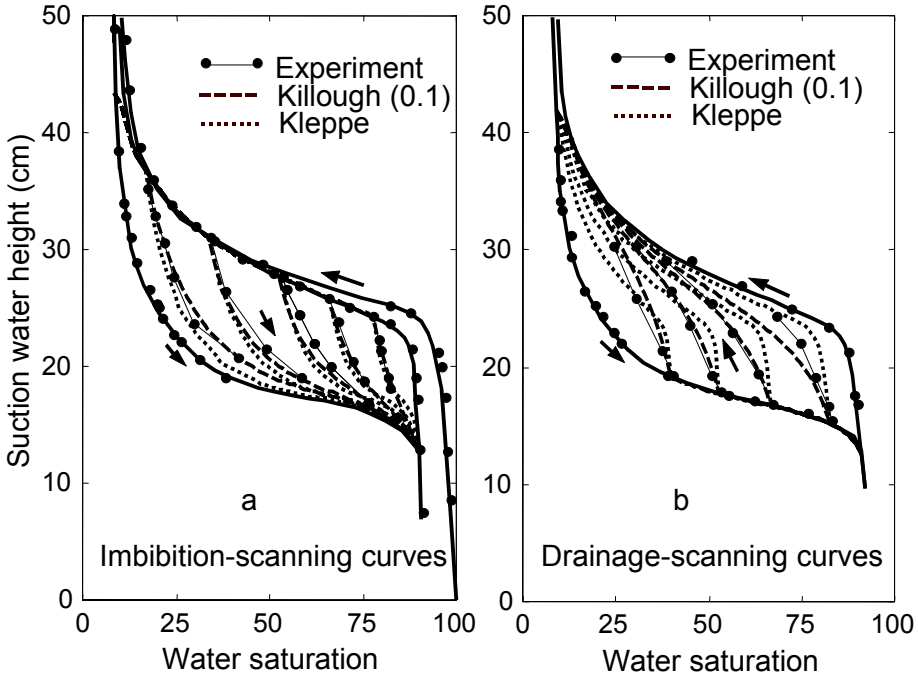

Figure 3.5: Comparison of constructed capillary scanning curves from Kleppe and Killough methods.

3.5 History Dependent Modeling

Early attempts (Briggs 1963, Briggs and Katz 1966, Al-Wadahi et al. 2000) to simulate counter-current flow experiments were using one capillary pressure curve and one pair of relative permeability curves. Simulation attempts using either drainage or imbibition capillary pressure curve failed to reproduce the characteristics of counter-current experiments. Al-Wadahi et al. (2000) successfully simulated Barbu et al.'s (1999) experiments with a capillary pressure curve constructed based on the final saturation profile, which is an S-shaped curve. The same approach has been tried to simulate Karpyn's (2001) experiments. The simulation can generate the general characteristic of the experiments, but it cannot capture the fluid banks formed at the top of the core sample. A more general approach is required to model the counter-current flow process.

According to Everett's independent domain theory, any point within a hysteresis loop can be reached by many paths. The path by which the point was attained has to be specified to get a complete description of the status of the system (Morrow 1970). **Figure 3.3** shows some paths by which point **O** can be reached. The future behavior of the system starting at point **O** would be not be unique, even for cases that undergo the same type of process. For example, if a drainage process is initiated from point **O**, capillary pressure can follow path **OCA**, or **OFA** to approach the drainage capillary pressure curve, depending on the saturation history. These different paths will result in different fluid flow behavior. Therefore, to properly model oil recovery processes, capillary pressure hysteresis has to be taken into account.

In the following part, a counter-current flow scenario is stated to explain how history dependent modeling works. The heavy fluid is the wetting phase in this scenario,

which is consistent with the actual experiments. The core is first drained by the non-wetting phase until an evenly distributed saturation in the core (two phase injection). In the family of the capillary pressure curves, it is located on the drainage capillary pressure curve - point **O** in **Figure 3.6** corresponding to the saturation. In the first stage, the system is closed and fluids segregate because of the density difference. Because the heavy phase is the wetting phase, the upper part of the core undergoes drainage process. Among the capillary pressure curves, it follows the drainage capillary pressure curve with increasing non-wetting phase saturation. However, in the lower part, wetting phase saturation increases, which is an imbibition process. Among the capillary pressure curves, it follows an imbibition-scanning curve initiated from point **O**. At the end of this stage, the fluids are segregated in the system with a high saturation of heavy fluid at the bottom and light fluid at the top. The final saturation profile is shown in **Figure 3.6** (stage 1). In the second stage, the core is rotated by 180º after segregation. Now the upper part is undergoing drainage process. Because this part was located on the imbibition-scanning curve **AO** before rotation, it will follow drainage-scanning curves starting from this imbibition-scanning curve. In the meantime, the lower part follows the imbibition-scanning curves starting from the drainage capillary pressure curve **OB**. **Figure 3.6** also shows the process of the second stage on the right half of the graph. Points **D'** and **E'** in the upper part of the profile follow the drainage-scanning curves initiating from **D** and **E** in the capillary pressure loop. Points **C'** and **F'** in the lower part of the profile follow the imbibition-scanning curves initiating from **C** and **F**. The ending points of the saturation profile **A'** and **B'** follow the bounding drainage and imbibition capillary curves respectively.

In counter-current flow, drainage and imbibition flow regimes are present and two pairs of relative permeability curves are used in modeling.

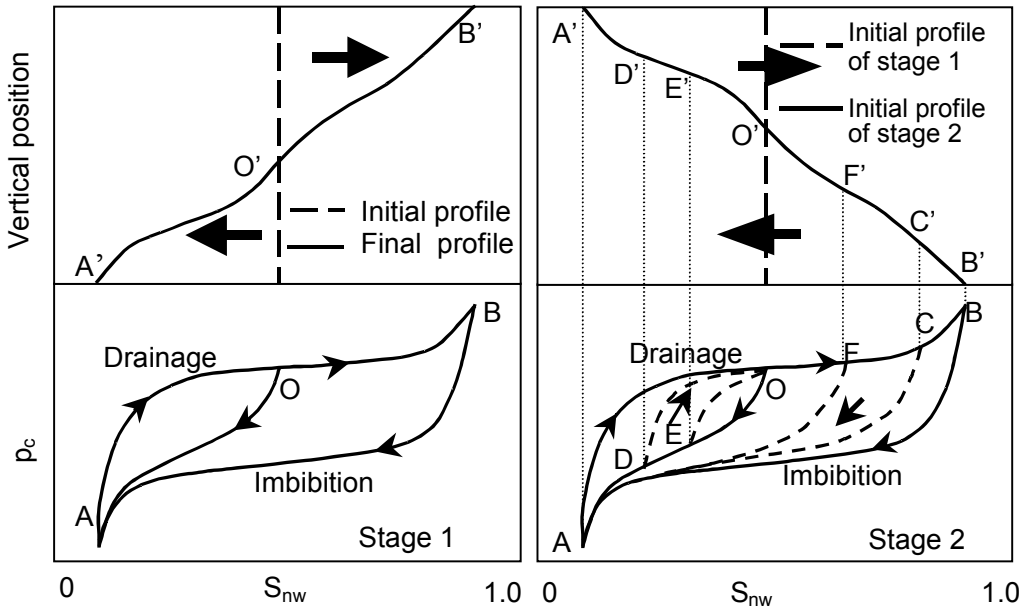

Figure 3.6: Schematic of history dependent modeling method.

CHAPTER 4

EXPERIMENTS AND MODELING

4.1 Optimization Algorithm Selection

The selection of a fast and stable algorithm is of great importance for automatic history matching. Algorithm selection for a particular case depends on the complexity and non-linearity of the problem. Several optimization algorithms listed in the last chapter were tested to find the best one for this work.

A small system is constructed for this purpose. The small system mimicks the counter-current flow process at 34 inch position in Barbu's Experiment A (Barbu et al. 1999). The size of the system is 5.0 cm by 5.0 cm with a grid of 20×20 (**Figure 4.1**). There are two mobile phases (oil and gas), and a third phase (water) at its residual. For given capillary pressure and relative permeabilities, 9 saturation profiles (**Figure 4.2**) are generated with a reservoir simulator (Eclipse® 100). The saturation profiles are the average horizontal projections of the core at different times. These 9 saturation profiles are assumed to be the experimental data with known properties such as relative permeabilities and capillary pressure. The optimization method is applied to find these properties and the initial guesses are arbitrarily chosen.

Figure 4.3 shows the capillary pressure curve used for algorithm selection. This curve was obtained by adjusting the vertical final saturation profile to the right range (Al-Wadahi et al. 2000) and it is fixed for this case. Only gas and oil relative permeabilities are adjustable. The power law form was used for relative permeability curves, in which

there are four parameters **a**, **b**, **c**, **d** according to Equation (3.18) with **a** and **b** for oil and **c** and **d** for gas. By matching the first profile in **Figure 4.2**, two relative permeability curves were obtained and with the obtained parameters, the rest of the saturation profiles were predicted. The matched and the predicted saturation profiles (black dots) are shown in **Figure 4.4**. The first saturation profile without dots is the initial condition and the one next to it is the profile used in history match. The rest are predicted. All the profiles from simulator are well matching the synthetic experimental data. **Figure 4.5a** shows the relative permeability curves including the initial guess, the target and the curves obtained from history matching with the Steepest Descent method. The obtained gas relative permeability curve overlaps the target curve but there is a little gap between the oil relative permeability curve and the target curve. But this small difference does not affect predictions. The matching profiles for other methods are essentially the same as in **Figure 4.4**. The match is so good that there is no difference between different algorithms. Therefore, the matching profiles other than the Steepest Descent method are not presented. The relative permeabilities for the Gauss-Newton method and the Levenburg-Marquardt method are shown in **Figures 4.5b-c**, respectively. The initial guess can be arbitrarily chosen, but the closer it is to the target, the faster the convergence will be. The objective function as a function of the number of iterations for the three different methods is shown in **Figure 4.6**. The Steepest Descent method takes ten times larger than the Gauss-Newton method to converge and the Levenburg-Marquardt method is five times faster than the Gauss-Newton method.

The Steepest Descent method is a linear search algorithm. The search directions at consecutive iterations are orthogonal. On the contour of the objective function, it is a zigzag trajectory with small steps.

The Conjugate Gradient method is as slow as the Steepest Descent method. Because the Conjugate Gradient method has a quadratic convergence property, it is fast to converge when the problem is quadratic or near quadratic. The problem posed in this research is far more complicated than quadratic. Hence the Conjugate Gradient is not a good choice.

The rest of the algorithms are based on the Newton Method, which holds second order convergence properties. The difference between them is how to approximate the Hessian matrix with first order of derivatives.

The Variable Metric method, also called the Quasi-Newton method, is a multivariable secant method, which uses the first order of derivatives in two consecutive steps to approximate the second order derivatives (Hessian matrix). The one-dimensional problem is schematically shown in **Figure 4.7**. The first graph (a) shows the objective function *J* without noise. There are two points on each curve representing two points for two consecutive steps. In the Variable Metric method, the second order derivative $\frac{d^2J}{da^2}$ at point B is approximated with the first order derivatives at point **A** and point **B**:

$$\left(\frac{d^2J}{da^2}\right)_B = \frac{(dJ/da)_A - (dJ/da)_B}{a_A - a_B} \tag{4.1}$$

If the curve is smooth and approximately linear such as the one in **Figure 4.7a**, Equation (4.1) yields a good approximation. The slopes of the curve at the two points are very

close to each other. But if the problem is nonlinear or with a lot of noise (**Figure 4.7b**), the slopes at the two points are too different to approximate the second order derivative and Equation (4.1) fails to represent the second order derivative at point **B**. The Variable Metric method failed to converge in this specific study. The possible reason for this failure is that the problem is too complicated and nonlinear to approximate the Hessian matrix with first order derivatives of two consecutive steps. The Gauss Newton method also uses the first order derivatives to approximate the Hessian matrix, but it uses the same point, so the difficulties in the Variable Metric method do not exist in the Gauss Newton method. The Steepest Descent method is stable but is too slow to be applied to a large system. The Gauss Newton method is fast, but it is not stable if the step size is large. The Levenburg-Marquardt method can be viewed as an improved Gauss-Newton method, which combines the advantages of the above two methods (fast and stable). In the Levenburg-Marquardt method, when the control parameter, λ, is very large, it collapses to the Steepest Descent method and when $\lambda = 0$, it is the Gauss Newton method. From the above analysis, it can be concluded that the Levenburg-Marquardt method is the best option for this work. For more complicated problems, λ is set to a large value to make the process stable and for simple cases, λ is set to small value to reduce the convergence time. The disadvantage of this method is that it has two free variables λ and step size α, which makes the optimization more complicated. The values for these two parameters mainly rely on experience.

The relationship of the above three algorithms (Steepest Descent method, Gauss Newton method and Levenberg Marquardt method) can also be reflected by the trajectory

of the model parameters against iteration number shown in **Figures 4.8a-c**. In these figures, **a**, **b**, **c** and **d** are model parameters and **a'**, **b'**, **c'**, **d'** are the targets. In the Steepest Descent method (**Figure 4.8a**), model parameters steadily converge to the targets except during the first few iterations. The Gauss Newton method is not as stable as the Steepest Descent method, which can be seen from the parameters trajectories (**Figure 4.8b**). This method could be faster if appropriate step size is chosen. The Levenberg-Marquardt method is much faster than the above two methods. Model parameters of the last iteration (the 10^{th} iteration in **Figure 4.8c**) are closer to the targets than the other two methods.

Global algorithms were not tried. Usually they are considered to be very slow, and are close to exhaustive search in the feasible parameter domain.

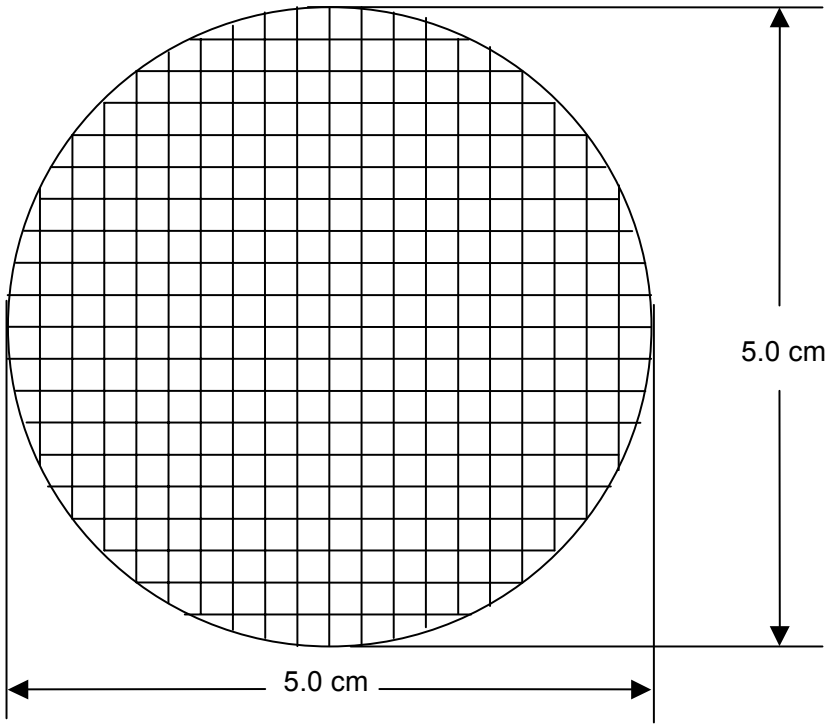

Figure 4.1: Grid system for the small synthetic case.

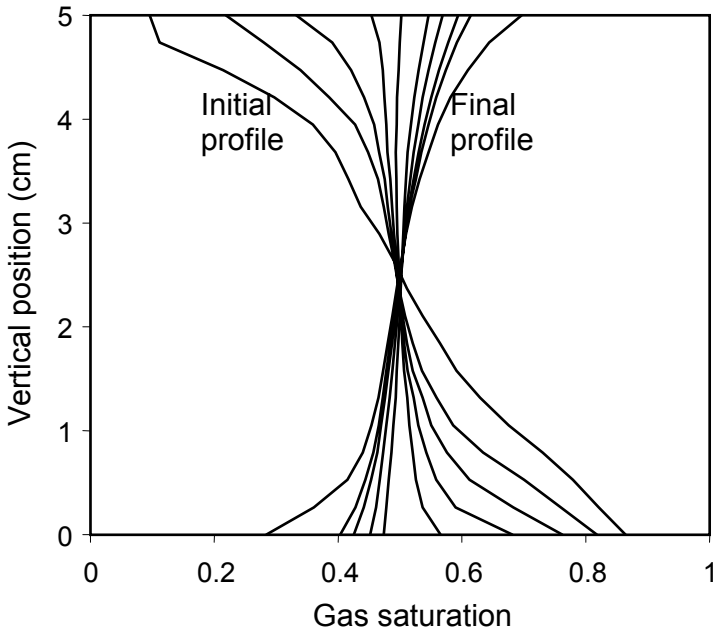

Figure 4.2: Saturation profiles of synthetic experimental data.

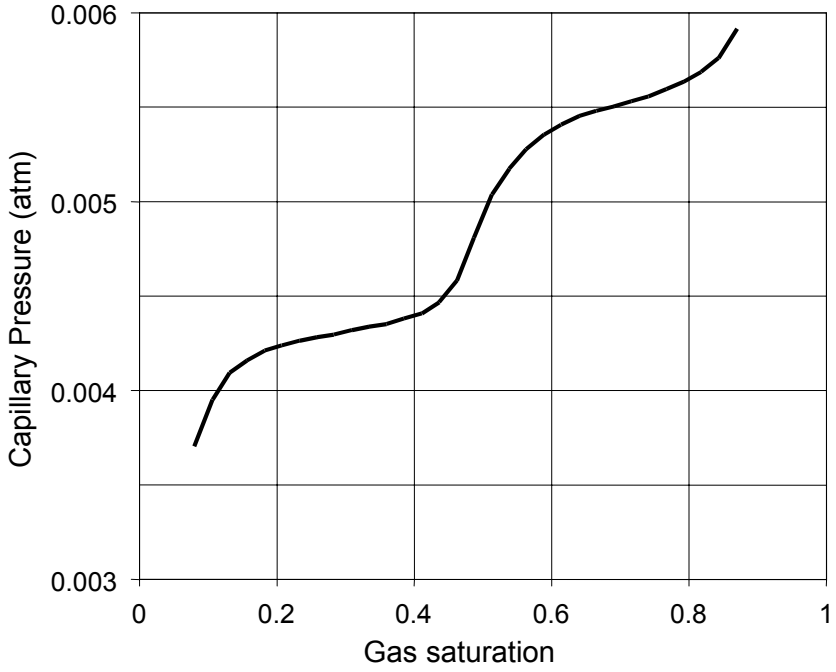

Figure 4.3: Capillary pressure curve for algorithm selection.

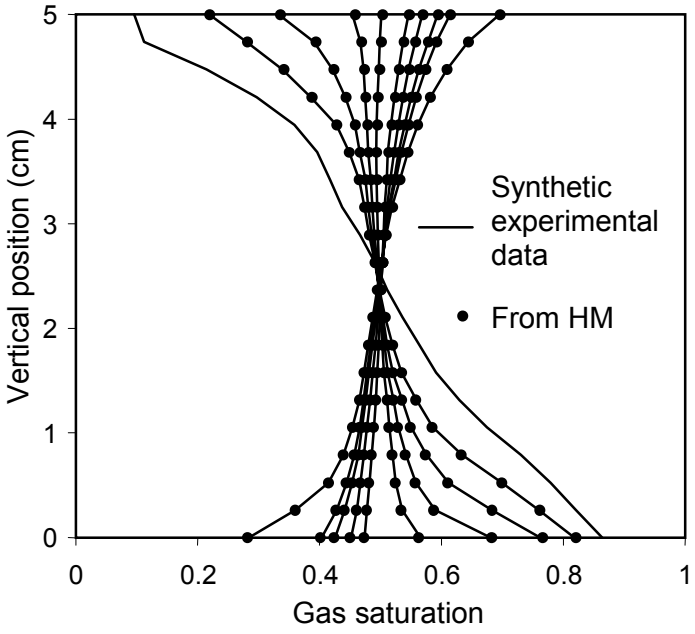

Figure 4.4: Saturation profiles match from the Steepest Descent method.

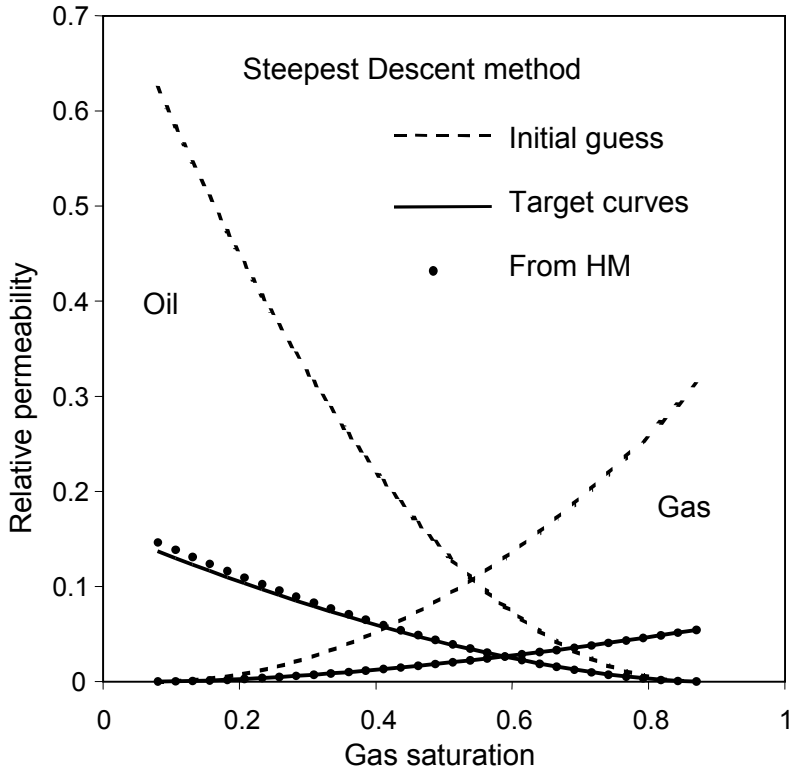

Figure 4.5a: Relative permeability curves from the Steepest-Descent method.

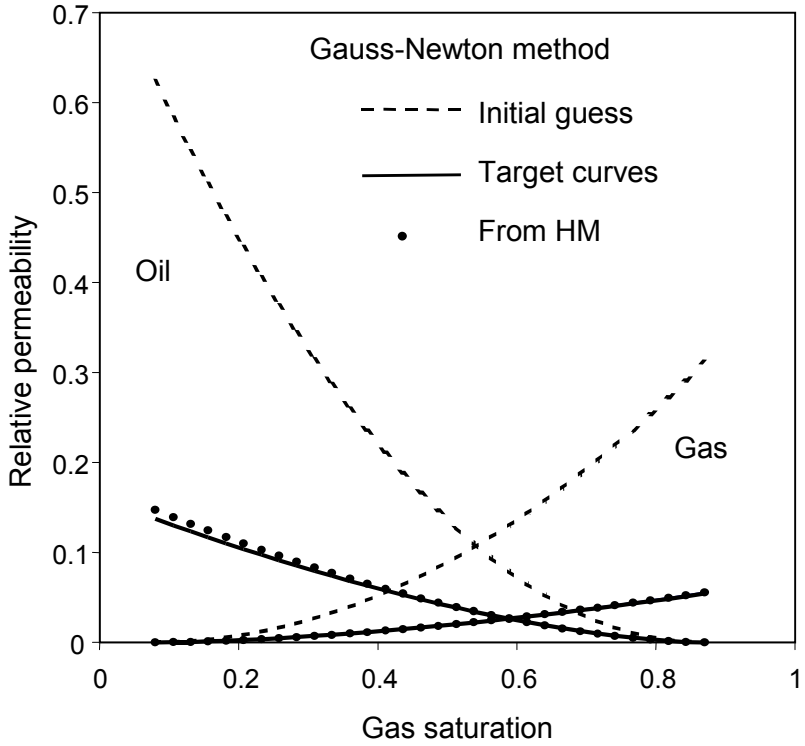

Figure 4.5b: Relative permeability curves from the Gauss-Newton method.

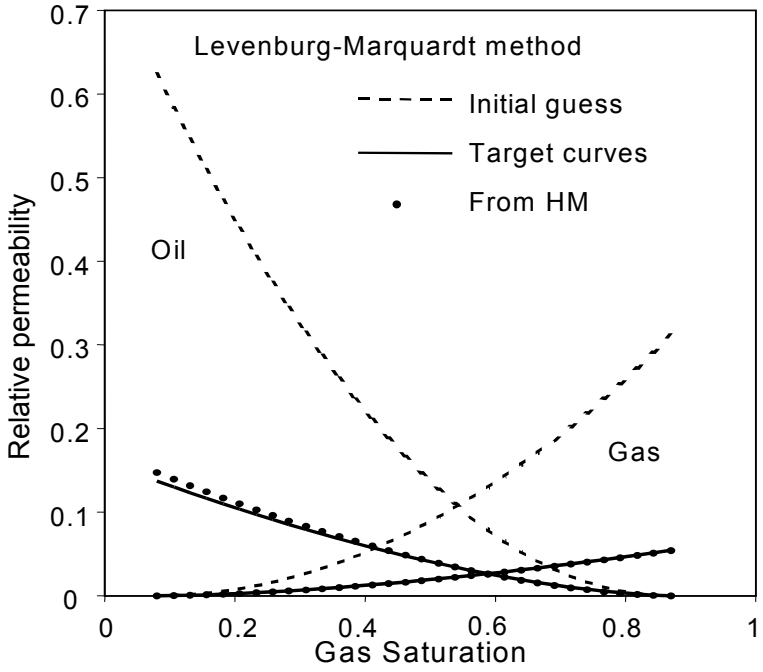

Figure 4.5c: Relative permeability curves from the Levenburg-Marquardt method.

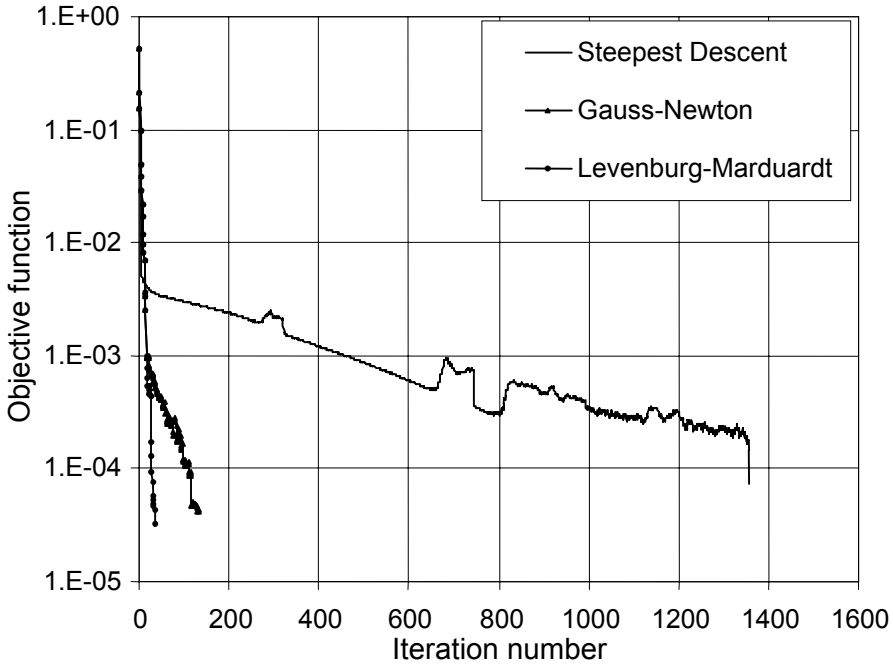

Figure 4.6: Objective function versus iteration number for different algorithms.

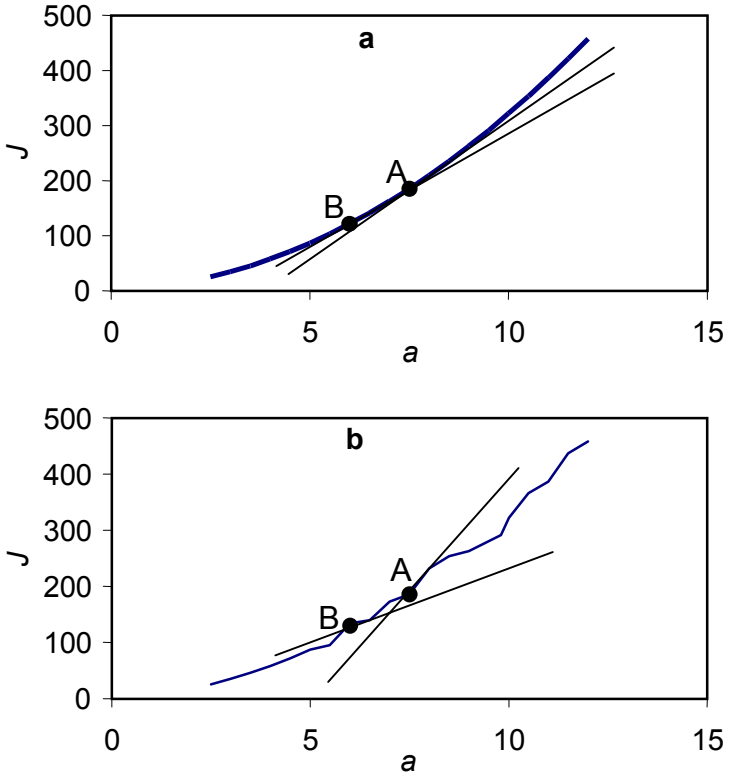

Figure 4.7: Schematic of the Variable Metric method.

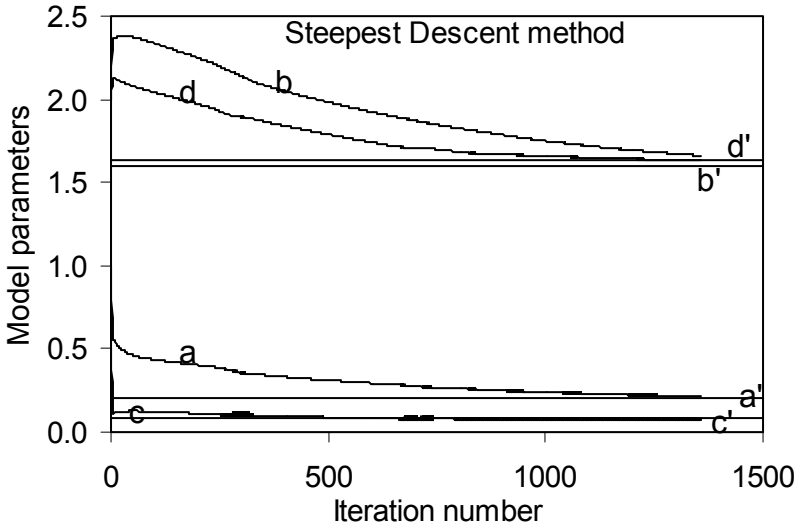

Figure 4.8a: Model parameters versus iteration number for the Steepest Descent method.

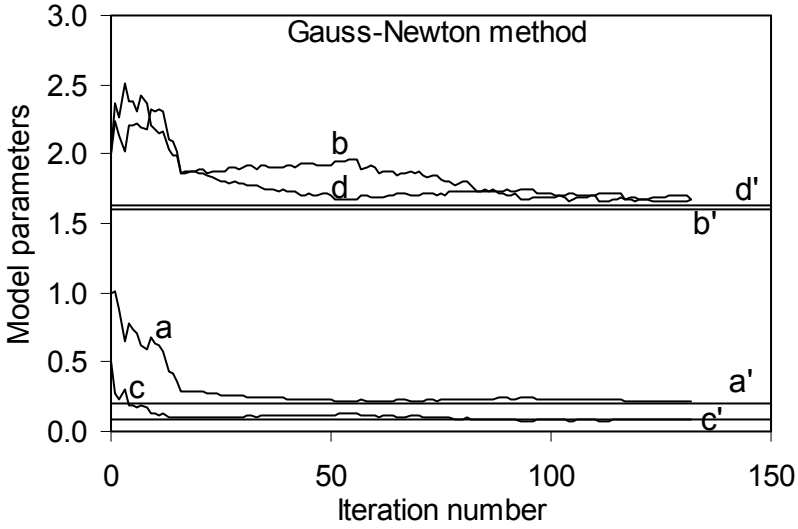

Figure 4.8b: Model parameters versus iteration number for the Gauss Newton method.

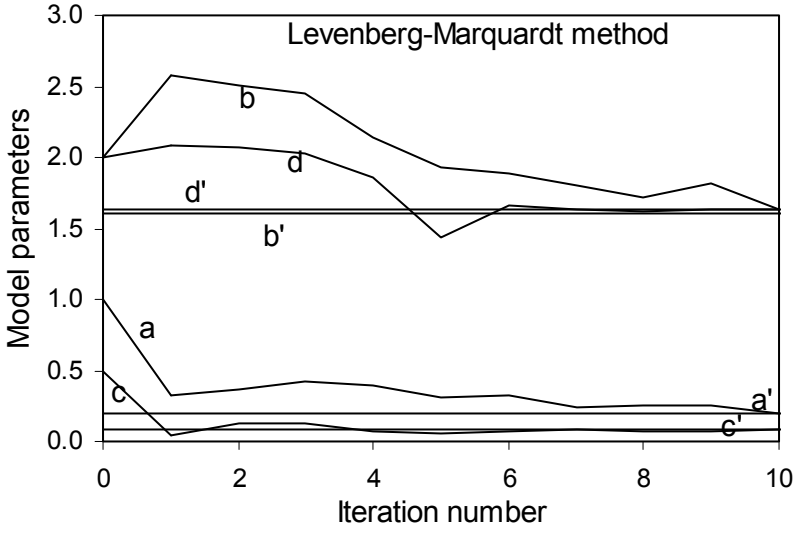

Figure 4.8c: Model parameters versus iteration number for the Levenberg-Marquardt method.

4.2 Method Validation

In order to apply it to experimental data, the Levenburg-Marquardt method was validated with a set of synthetic experimental data. The capillary pressure curve is fixed in algorithm selection, but both capillary pressure and relative permeabilities of the core sample are not available, so it is desirable to extract both parameters simultaneously from the experimental data with history matching. There are three adjustable curves in this validation process: two relative permeability curves (gas and oil) and one capillary pressure curve. The capillary pressure and relative permeability curves are known for the synthetic experimental data. The parameters obtained from history matching are compared with these target curves. If they match well, the method is validated. In this process, all the 9 profiles are used in the matching process. **Figure 4.9** shows the target relative permeability curves and the ones obtained from history matching and they have a satisfactory match. Also included in this figure are the initial guesses, which are far from the final match. The initial guesses are arbitrarily selected and they do not have to be close to the target. Several tests were taken with different initial guesses, and all had the same good match verifying the stability of the history matching method. **Figure 4.10** shows the match of the capillary pressure curves.

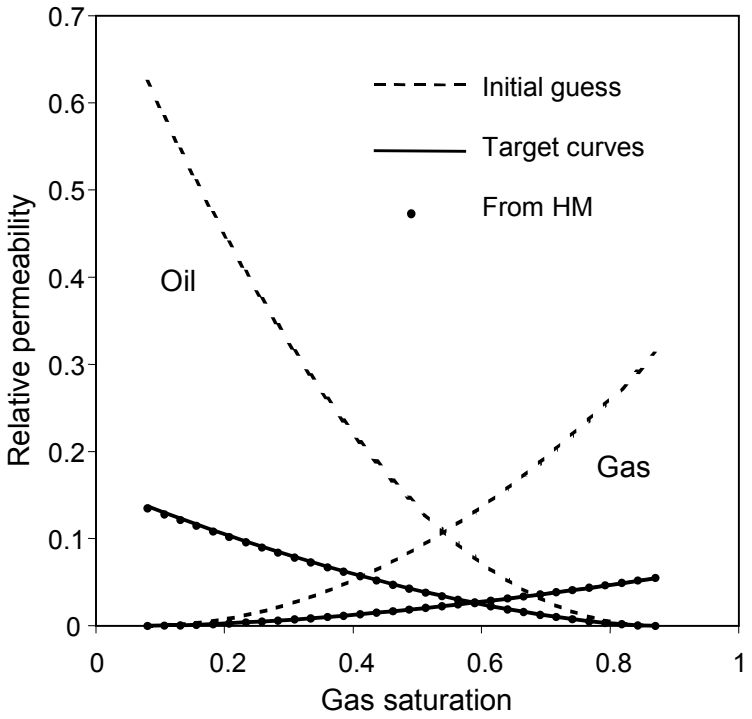

Figure 4.9: Relative permeability curves for validation with the Levenburg-Marquardt method.

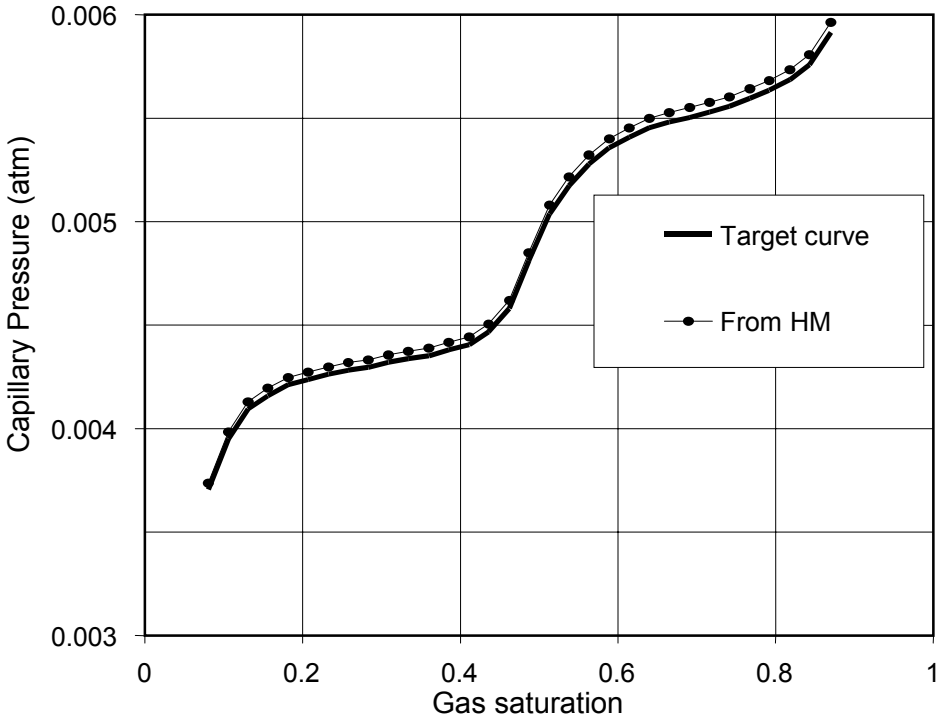

Figure 4.10: Capillary pressure curve for validation with the Levenburg-Marquardt method.

4.3 Modeling of Barbu's Experiments

4.3.1 Experiments

The focus of Barbu et al.'s (1999) work was to develop three-phase saturation structures driven by viscous, gravitational, and capillary forces. In the displacement experiments, an oil bank was successfully created and flow behavior around and inside the oil bank was studied. The core sample was made of glass beads and three immiscible fluids were used: water, benzyl alcohol (oil), and decane (gas). The properties of these fluids are summarized in **Table 4.1**. The glass bead core is 36 inches in length and 2 inches in diameter. The experimental procedure (Experiment A) is summarized schematically in **Figure 4.11**.

Table 4.1: Fluid properties (Al-Wadahi 1994).

	Density (g/cc)	Viscosity (cp)	Interfacial tension (dyne/cm)	
Water	1.03	1.19	W-BA	3.04
Benzyl alcohol	1.03	5.44	BA-D	1.83
Decane	0.77	1.14	W-D	6.05

The experiment started by applying vacuum to the sample (1). The core was then saturated with water (2). Benzyl alcohol was injected to decrease water saturation to its residual (3). Benzyl alcohol and decane were injected simultaneously until steady-state conditions were obtained (4). Then a dynamic waterflood was performed. An oil bank was formed after 0.3 pore volumes of water were injected (5). All the above steps were

performed while the core was in the vertical position. The core was then placed in the scanner horizontally and several scanning sequences were taken (6). The core was rotated 180° around its long axis (7) and the counter-current flow process was monitored with sixteen scanning sequences (8). Then another 0.1 pore volumes of water were injected (9) and fluid saturation was monitored (10). Finally, the waterflood was completed (11) and a final scan was performed (12).

Figure 4.12 shows the saturation distribution along the sample reconstructed from the end of step 6. The inlet is at the left side. The benzyl alcohol saturation varies from low values (white) to high values (dark). In the middle of the figure, there is an oil bank (black) and a decane tongue (white) above it. **Figure 4.13** shows the comparison of saturation distribution before and after rotation (step 8). The position of the oil bank did not change and a new decane tongue formed at the top of the oil bank. In this step, scans were taken at five positions shown in **Figure 4.12** with thin vertical lines (at 19, 20, 24, 24.3 and 34 inches from the injection end of the core). Each location was scanned 16 times during a period of 71.2 hours. Counter-current flow due to gravity and capillary force occurred at this step as well as in step 6. The following modeling is going to focus at 34-inch position. At this position, there are only two mobile phases: benzyl alcohol and decane. Water is at its irreducible. **Figures 4.14a-b** show the images of the saturation distribution at this position from step 6 (Stage 1) and step 8 (Stage 2), respectively. The images show the decane saturation distribution during counter-current flow. Stage 1 started with quite uniformly distributed fluids saturation in the core. This saturation distribution structure was formed when the core was in the vertical position (steps 1-5). After it was placed in the horizontal position, fluids segregate due to gravity. Decane

(light phase) started to flow upward and benzyl alcohol (heavy phase) counter-currently flowed downwards. **Figure 4.15a** shows the decane saturation profiles of Stage 1. These saturation profiles are horizontal projections (at each level of the sample, all the saturations are averaged to one value). After Stage 1 finished, the core was rotated 180°, decane (light phase) flowed upward from bottom and benzyl alcohol (heavy phase) counter-currently flowed downwards. The decane saturation profiles of Stage 2 are shown in **Figure 4.15b**. There is no flow in the horizontal direction along the core at this position, which can be seen from **Figure 4.16**, which shows no average saturation change in this plane during Stage 2. This validates the application of a 2-D model of counter-current flow process to simulate the experimental results at this position.

4.3.2 Modeling

Al-Wadahi et al. (2000) modeled the counter-current flow process at the 34-inch position (ahead of the shock) using a neuro-simulation approach. They found the best relative permeabilities and capillary pressure that describe the counter-current process at this position of the core using a neural network model. It was concluded that the counter-current relative permeabilities are lower than the co-current relative permeabilities for the same system. The shape of the capillary pressure is similar to that of the final vertical saturation profile, which is different from the traditional Leverett *J* function. Neuro-simulation proved to be an effective tool in this study. The disadvantage of this method is that it is based on interpolation and can only produce parameters in pre-selected ranges.

The Levenburg-Marquardt method was selected as the best algorithm for the current study and the validation proved that history-matching method can be used to

accurately extract the relative permeabilities and capillary pressure from synthetic experimental data. In the following, the counter-current flow at the same position (34-inch position in Barbu et al. 1999) is modeled using history-matching method with the Levenburg-Marquardt optimization algorithm.

Two modeling methods were implemented to simulate this process. The first method is called the "single pc method", in which one capillary pressure curve and one pair of relative permeability curves (oil and gas) were used. The second method is called the "saturation history dependent simulation method". There are two pairs of relative permeability curves (imbibition and drainage) and for each pixel of the core sample, there is a capillary pressure curve obtained from the capillary hysteresis loop.

In the first method – single pc method, the relative permeabilities are represented in a power law form using Equation (3.18). The capillary pressure curve is constructed based on the final saturation profile using Equation (3.21). Through an optimization algorithm (Levenburg-Marquardt method), these coefficients, starting from some initial guesses, are adjusted according to history matching procedures until the simulation results match the experiments. **Figure 4.17** shows how these coefficients, from the initial guess, approach the ones that give the best match of the saturation profiles and **Figure 4.18** shows the objective function decreases with the number of iterations. History matching is applied to the experimental data in Stage 2 to extract the right relative permeabilities and capillary pressure. The best match of the decane saturation profiles is shown in **Figure 4.19**. **Figure 4.20** and **Figure 4.21** show the relative permeabilities and capillary pressure curves obtained from history matching. After relative permeabilities and capillary pressure were extracted from the experimental data of Stage 2, they were

applied to Stage 1 of the same experiment. The match of saturation profiles is shown in **Figure 4.22**. The simulation can capture the general behavior of the core sample, but it does not match the experimental data very well. In the upper potion of **Figure 4.19** there is a " hint" of a fluid bank. The single pc method does not allow for the creation of a fluid bank and the resulting simulated curves are smooth. A mechanistic method is needed to model counter-current flow.

In the saturation history dependent method, the relative permeabilities are still represented in a power law form, but there are two pairs instead of just one pair for the whole system. This is because there are both imbibition and drainage processes occurring in the system at the same time. Therefore, there are one pair of drainage relative permeabilities and one pair of imbibition relative permeabilities. If only one pair of relative permeability curves is used for these two processes, it would not give the details of the flow behavior of the system. The use of a single capillary pressure curve makes the situation even worse. Capillary pressure exhibits hysteresis. The saturation along with its history decides the capillary pressure for different saturation points in the core. A mechanistic understanding about capillary pressure is presented in chapter 3. For each system, there is a family of capillary pressure curves composed of a hysteresis loop and some scanning curves inside the loop. The hysteresis loop consists of a drainage capillary pressure curve and an imbibition capillary pressure curve and inside are imbibition-scanning curves as well as drainage-scanning curves. The whole family of capillary pressure curves can be obtained from experiments, which is expensive and time consuming. To overcome the disadvantage of measuring the whole family, some investigators proposed methods to construct the capillary scanning curves from only the

hysteresis loop, which is normally measured in experiments. These methods include Killough's (1976) method and Kleppe's (1997) method. Because in Barbu's experiments, capillary pressure was not measured, history matching is implemented to extract the capillary hysteresis loop from the experimental data and the family of the capillary scanning curves are constructed using a combination of the above two methods. **Figure 4.23** shows the extracted capillary pressure hysteresis loop and the drainage and imbibition scanning curves used in the simulation. To fully understand how saturation history dependent modeling works, the saturation history of the experiment must be studied first.

Because water saturation is at its irreducible in the experiment studied here, the analysis starts at the beginning of step 4. Before this step, water was pushed out of the core until its irreducible saturation and benzyl alcohol achieved its highest saturation. With injecting benzyl alcohol and decane at the same time in step 4, decane saturation increases, which is a drainage process. As was mentioned before, benzyl alcohol represents oil and decane represents gas in the system and benzyl alcohol is the wetting phase compared to decane. In the capillary hysteresis family, the capillary pressure trajectory travels on the drainage capillary pressure curve in step 4. In **Figure 4.23**, it follows curve **ACO**. When benzyl alcohol-decane injection reached steady-state, the average decane saturation was about 50 % and the capillary pressure stopped at point **O**. In step 5 (waterflooding), capillary pressure does not change, because the saturation does not change at this position far ahead of the benzyl alcohol bank. In step 6 when the core was placed in a horizontal position, the two fluids segregated. Decane moved up and benzyl alcohol counter-currently moved down. The saturation did not change in the

middle of the core(**Figure 4.15a**), at which the capillary pressure did not change either. In the upper part, decane saturation increased, which underwent drainage process, the capillary pressure still followed the drainage capillary pressure curve **ODB** – continuing the process of step 4. But in the lower part, decane saturation decreased undergoing imbibition process, the capillary pressure followed an imbibition-scanning curve **OEA**.

In Stage 2, after the core was rotated 180°, the upper part underwent drainage process and the lower part underwent imbibition process. The capillary pressure of the system started from the capillary pressure curve **AEODB** in the loop, where it was left in Stage 1. Because the saturation in the system was different from pixel to pixel (vertical position) and the saturation histories between the lower and upper parts were different, they followed different capillary pressure paths. The lower part followed some imbibition scanning curves starting from curve **ODB** and the upper part followed some drainage scanning curves starting from the same curve **AEO**.

The two pairs of relative permeability curves are shown in **Figure 4.24**. The drainage relative permeabilities were used in the upper part, because it always exhibited a drainage process. Accordingly, the imbibition relative permeabilities were used in the lower part, because it always exhibited an imbibition process. **Figures 4.25a-b** show the final match of the saturation profiles for Stage 1 and Stage 2. The match is better than that obtained from the single pc method.

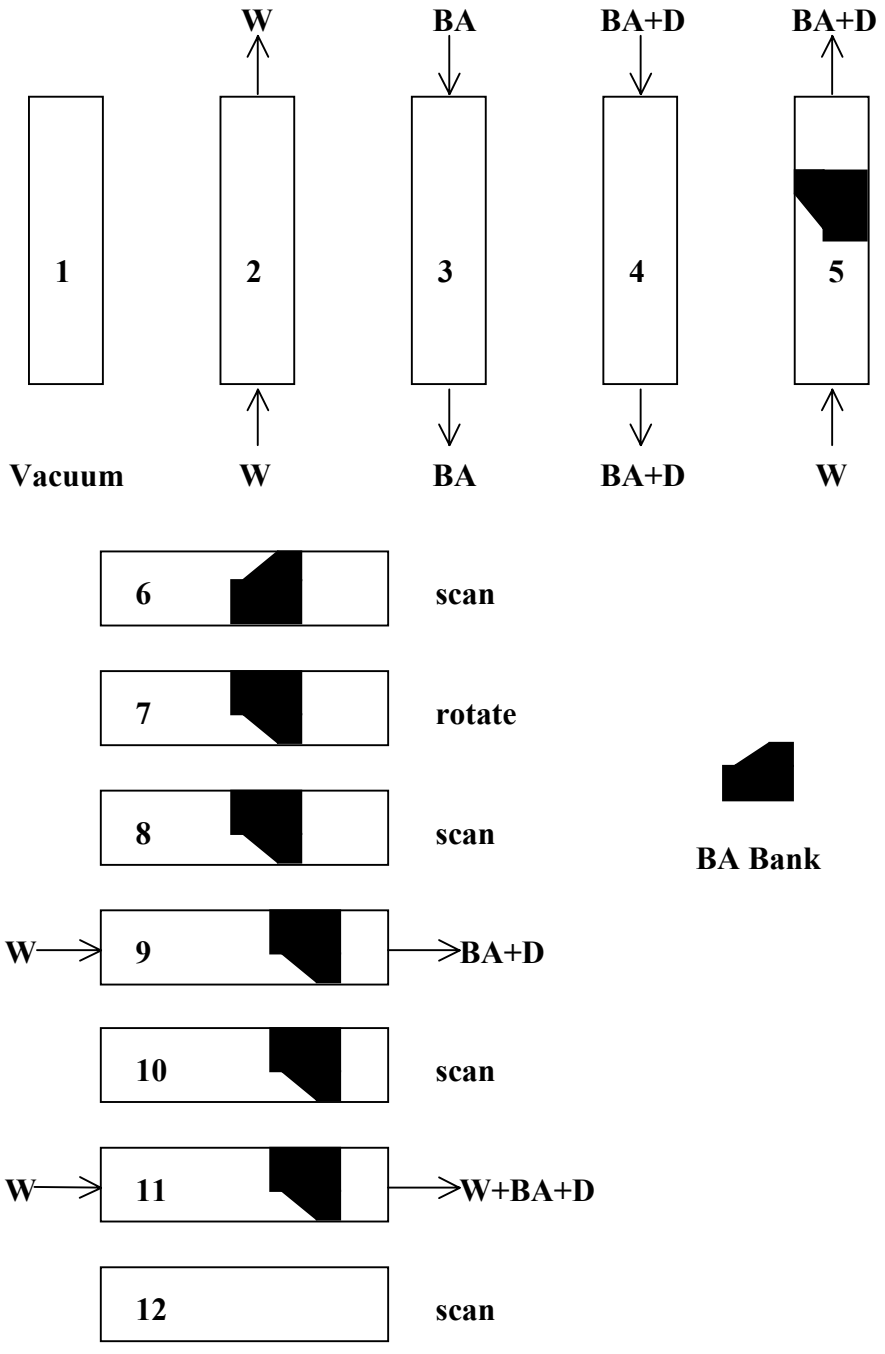

Figurer 4.11: Barbu's experimental procedure (Barbu et al. 1999).

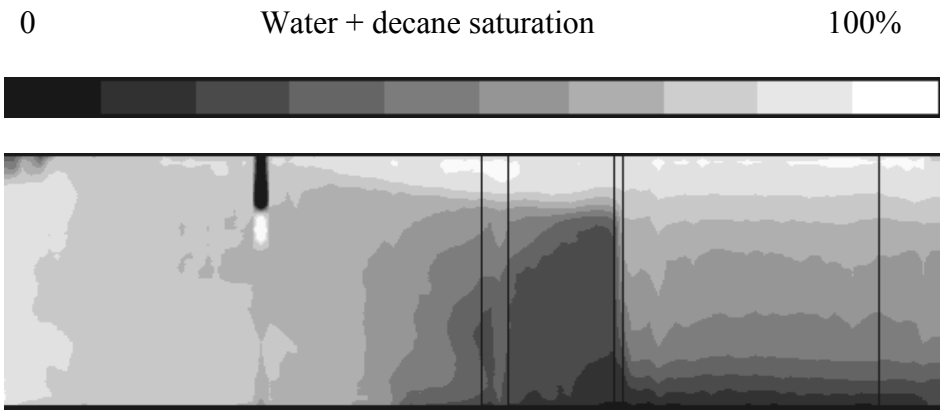

Figure 4.12: Saturation distribution from Experiment A (Barbu et al. 1999).

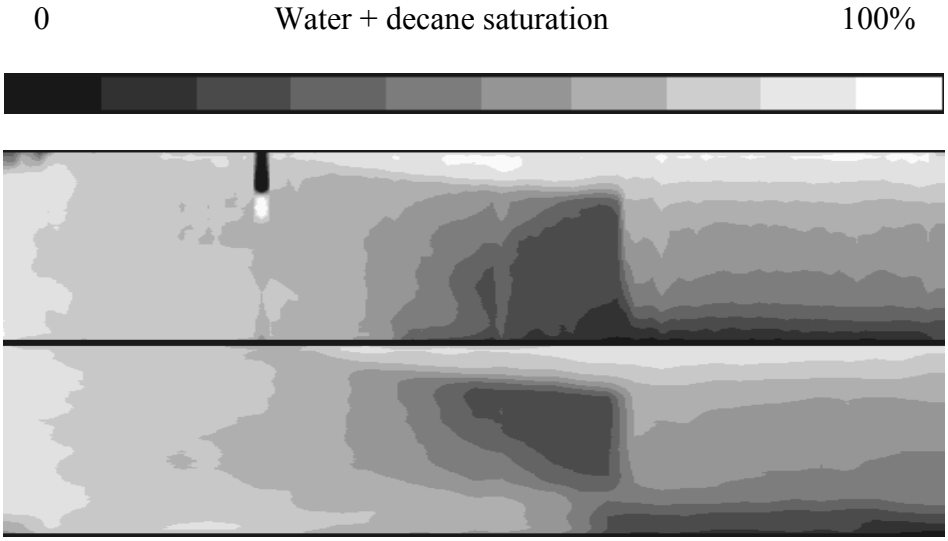

Figure 4.13: Comparison of saturation distribution before rotation and at the end of rotation in Experiment A (Barbu et al. 1999).

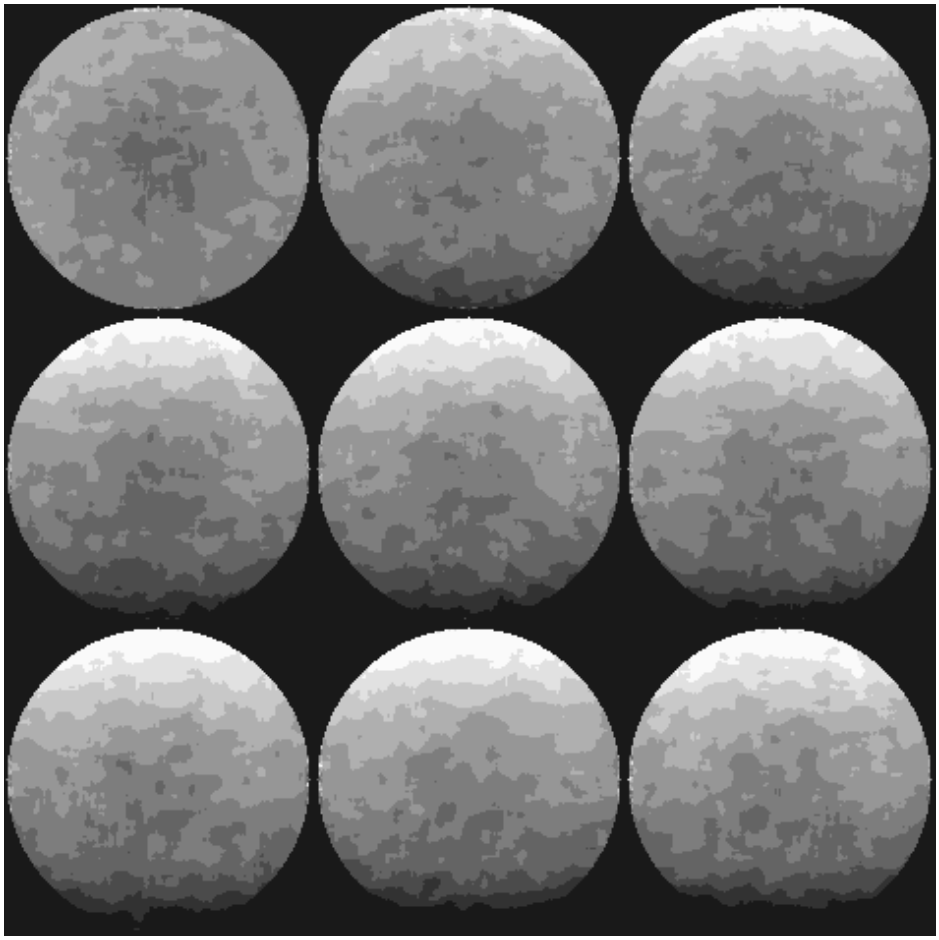

Figure 4.14a: Decane saturation distribution at 34-inch position
in Stage 1 of Barbu's Experiment A.

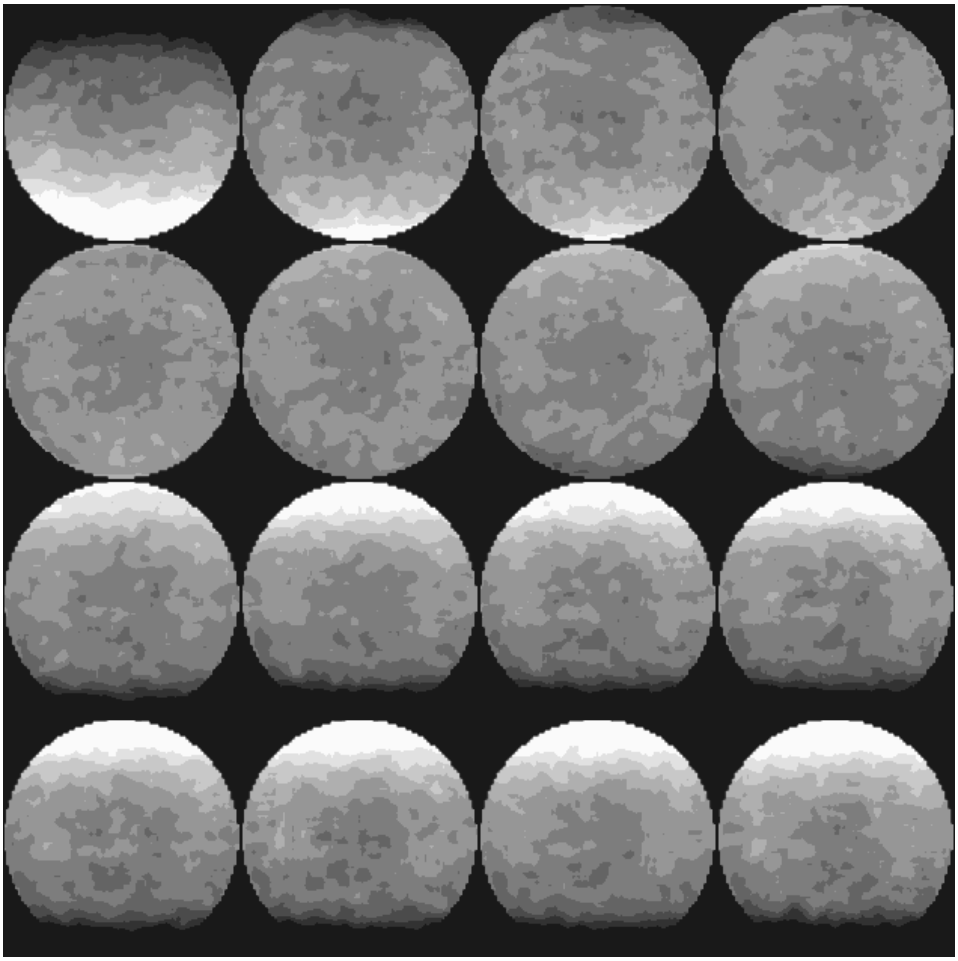

Figure 4.14b: Decane saturation distribution at 34-inch position
in Stage 2 of Barbu's Experiment A.

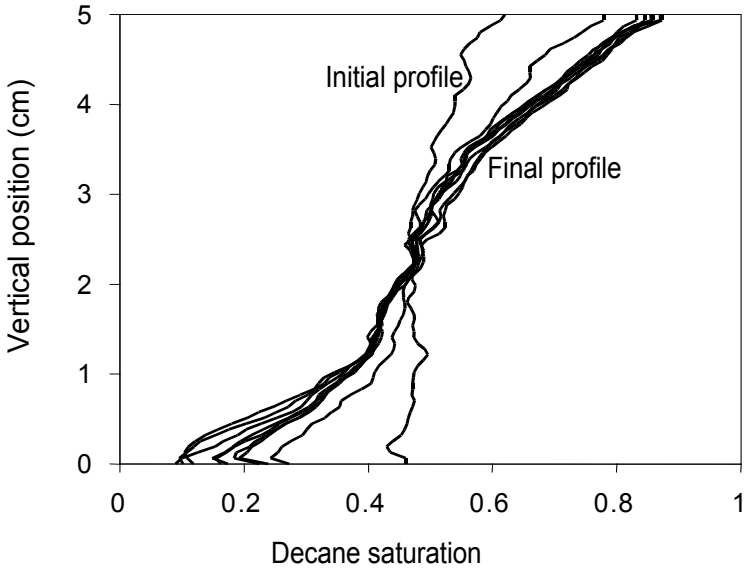

Figure 4.15a: Decane saturation profiles at 34-inch position in Stage 1 of Barbu's Experiment A.

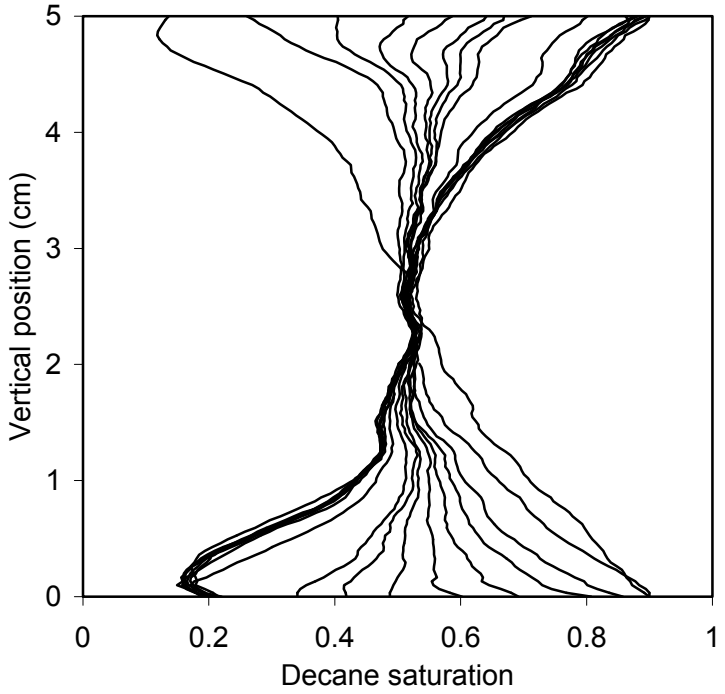

Figure 4.15b: Decane saturation profiles at 34-inch position in Stage 2 of Barbu's Experiment A.

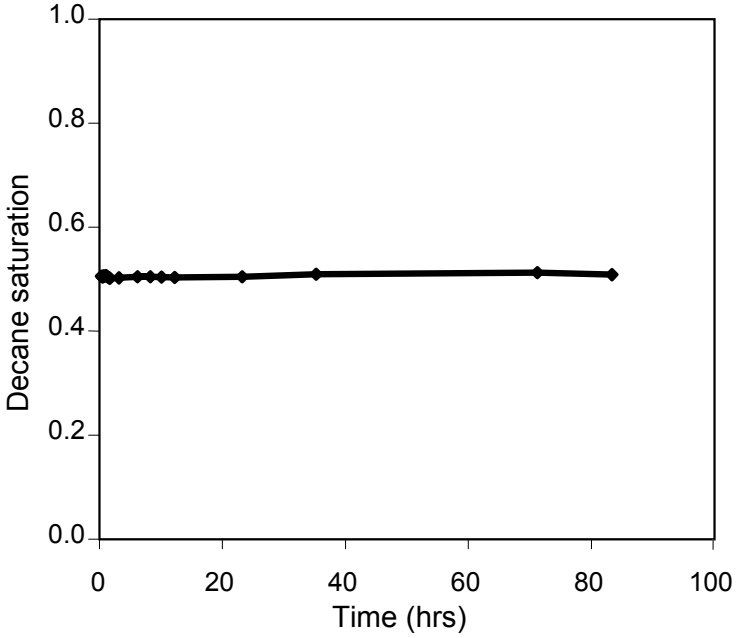

Figure 4.16: Average decane saturation at 34-inch position in Stage 2 of Barbu's Experiment A.

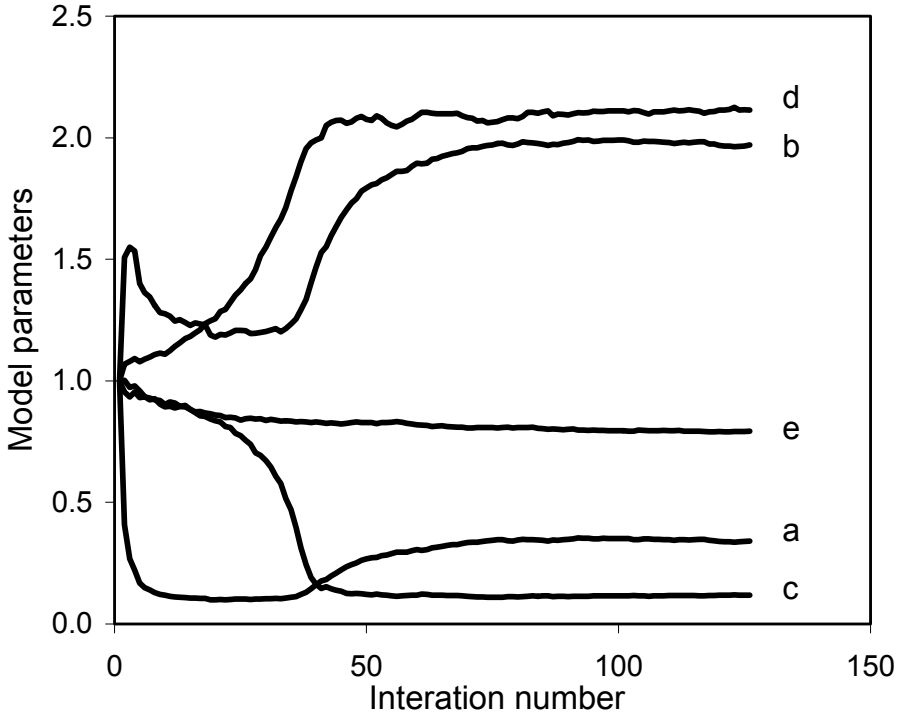

Figure 4.17: Model parameters versus iteration number for the match of Stage 2 of Barbu's Experiment A (single pc method).

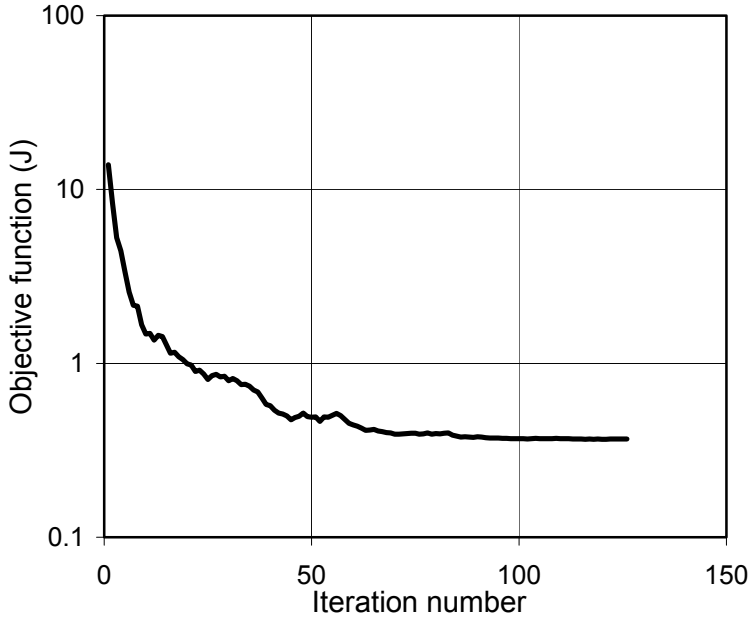

Figure 4.18: Objective function versus iteration number for the match of Stage 2 of Barbu's Experiment A (single pc method).

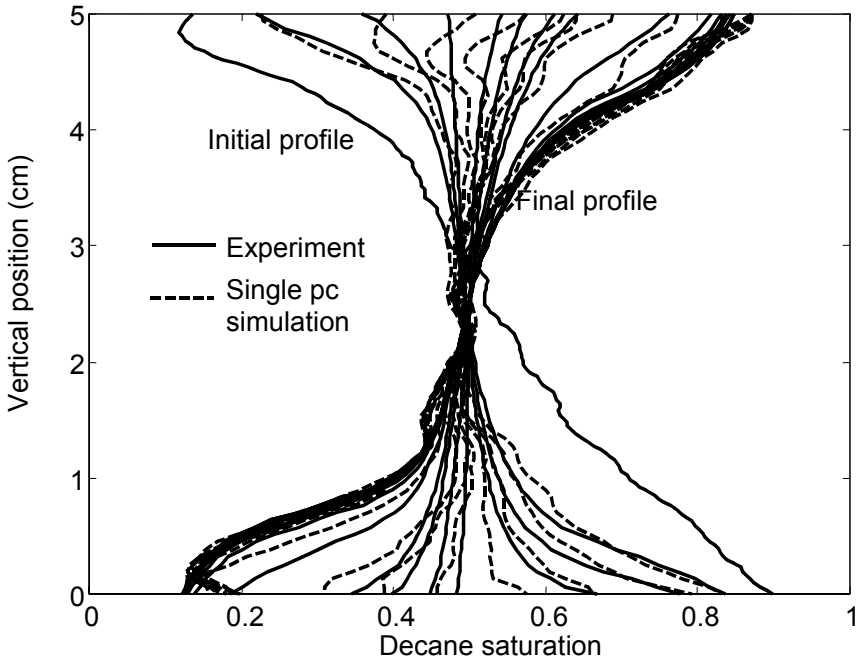

Figure 4.19: Decane saturation profiles of Stage 2 at 34-inch position in Barbu's Experiment A. The simulation was done with a single capillary curve obtained from final saturation profile.

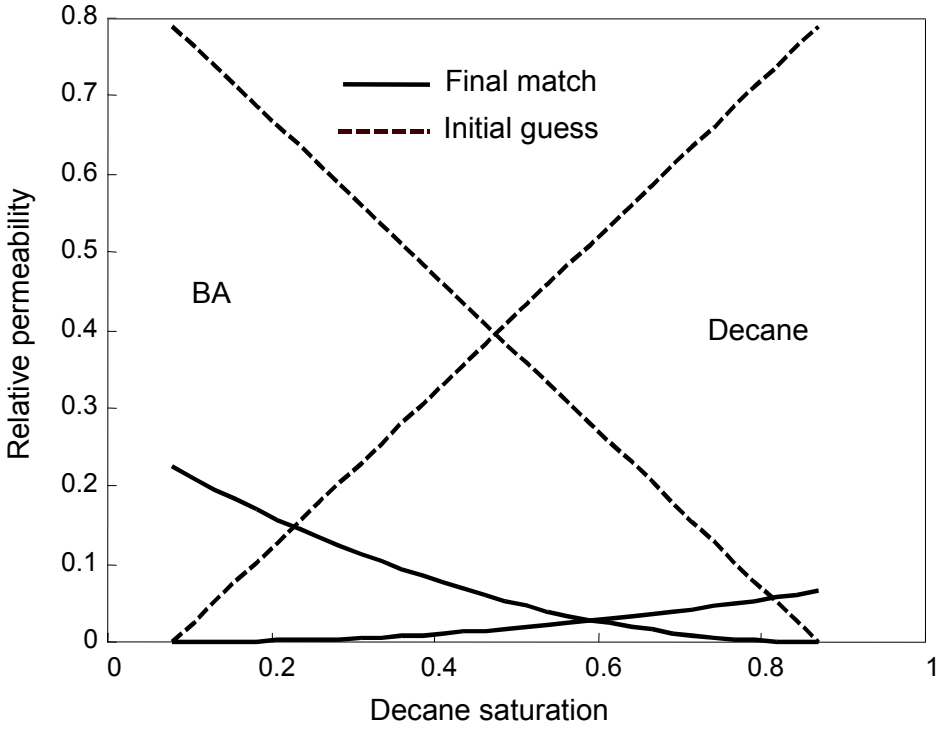

Figure 4.20: The initial guess and final match of the relative permeabilities at 34-inch position in Barbu's Experiment A (single pc method).

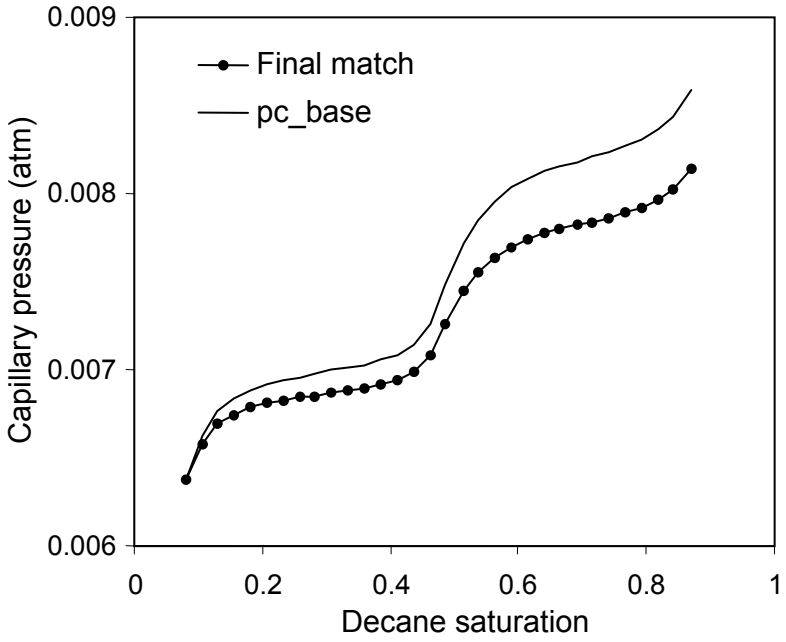

Figure 4.21: The initial guess and final match of the capillary pressure curve at 34-inch position in Barbu's Experiment A.

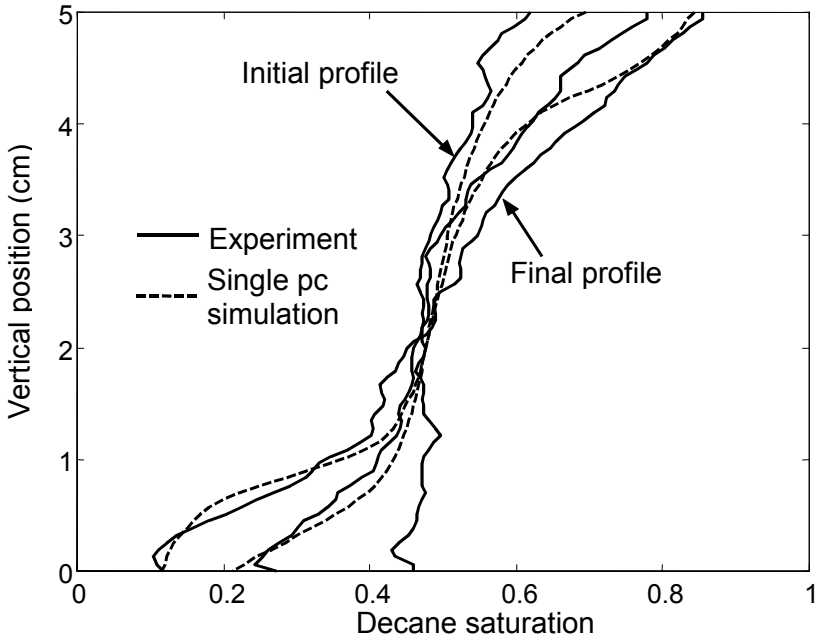

Figure 4.22: Decane saturation profiles of Stage 1 at 34-inch position with single pc simulation.

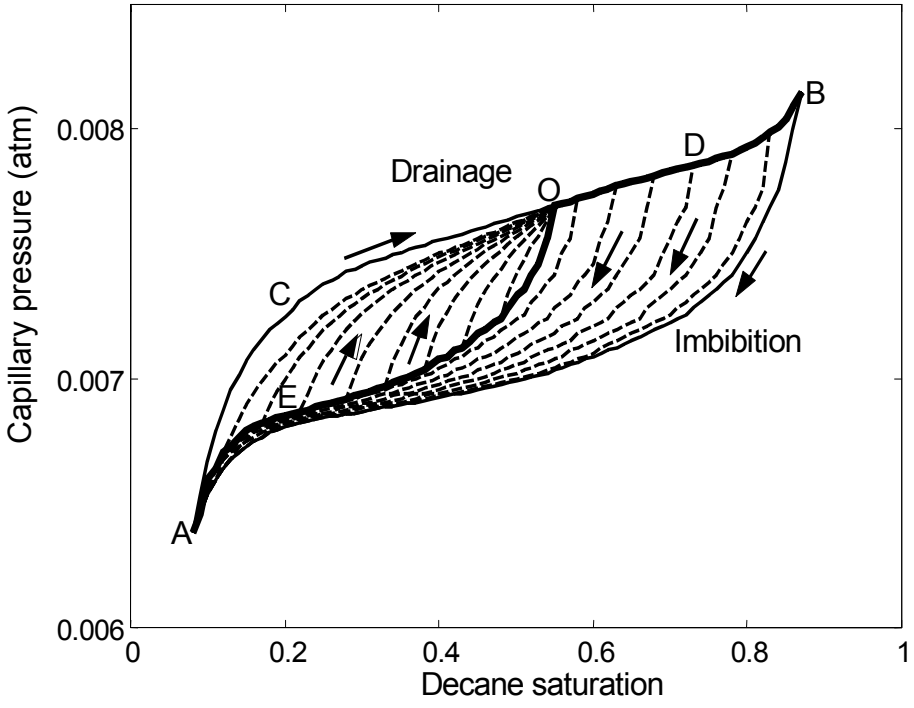

Figure 4.23: Capillary pressure hysteresis loop and the scanning curves for Barbu's Experiment A used in history dependent simulation.

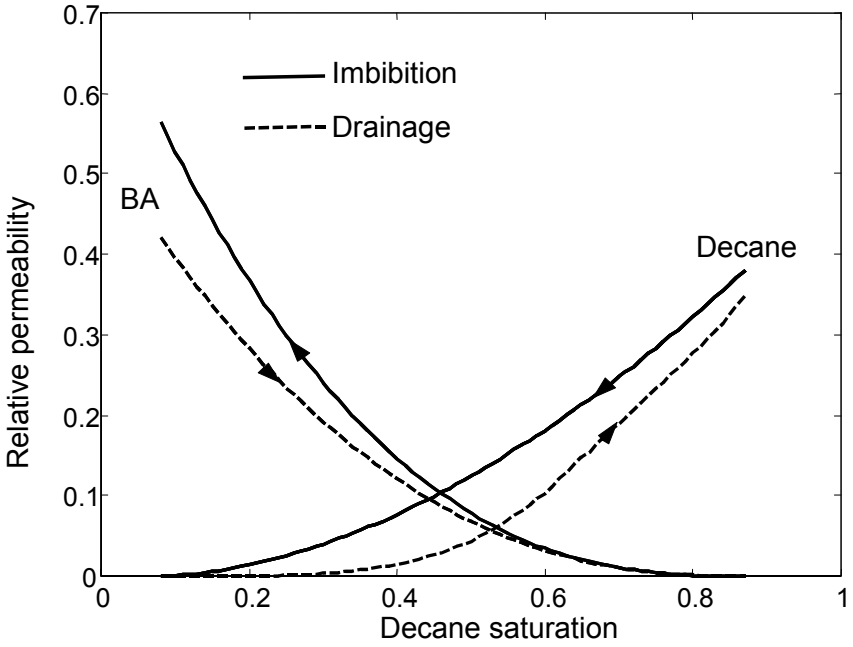

Figure 4.24: Relative permeability curves for Barbu's Experiment A used in history dependent simulation.

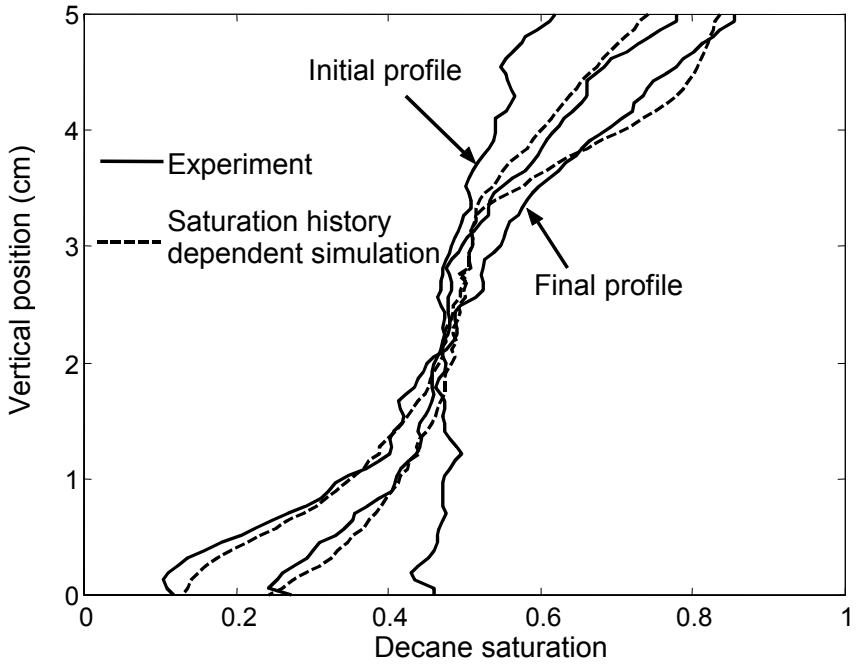

Figure 4.25a: Decane saturation profiles of Stage 1 at 34-inch position with history dependent simulation.

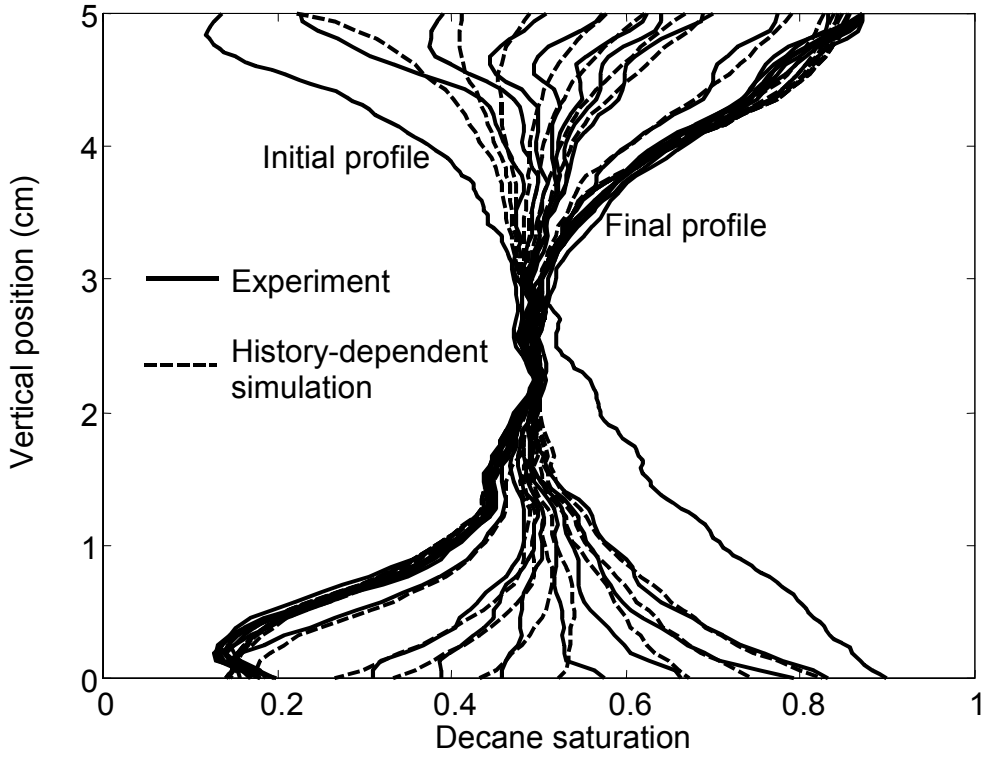

Figure 4.25b: Decane saturation profiles of Stage 2 at 34-inch position in Barbu's Experiment A with history dependent simulation.

4.4 Modeling of Karpyn's Experiments

4.4.1 Experiments

The counter-current flow experiments were done in a 10x10x1 cm closed cell made of glass beads. The fluids used in the experiments are the same as that in Barbu's experiments. They are three immiscible fluids: distilled water, benzyl alcohol and decane, representing water, oil and gas respectively. The saturation distribution of the core sample was mapped with an X-ray CT scanner. A complete description of the experiments is given in Karpyn (2001) and the following is only a brief overview.

The experiments have three major stages: pre-saturation, Stage 1 and Stage 2. The schematic of the experimental procedure is shown in **Figure 4.26**. In the pre-saturation stage, the core was first vacuum saturated with water. Then the core was flooded with benzyl alcohol to obtain irreducible water saturation. Benzyl alcohol and decane were then injected simultaneously until steady-state was achieved. The core was scanned after vacuum and during flow process to ensure the homogeneity of the core as well as fluid distribution. In Stage 1, the system was closed and the fluids were segregated until equilibrium was obtained. The segregation is a counter-current flow process starting from an even initial saturation distribution. Several scans were taken during the segregation process. At the end of this stage, the heavy wetting fluid – benzyl alcohol stayed at the bottom while the light non-wetting fluid - decane stayed at the top of the core. In Stage 2, the core was rotated 180º around the horizontal axis to initiate another counter-current flow process, which started from a non-even initial saturation distribution. Several scans were taken to monitor this process.

Figures 4.27a-b show the CT images of the core for Stage 1 and Stage 2, respectively. The images show the fluid distribution during the counter-current flow process. Stage 1 started with uniformly distributed fluids saturation in the core. The heavy phase benzyl alcohol (black) moved down to the bottom due too gravity and the light phase decane (white) counter-currently moved up to the top of the core at the end of segregation (**Figure 4.27a**). Decane and benzyl alcohol also exchanged position in Stage 2 after the core was rotated 180º (**Figure 4.27b**). The decane saturation profiles of Stage 1 and Stage 2 are shown in **Figures 4.28a-b**. There is a benzyl alcohol bank at the top part of the core in Stage 2 (**Figures 4.28b**), which also can be seen in the images (**Figure 4.27b**). In both stages, there is a decane shock at the bottom of the core, below which resides the benzyl alcohol zone (**Figures 4.28a-b**).

4.4.2 Modeling

The modeling of Karpyn's experiments started with matching the experimental data of Stage 1 using a single capillary pressure curve. **Figure 4.29** shows the final match of saturation profiles. The relative permeabilities and capillary pressure obtained from history matching are shown in **Figure 4.30** and **Figure 4.31**, respectively.

Because both drainage and imbibition processes exist in the same system at the same time, two pairs of relative permeability curves were used. One pair was drainage relative permeabilities used in the upper half of the core while the lower half used the imbibition relative permeabilities.

These parameters were then applied to Stage 2, but it resulted in unsatisfactory saturation profiles shown in **Figure 4.32**. In the experiments, there was a benzyl alcohol

bank at the top of the core in Stage 2 (**Figures 4.28b**) and the decane saturation extended to a very high value at the top. From simulation results (**Figure 4.32**), there is only a tail of the benzyl alcohol bank and the decane saturation of the upper wing of the bank never passes the average saturation during the formation of the benzyl alcohol bank. This is because the capillary curve in this method is a S-shaped curve with a very high gradient in the middle part of the curve, which restricts fluids to flow that saturation section. Then saturation history dependent modeling is applied to Stage 2, and satisfactory decane saturation profiles are obtained using the relative permeabilities got from Stage 1. The match of decane saturation profiles is shown in **Figure 4.33**.

The capillary pressure hysteresis loop is obtained with history matching. The scanning curves inside the capillary hysteresis loop are constructed by the combination of the Kleppe and the Killough methods. From **Figure 3.5**, Both the Kleppe and the Killough methods provide a good match for imbibition-scanning curves with the experiments, but the Killough method gives a better match for drainage-scanning curves than the Kleppe method does. In the Killough method, parameter ε may be different for drainage and imbibition-scanning curves and the specification of this parameter requires experiments or experience. A combination of these two methods was used in simulation, in which imbibition-scanning curves are constructed by the Kleppe method and drainage-scanning curves were constructed by the Killough method with ε equal to 0.1. The capillary hysteresis loop with the scanning curves constructed using this combination of methods is shown in **Figure 4.34**. The drainage-scanning curves converge to point **O**. This is consistent with the Everett's independent domain theory (Everett, 1967): "*If the system were taken through a series of pressure oscillation of decreasing amplitude, after*

nth pressure reversal, the system moves toward the point at which the (n-1)th reversal occurred, and if the system is carried through this point, it moves toward the (n-3)th reversal point and so on." The scanning curves constructed with the Kleppe method do not converge to point **O** and it created a discontinuous path for the drainage saturation points. This discontinuity created an artificial "bulge" in the late time saturation profile at the top of the core.

To understand why the simulation of Stage 2 using the parameters obtained from the Stage 1 did not yield satisfactory saturation profiles, the flow process, i.e. the saturation history, should be introduced tied to the capillary hysteresis.

Similar to the flow process in Barbu's experiments, benzyl alcohol was at its highest saturation, after water was pushed out of the core to its irreducible saturation. In the capillary hysteresis loop, it is at point **A**. Then simultaneous injection of benzyl alcohol and decane reduced benzyl alcohol saturation, which is a drainage process. It followed the drainage capillary pressure curve **ACODB** in the hysteresis loop. After it reached steady-state, it arrived at point **O** at decane saturation around 0.4. This is the end of the pre-saturation stage. After the core was shut-in at the beginning of Stage 1, counter-current flow occurred. Decane saturation increases at the top, decreases at the bottom and remains the same at the middle (**Figure 4.28a**). Therefore, the top part of the core continues to follow the drainage capillary pressure curve **ODB**, and the lower part follows an imbibition-scanning curve **OEA**. In Stage 1, the capillary pressure stayed on a single capillary pressure curve **BDOEA**, but in Stage 2, the core had a variable saturation profile with the saturation history that depended on the vertical position in the sample. Thus a good match to the experimental data of Stage 1 was obtained with a single

capillary pressure curve. However, a full hysteresis map was needed to match Stage 2 of the experiments.

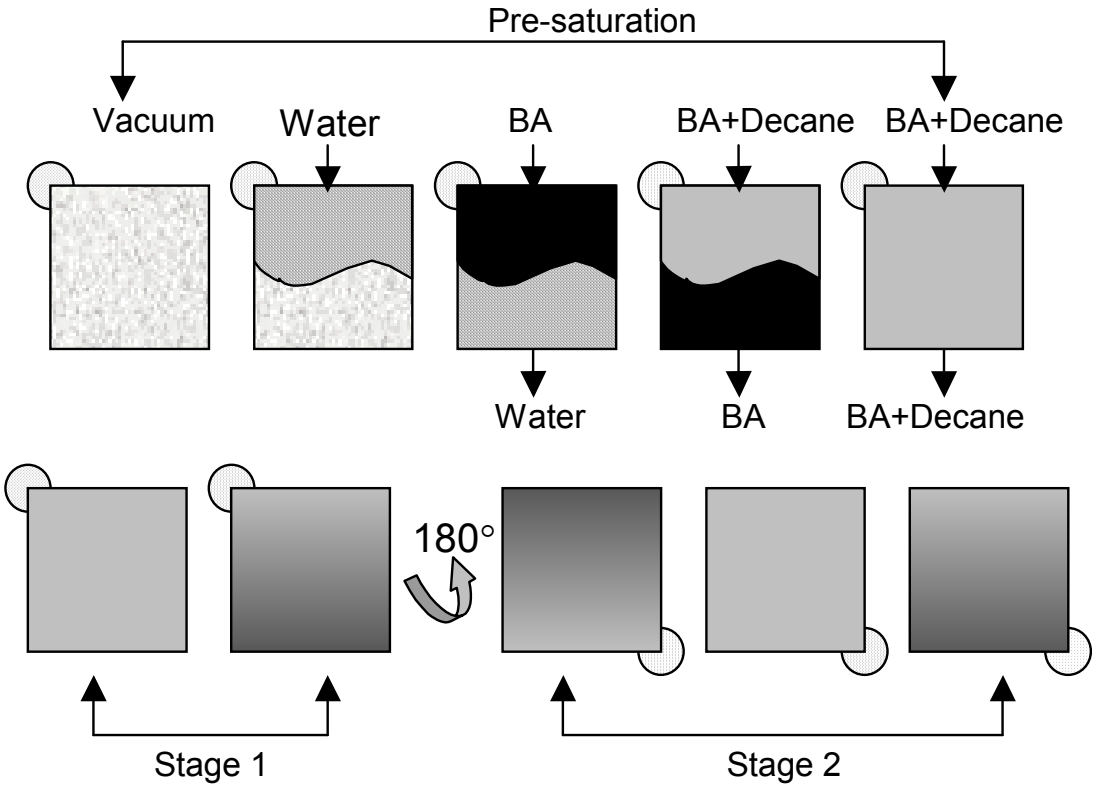

Figure 4.26: Schematic of Karpyn's experimental procedure (from Karpyn 2001).

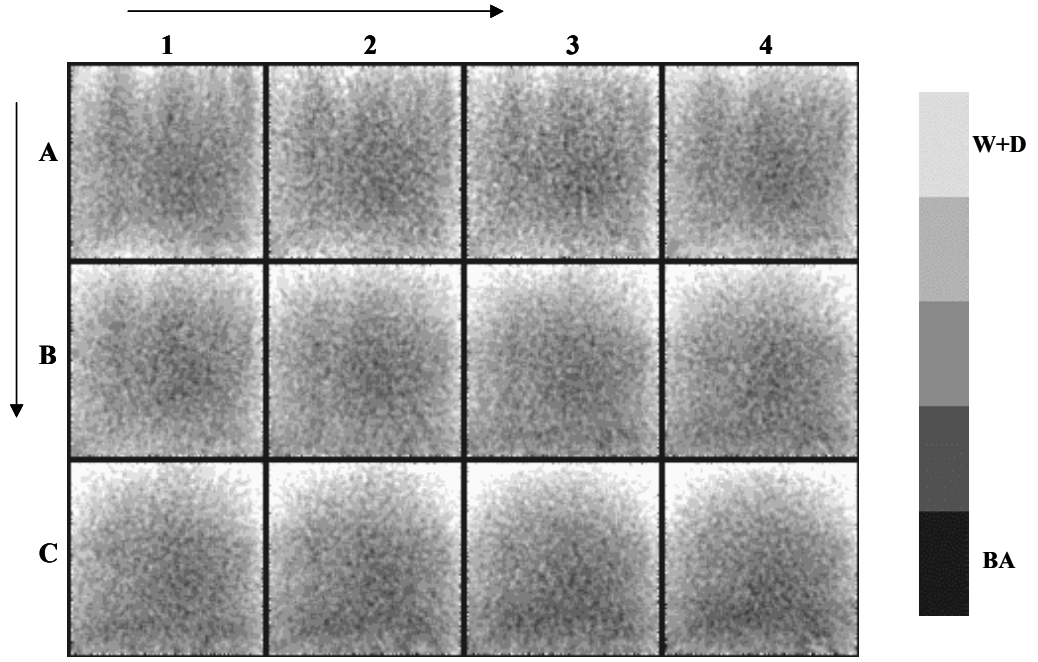

Figure 4.27a: CT images of Stage 1 in Karpyn's experiment (from Karpyn 2001).

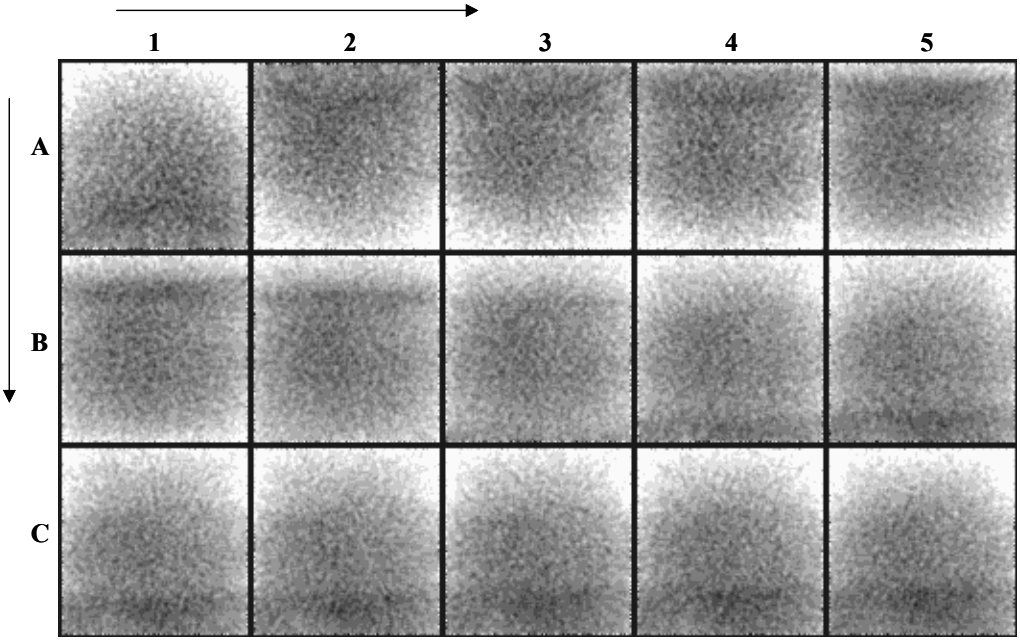

Figure 4.27b: CT images of Stage 2 in Karpyn's experiment (from Karpyn 2001).

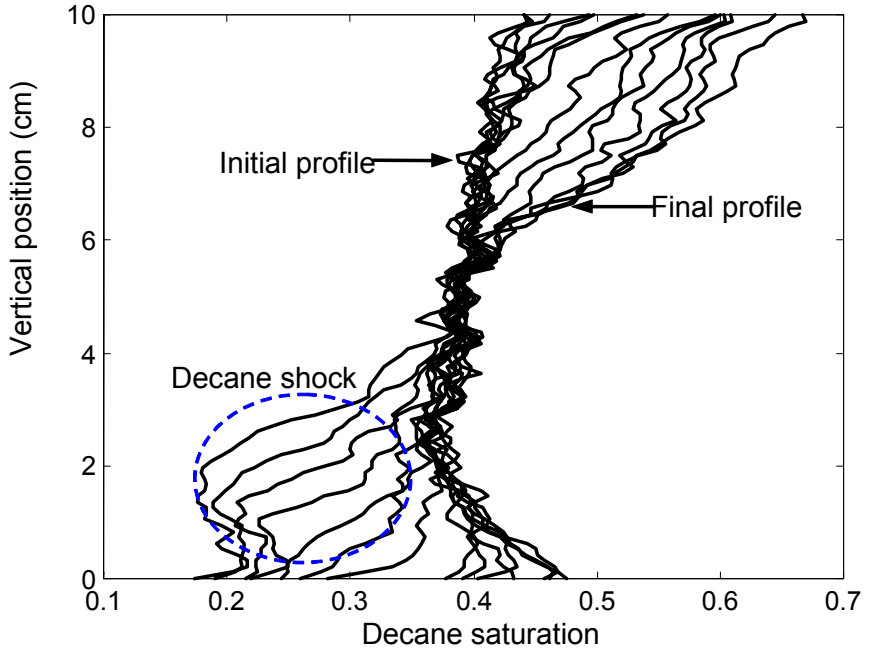

Figure 4.28a: Decane saturation profiles of Stage 1 in Karpyn's experiments.

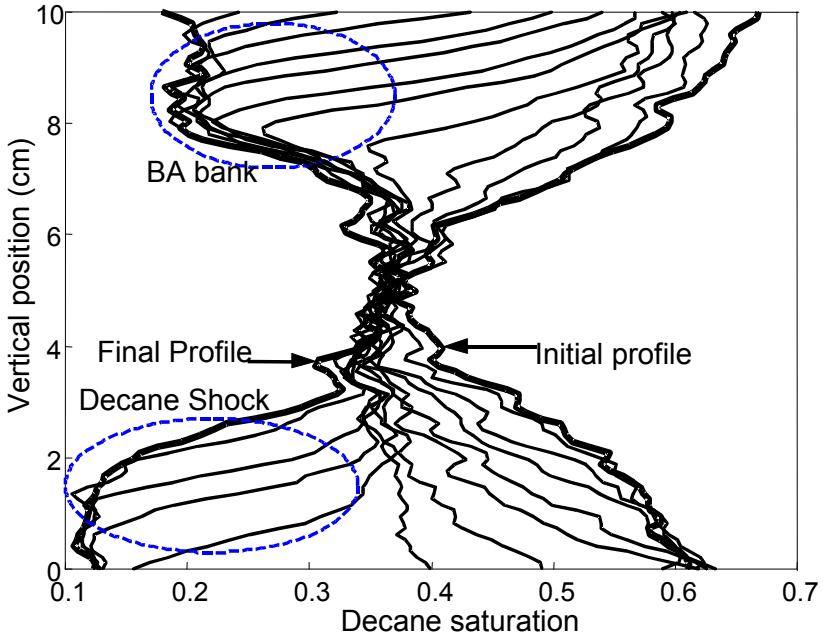

Figure 4.28b: Decane saturation profiles of Stage 2 in Karpyn's experiments.

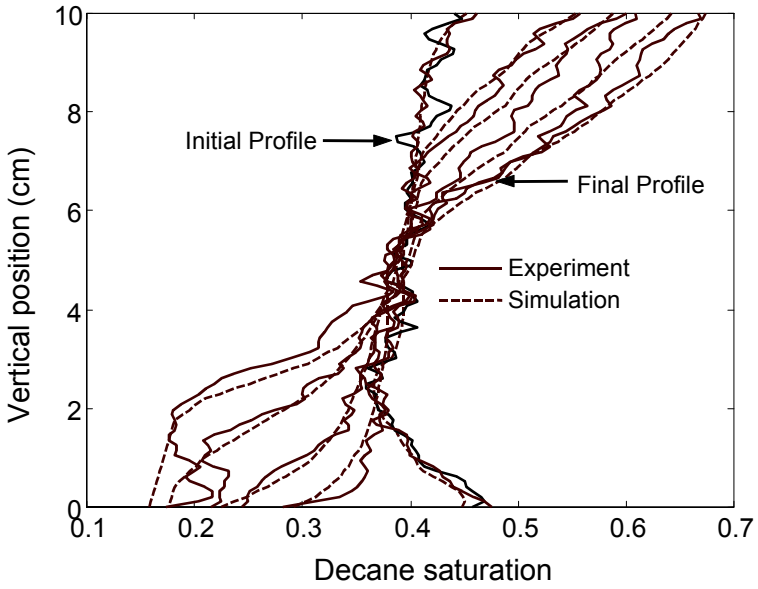

Figure 4.29: Decane saturation profile match for Stage 1 in Karpyn's experiments.

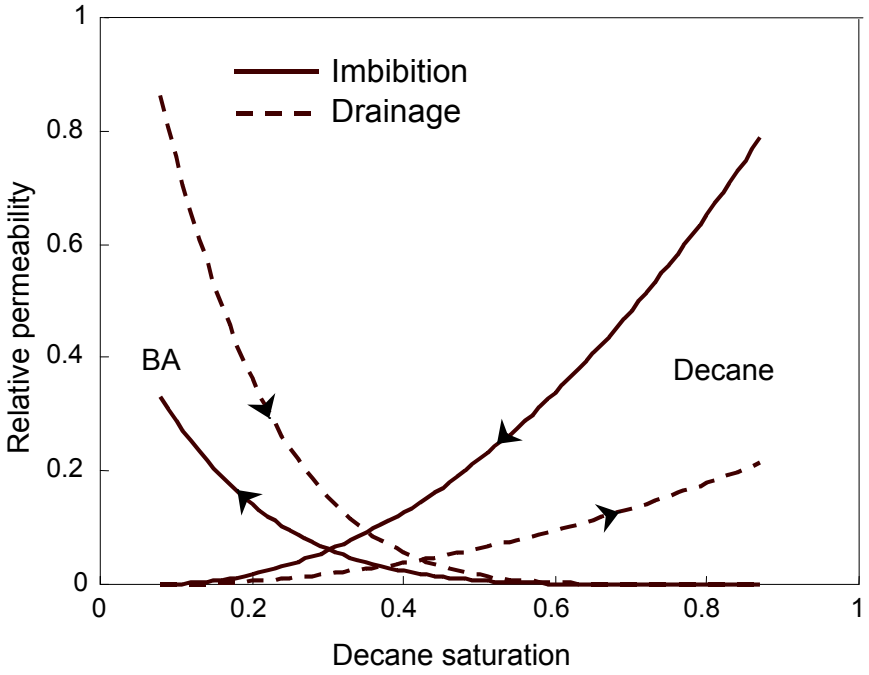

Figure 4.30: Relative permeabilities obtained by matching the Stage 1 in Karpyn's experiments.

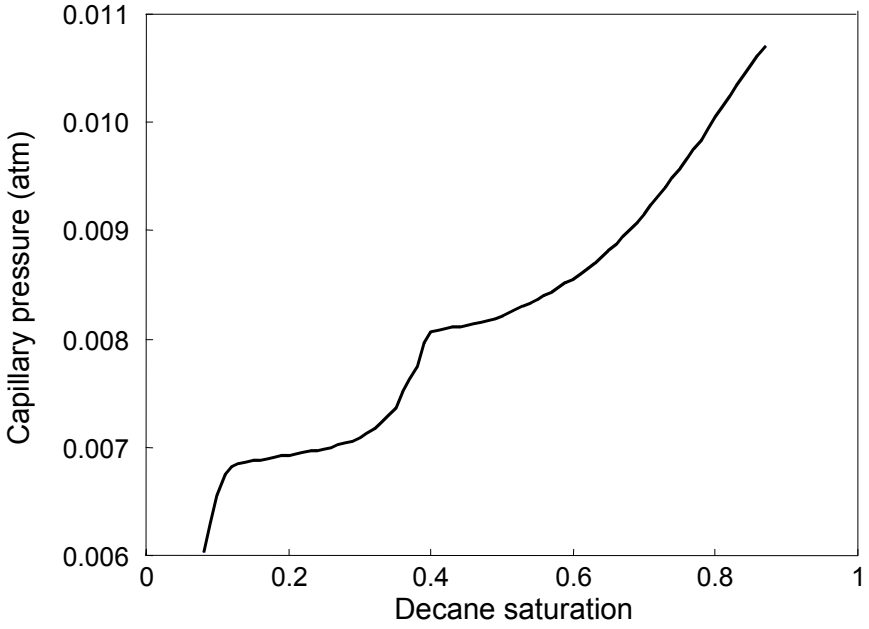

Figure 4.31: Capillary pressure obtained by matching the Stage 1 in Karpyn's experiments.

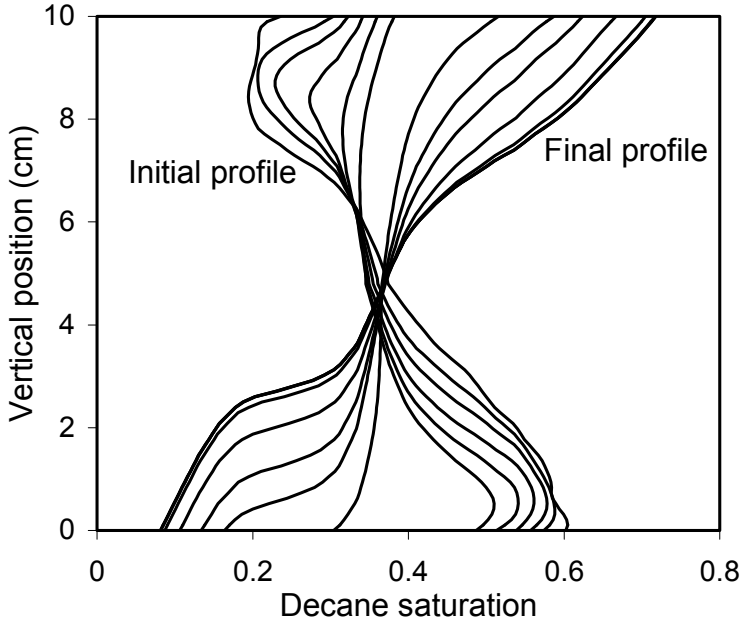

Figure 4.32: Decane saturation profiles simulated with a single pc for Stage 2 in Karpyn's experiments.

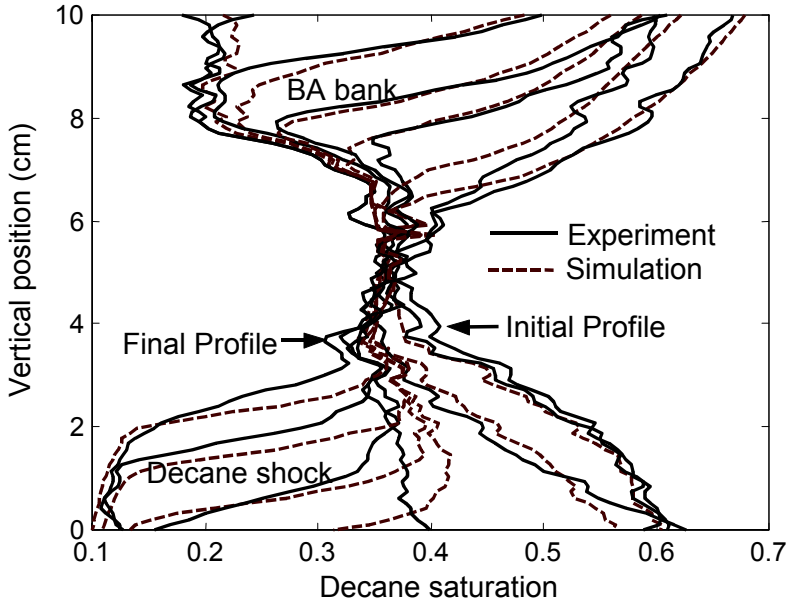

Figure 4.33: Saturation profile match for Stage 2 in Karpyn's experiments.

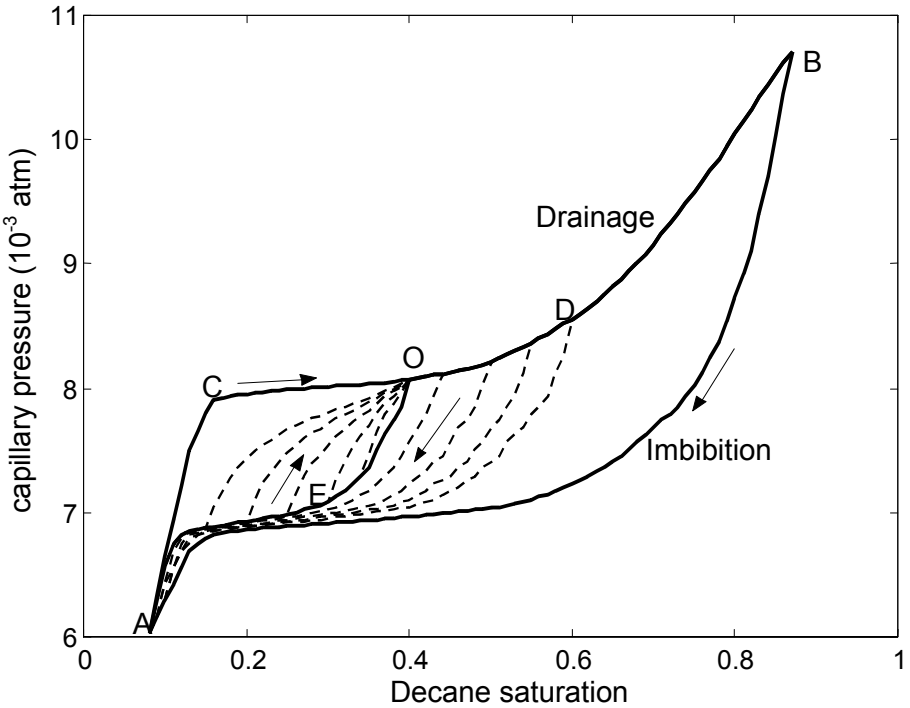

Figure 4.34: Capillary pressure hysteresis loop and scanning curved used in simulating Stage 2 in Karpyn's experiments.

4.5 Modeling of Briggs' Experiments

Several counter-current flow experiments were done by Briggs (1966). Two of them (Experiment 3 and Experiment 4) were chosen for investigation. The core is made of glass beads with 30 inches in height and 2 inches in diameter. Water and air were used in both experiments. The saturations were determined by measuring, at various positions and times, the radioactivity of the liquid phases, which contained an I^{131} tracer. The parameters of the core samples are detailed in the reference (Briggs, 1966). The procedure of the experiments was as follows: vacuum saturate the core with the liquid phase (imbibition) till a certain saturation was obtained. Close the system, and rotate 180°. Then open the top and let it segregate. Then close the system rotate another180° and perform the experiment.

The drainage and imbibition capillary pressure curves shown in **Figure 4.35** were measured for different core samples. The loop represented with a solid line in the graph is the capillary hysteresis loop used in the simulation. Table 4.2 shows the properties of the core sample for different sets of experimental data.

The saturation history modeling method was applied to these two experiments. **Figure 4.36a** shows the match of saturation profiles for Briggs experiments (Experiment 3) with solid line with dots representing the experimental data and dash line representing simulation results. The fluid banks are well captured in the simulation. In **Figure 4.36b**, the simulation from Briggs (solid line) is compared with the ones from history dependent simulation (Experiment 4). In Briggs' simulation, the imbibition capillary curve was used. Their simulation only matches the average behavior and did not reproduce the fluid bank. The history dependent simulation (long-dash line) shows a better match. The

capillary pressure hysteresis loop was provided by the literature (Briggs, 1966), and the scanning curves are constructed by the combination of the Kleppe and Killough methods. The hysteresis loop with the constructed scanning curves is shown in **Figure 4.37**. The average water saturation of Experiment 3 and are Experiment 4 were 0.4 and 0.5, respectively. The only difference between the two experiments is the position of point **O**. The relative permeabilities were obtained from history matching shown in **Figure 4.38**.

Table 4.2: The properties of core samples for capillary pressure measurements (from Briggs 1963).

Data set symbols	Type of process	Permeability (D)	Porosity
×	Drainage	12.52	0.394
□	Drainage	11.78	0.398
*	Imbibition	11.20	0.397
Δ	Imbibition	From reference	

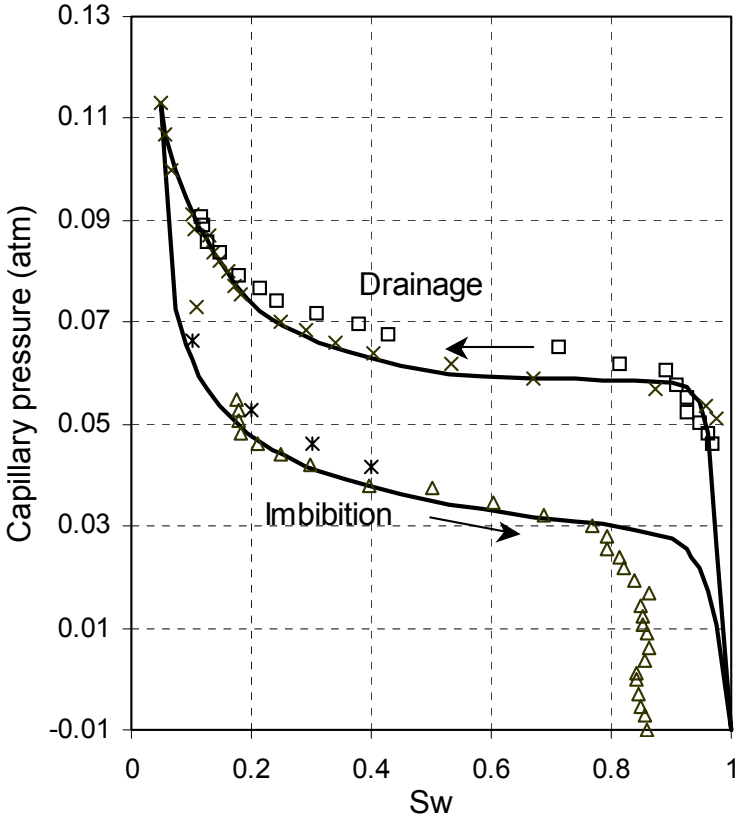

Figure 4.35: The capillary hysteresis loop experimental data and the loop used in simulation (from Briggs, 1963).

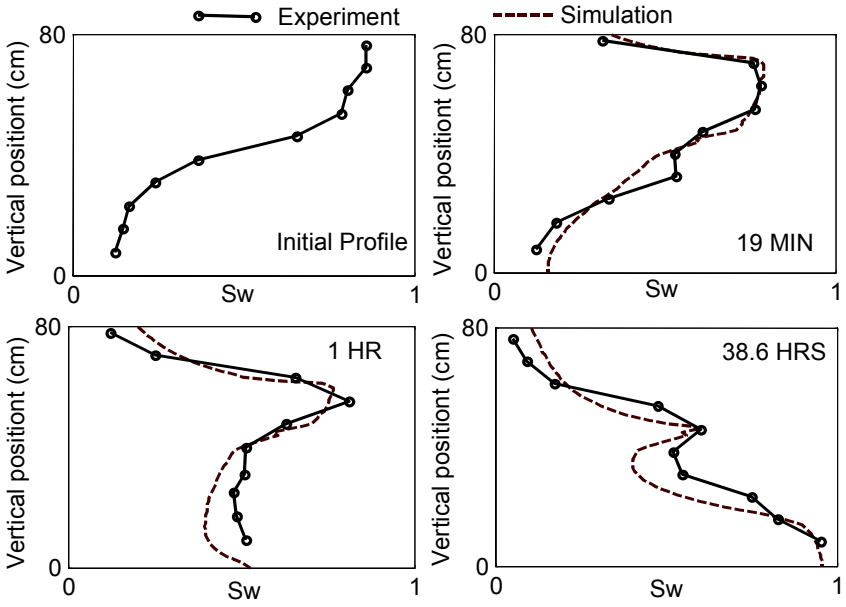

Figure 4.36a: Saturation profile match in Briggs experiment (Experiment 3).

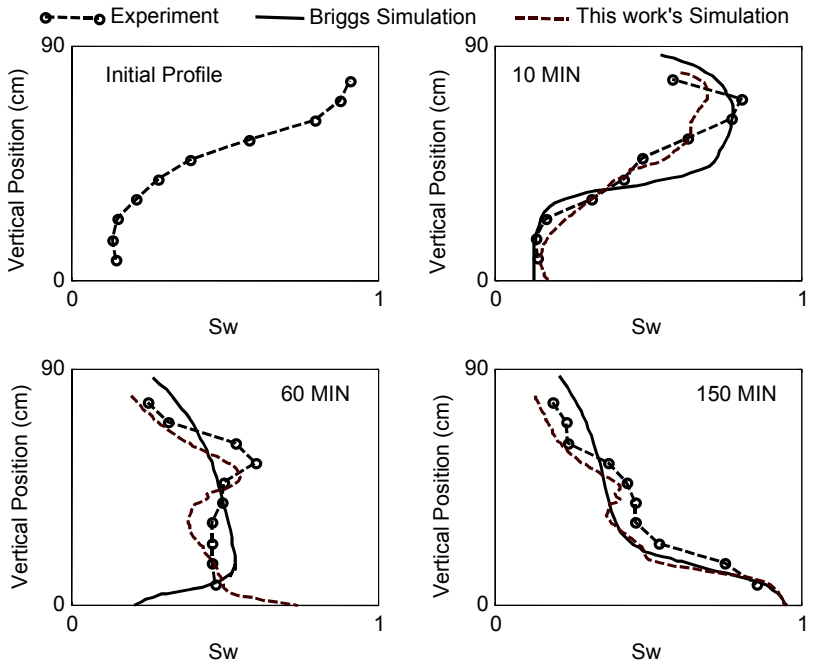

Figure 4.36b: Saturation profile match in Briggs experiment
and comparison with their simulation(Experiment 4).

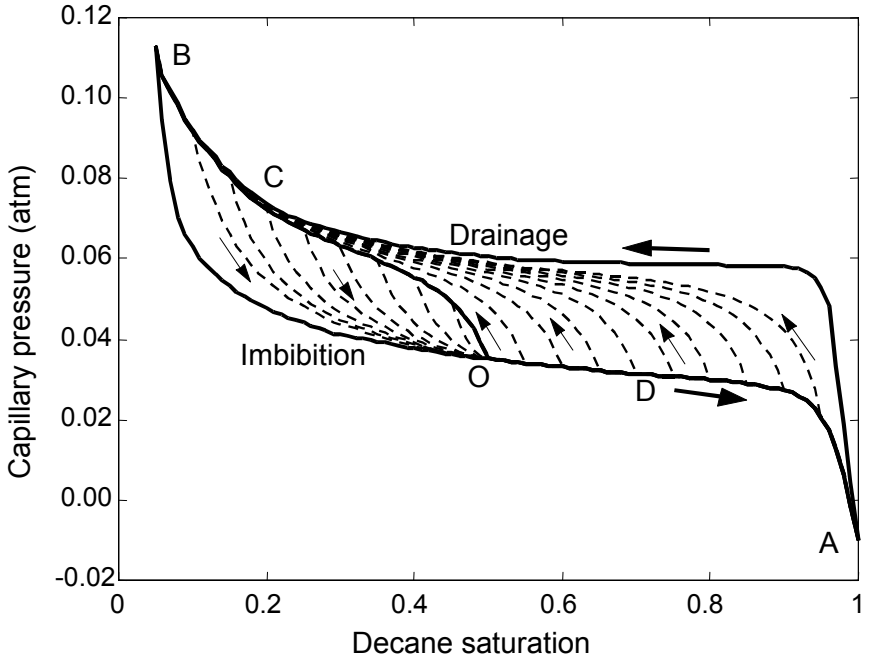

Figure 4.37a: Capillary pressure hysteresis loop with its scanning curves for Briggs experiment (Experiment 3).

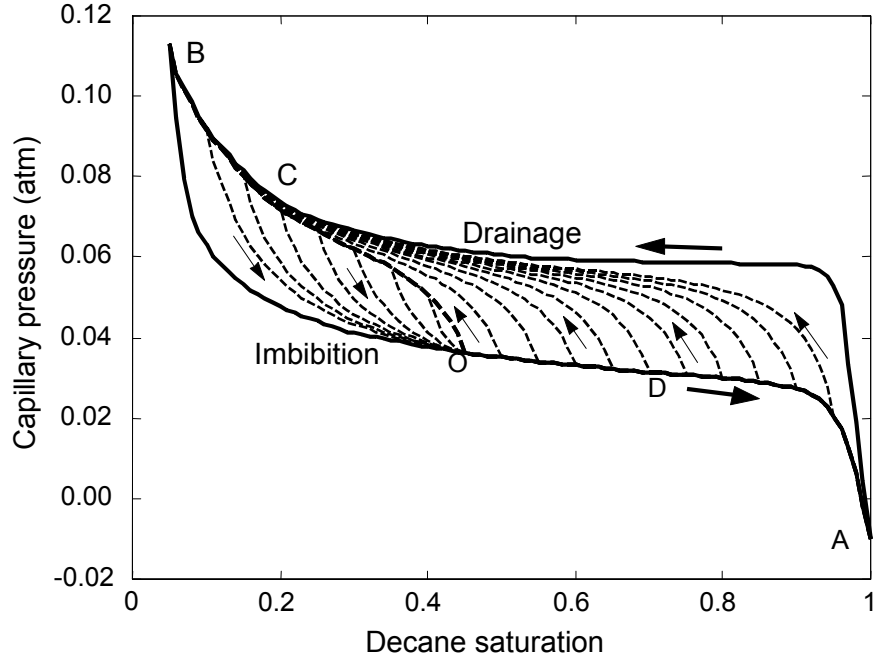

Figure 4.37b: Capillary pressure hysteresis loop with its scanning curves for Briggs experiment (Experiment 4).

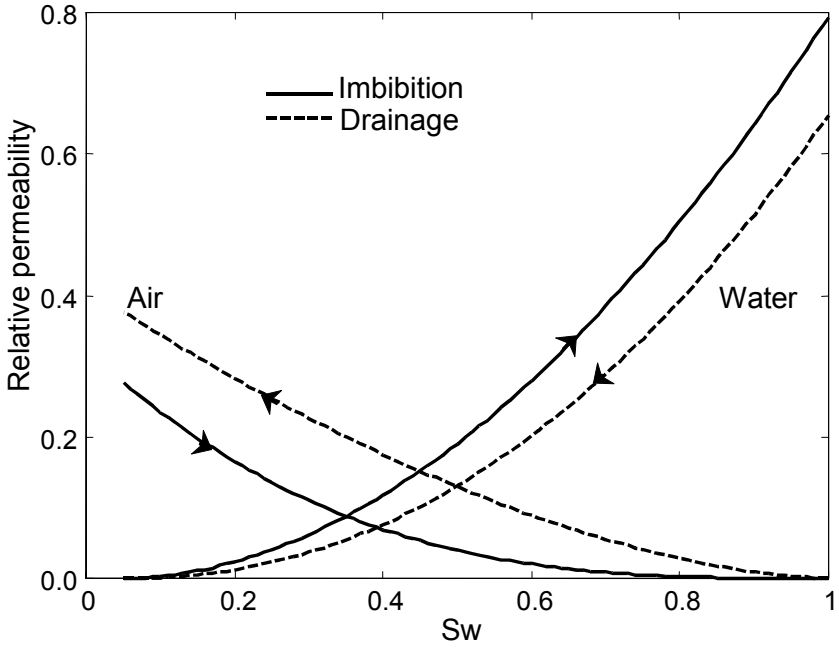

Figure 4.38a: Relative permeabilities for Briggs experiment (Experiment 3).

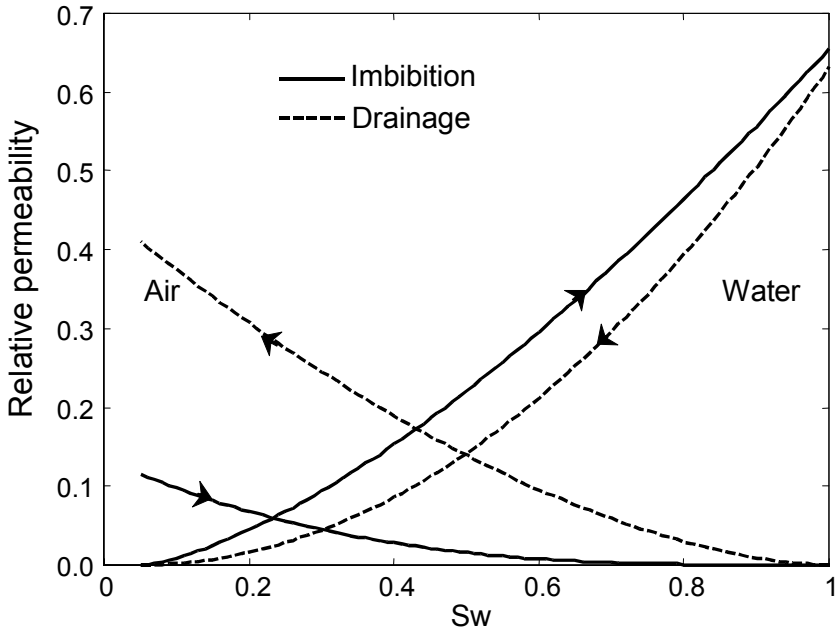

Figure 4.38b: Relative permeabilities for Briggs experiment (Experiment 4).

CHAPTER 5

DISCUSSION AND ANALYSIS

5.1 Total Effective Mobility.

Mobility is defined as the ratio of effective permeability of a fluid to its viscosity. In the following discussion, subscript "w" represents wetting phase and "nw" represents non-wetting phase. The mobility of wetting and non-wetting phases is defined, respectively:

$$\lambda_w = \frac{k_w}{\mu_w} = \frac{k \cdot k_{rw}}{\mu_w} \tag{5.1a}$$

$$\lambda_{nw} = \frac{k_{nw}}{\mu_{nw}} = \frac{k \cdot k_{rnw}}{\mu_{nw}} \tag{5.1b}$$

where k is the absolute permeability; μ is the viscosity; k_r is the relative permeability; and k_w and k_{nw} are the effective permeabilities.

From Darcy's equation in the vertical direction, the flow velocity of a fluid can be calculated by,

$$v_w = -\lambda_w \left(\frac{dp_w}{dz} + \rho_w g \right) \tag{5.2a}$$

$$v_{nw} = -\lambda_{nw} \left(\frac{dp_{nw}}{dz} + \rho_{nw} g \right) \tag{5.2b}$$

Differentiating the definition of capillary pressure $p_c = p_{nw} - p_w$ yields,

$$dp_c = dp_{nw} - dp_w \tag{5.3}$$

In a multiphase flow environment, total velocity of fluids is defined as the sum of the velocity of each phase:

$$v_t = v_w + v_{nw} \tag{5.4}$$

After substituting Equations (5.3) and (5.4) into Equations (5.2), the phase pressure can be eliminated and the following expression of phase velocity can be obtained:

$$v_w = \left(\frac{1}{\lambda_w} + \frac{1}{\lambda_{nw}}\right)^{-1}\left(\frac{v_t}{\lambda_{nw}} + \frac{dp_c}{dz} - (\rho_w - \rho_{nw})g\right) \tag{5.5a}$$

$$v_{nw} = \left(\frac{1}{\lambda_w} + \frac{1}{\lambda_{nw}}\right)^{-1}\left(\frac{v_t}{\lambda_w} - \frac{dp_c}{dz} + (\rho_w - \rho_{nw})g\right) \tag{5.5b}$$

In a closed system, $v_t = 0$, therefore,

$$v_w = -v_{nw} = \left(\frac{1}{\lambda_w} + \frac{1}{\lambda_{nw}}\right)^{-1}\left(\frac{dp_c}{dz} - (\rho_w - \rho_{nw})g\right) \tag{5.6}$$

Total effective mobility is defined as

$$\lambda_{te} = \left(\frac{1}{\lambda_w} + \frac{1}{\lambda_{nw}}\right)^{-1} \tag{5.7}$$

Total effective mobility represents the ability that fluid can flow through the system. This concept is valid for both co-current flow and counter-current flow.

5.2 Co-Current Flow Versus Counter-Current Flow.

Co-current flow is a flow process, in which all fluids flow in the same direction. Most petroleum engineers deal with this type of fluid flow. But in some cases, different fluids flow at opposite directions, which is called counter-current flow. In the early study of counter-current flow, many investigators proposed that the relative permeabilities of counter-current flow are different than that of co-current flow. Al-Wadahi et al. (2000) found that counter-current flow relative permeabilities are smaller than that of co-current in the same system. **Figure 5.1a** shows the relative permeabilities obtained from the 34-inch position of Barbu's Experiment A. The co-current relative permeabilities from a similar system are also presented in this graph. The counter-current relative permeabilities (short dash lines) obtained by Al-Wadahi et al. (2000) using neuro-simulation are noticeably smaller than that of co-current flow (solid line). This is also true for the relative permeabilities obtained from single pc simulation of this work. The counter-current flow relative permeabilities from these two methods are very close to each other. In these two methods, the same parameter representation was used. The relative permeabilities are represented in a power law form as in Equation (3.18), and the capillary pressure is represented as a similar curve to the final saturation profile. But these parameters were obtained with different methods. Al-Wadahi et al. (2000) used neuro-simulation and automatic history matching is used in this research.

In saturation history dependent simulation, two pairs of relative permeability curves were used for the two processes that occurred in the system: drainage and imbibition. The counter-current relative permeabilities obtained with this method are smaller than the co-current flow relative permeabilities except the decane imbibition

relative permeability (**Figure 5.1a**). This is also true in Karpyn's experiments, the relative permeabilities of which are shown in **Figure 5.b**. But the total effective mobility of the counter-current flow is always smaller than that of the co-current flow, which is shown in **Figure 5.2a** and **5.2b** for Barbu's and Karpyn's experiments, respectively.

Kalaydjian (1990) also concluded that counter-current flow relative permeabilities are smaller than that of co-current flow and he attributed this relative permeability reduction to viscous coupling. The effect of hysteresis of the process has not been considered. In the derivation of total effective mobility, in a closed system, the flow velocity is controlled by the total effective mobility, not relative permeabilities. The total effective mobility is mainly controlled by the less mobile phase, which is consistent with observations by Pirson (1958). When the mobility of two phases is not very different, they both control the process.

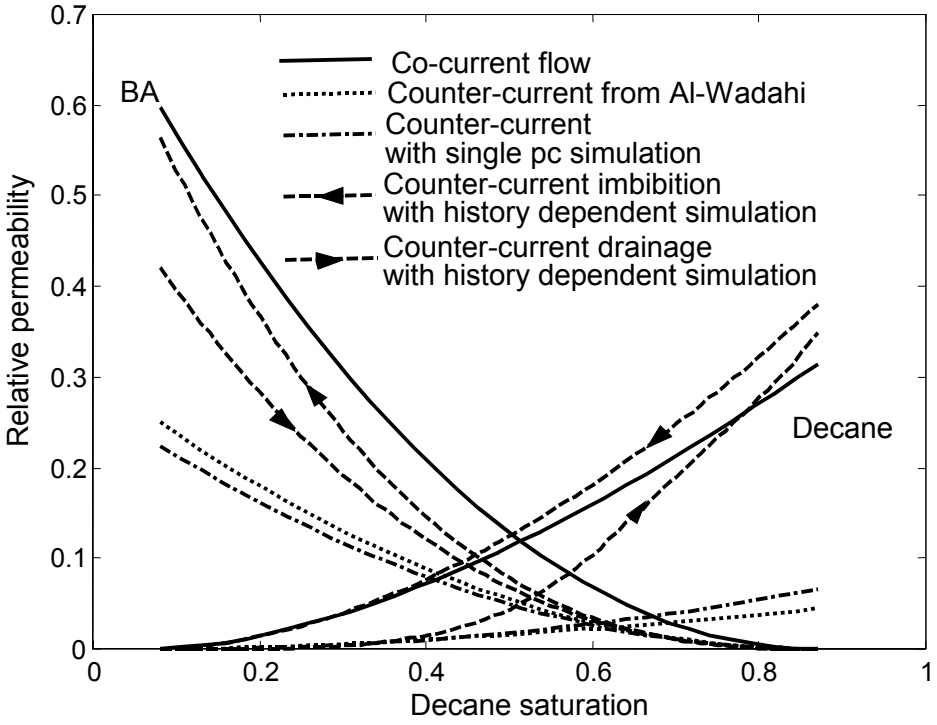

Figure 5.1a: Relative permeabilities of Stage 2 at 34-inch position in Barbu's Experiment A.

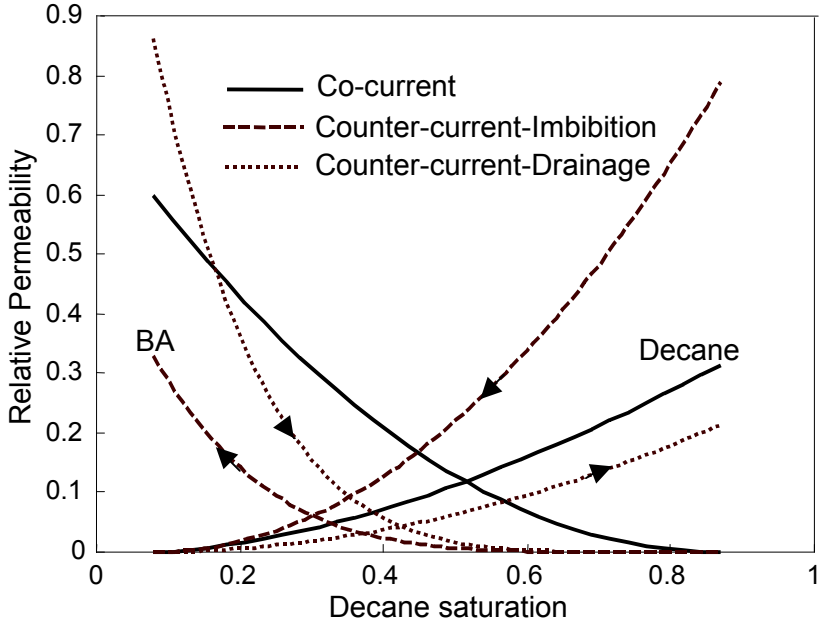

Figure 5.1b: Relative permeability curves used in history dependent simulation of Karpyn's experiment.

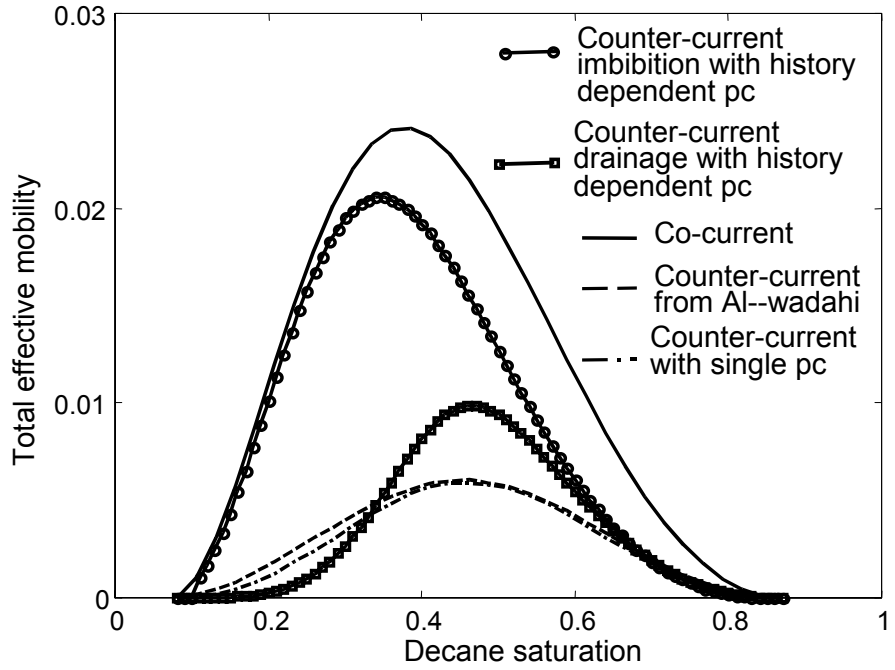

Figure 5.2a: Total effective mobility of Stage 2 at 34-inch position in Barbu's Experiment A.

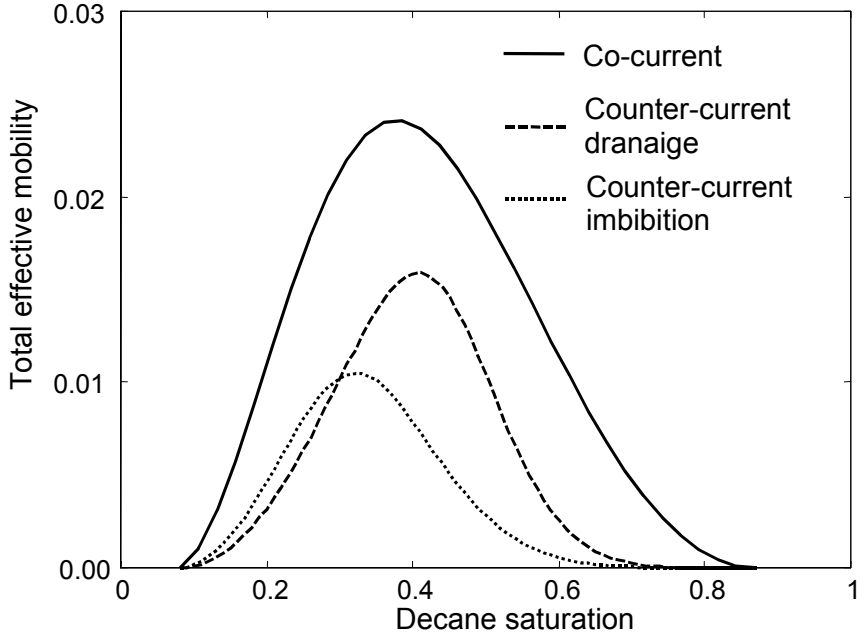

Figure 5.2b: Total effective mobility curves of Karpyn's experiment.

5.3 History Dependent Modeling.

Counter-current flow can be modeled with a single capillary pressure curve and one pair of relative permeability curves only if fluid banks do not form. When fluid banks form, saturation history dependent modeling method must be implemented and this method can also be applied to model the process without banks. Therefore, the single pc method can be considered as a subset of the history dependent modeling method. **Figure 5.3** shows the capillary pressure hysteresis loop used in the saturation history dependent modeling and the capillary pressure curve used in the single pc modeling for Barbu's Experiment A. At low and high decane saturations, the capillary pressure curve in single pc method overlaps on the hysteresis loop and there is a transition zone in the middle. The curve in the transition zone is a combination of drainage and imbibition-scanning curves, which is only an average effect. This effect is also shown in the relative permeabilities shown in **Figure 5.1**.

In history dependent simulation, the hysteresis of the flow process was considered, thus two pairs of relative permeability curves were introduced with one pair for the drainage process and another pair for the imbibition process. Both pairs of relative permeability curves are larger than the ones obtained with the single pc method. In the single pc method, only one pair of relative permeability curves is used. This is an average of the history dependent simulation method. Based on the derivation of total effective mobility, the total relative permeability is the harmonic average of the two pairs (drainage and imbibition), in which case, the average is always less than either of them.

Briggs (1966) simulated their counter-current flow process using the measured imbibition capillary pressure curve. Their simulation only matches the general behavior of the process and the fluid banks are not clear the simulation (**Figure4.36b**). The solid lines represent their simulation results. The saturation history modeling method was also applied to the same experiments. It is noticeable that the history dependent simulation (long-dash line) shows a better match and it satisfactorily captures the fluid bank behavior.

The reason why history dependent modeling yields better matches than other methods is that it includes hysteresis. Different regions use the corresponding relative permeabilities and capillary pressure according to the process it undergoes (drainage or imbibition). Because different regions in the system follow different capillary pressure curves according to the saturation and saturation history, the capillary pressure curve dynamically changes with time. The dynamic capillary pressure curves at each time step in the hysteresis loop together with the saturation profiles, capillary pressure profiles, and mobility profiles are shown in **Figures 5.4a-n** for Stage 2 in Karpyn's experiments. In each figure there are three profiles: saturation profiles at the top left (a); total effective mobility profiles at the top right (b), and capillary pressure profiles at the bottom left (c). The dynamic capillary pressure curve with the hysteresis loop is at the bottom right (d). The capillary pressure profiles are similar to the decane saturation profiles. The middle part of the sample always has the highest mobility. At the beginning and end of the process, mobility has its lowest value at the top and the bottom of the sample, because both reach the residual fluid saturation. In history dependent simulation, the capillary pressure dynamically changes with saturation. The bottom left (d) of **Figures 5.4** show

the snapshot of these capillary pressure curves. At the initial condition, all the capillary pressure points at the upper part are located on the drainage capillary pressure curve but the capillary points in the lower part are located on an imbibition-scanning curve shown in **Figure 5.4a** (bottom right). This is just the capillary pressure curve used in Stage 1. To better understand how these dynamic capillary pressure curves are formed, **Figures 5.5a-e** show the capillary pressure trajectories. These trajectories are the capillary pressure scanning curves that the saturation points follow in the process. The fronts of these trajectories are the dynamic capillary pressure curves. Left parts of the thick dashed line are the trajectories for the drainage process in the top section of the core and the right parts are for the imbibition process at the bottom section of the core. Therefore, the left part moves upward in the capillary hysteresis loop and the right part moves downward in the loop and the middle part hardly changes. At t=0.2 hours (**Figures 5.5a**), trajectory **a** is a fastest path. This is because the drainage-scanning curves at low decane saturation have the largest capillary pressure gradient. The small change of the saturation at the top saturation profile (circle in the top left of **Figure 5.4b**) resulted in the large change in capillary pressure. The saturation change above and below the middle point (where initial and final saturation profiles intersect) of the saturation profile resulted in the upward movement of drainage trajectories **b**, **c**, **d** (**Figure 5.5a**) and the downward movement of imbibition trajectories **e**, **f**. The other two trajectories **g**, **h** have not started moving in the imbibition region, for there is no saturation change at the bottom of the core at t=0.2 hours. The very bottom of the core has near residual benzyl alcohol saturation and very low mobility (the top right of **Figure 5.4b**). At t=0.6 hours, imbibition trajectory **g** started moving downward but imbibition trajectory **h** has not showed up (**Figure 5.5b**). The

other trajectories continued moving along their paths. Drainage trajectory **a** moved further up, which corresponds to the formation of the bank at the top of the core (circle at the top left of **Figure 5.4c**). The formation of the fluid bank is explored further later in this work. Drainage trajectory **a** moved on the drainage capillary pressure curve where trajectory **a** started at t=1.0 hour (**Figure 5.5c**). The continuous smooth connection between the drainage-scanning curve and the drainage capillary pressure curve allows the continuous saturation change in the upper wing of the fluid bank at the top of the core (the top left of **Figure 5.4d**). With a single S-shaped capillary pressure curve, the large gradient in the middle part of the capillary pressure does not allow this continuous saturation changes, which will be discussed later. Starting from t=1.5 hours (**Figure 5.4e**), there appeared a peak in the total effective mobility profiles at the top of the core (top right of the **Figure 5.4e**). This peak corresponds to the crest of the drainage total effective mobility (**Figure 5.2b**). **Figure 5.5d** shows that trajectories at t=4.0 hours. All the imbibition trajectories converge and approach the initial capillary pressure curve. The drainage trajectories converge to the drainage capillary pressure curve and formed an oval shape. The final dynamic capillary pressure curve with all the trajectories are shown in **Figure 5.5e**. This final dynamic capillary pressure curve approaches the initial one, which can also be seen when comparing the dynamic capillary pressure curves at initial condition (the lower right of **Figure 5.4a**) and the final condition t=89.0 hours (**Figure 5.4n**). The dynamic capillary pressure curves shown in **Figures 5.5** are put together in **Figure 5.6**, demonstrating how these capillary pressure curves migrate within the capillary hysteresis loop. The drainage part on the left migrates upward and the imbibition part on the right migrates downward. The final and initial conditions overlap.

The characteristic that the final saturation profile and capillary pressure of the system comes back to the initial condition will result in the same flow process as in Stage 2 after another 180° rotation. The return to the original saturation and capillary pressure occurs in homogeneous systems similar to what was used experimentally. However, in heterogeneous systems, we do not expect to return to the same saturation condition, since capillary pressure and gravity create different saturation.

Between initial condition (**Figure 5.4a**) and t=2.0 hours (**Figure 5.4f**), benzyl alcohol accumulated below the middle point of the core without saturation change at the very bottom. With this increasing benzyl alcohol saturation, the negative capillary pressure gradient at the bottom of the core increased, which assisted the benzyl alcohol to move out and decane moved in at t=3.0 hours (**Figure 5.4g**). At t=6.0 hours, the dynamic capillary pressure curve became flat at the low decane saturation (bottom right of **Figure 5.4i**). The capillary pressure gradient became small in the lower part of the core and it shows an almost vertical straight line in this region of the capillary pressure profile (bottom left of **Figure 5.4i**). The low capillary pressure gradient of this saturation range remains small in the rest of the process (**Figures 5.4j-n**) and this low capillary pressure gradient initiated the build up of the decane shock at the bottom of the core (circles at the top left of **Figures 5.4i-n**). The decane shock developed at the bottom of the core (circle at the top left of **Figure 5.4n**).

The history dependent modeling method is able to capture the physical processes that occur during counter-current flow. The single pc method is not able to simulate the formation of fluid banks. Both methods were used to model the 34-inch position in Barbu's Experiment A and the match of the average saturation profiles from both

methods is quite good. But with the single pc method, the simulation only matches the average saturation profiles. The images from the single pc method are quite different than the experimental ones shown in **Figure 5.7**. The images in the first row are from the experiments and the third row shows the images from the single pc simulation. The single pc simulation exhibits strong artifacts caused by the shape of the sample. Also the single pc method averages out any saturation heterogeneity and creates artificially smooth images. The images generated by the hysteresis dependent method match well with the experimental results (middle row of images).

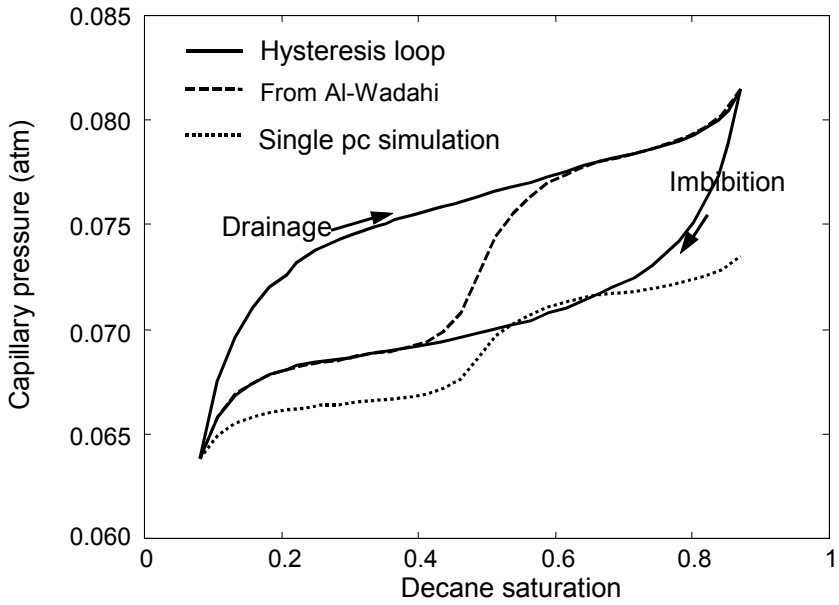

Figure 5.3: Capillary pressure curves of Stage 2 at 34-inch position in Barbu's Experiment A.

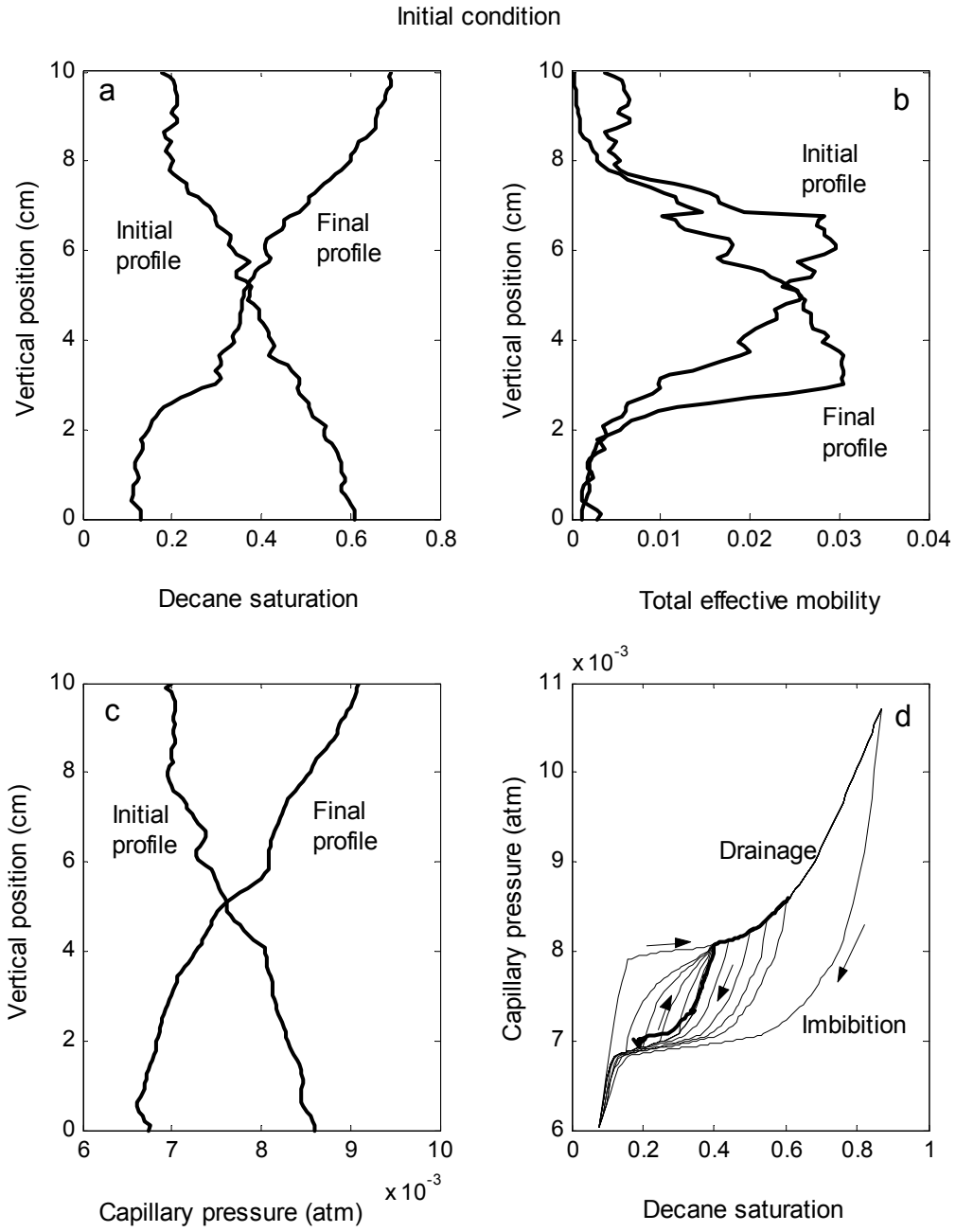

Figure 5.4a: History dependent simulation at initial conditions (Karpyn's experiment): a. saturation profiles; b. total effective mobility profiles; c. capillary pressure profiles; d. dynamic capillary pressure curve on the capillary hysteresis loop and scanning curves.

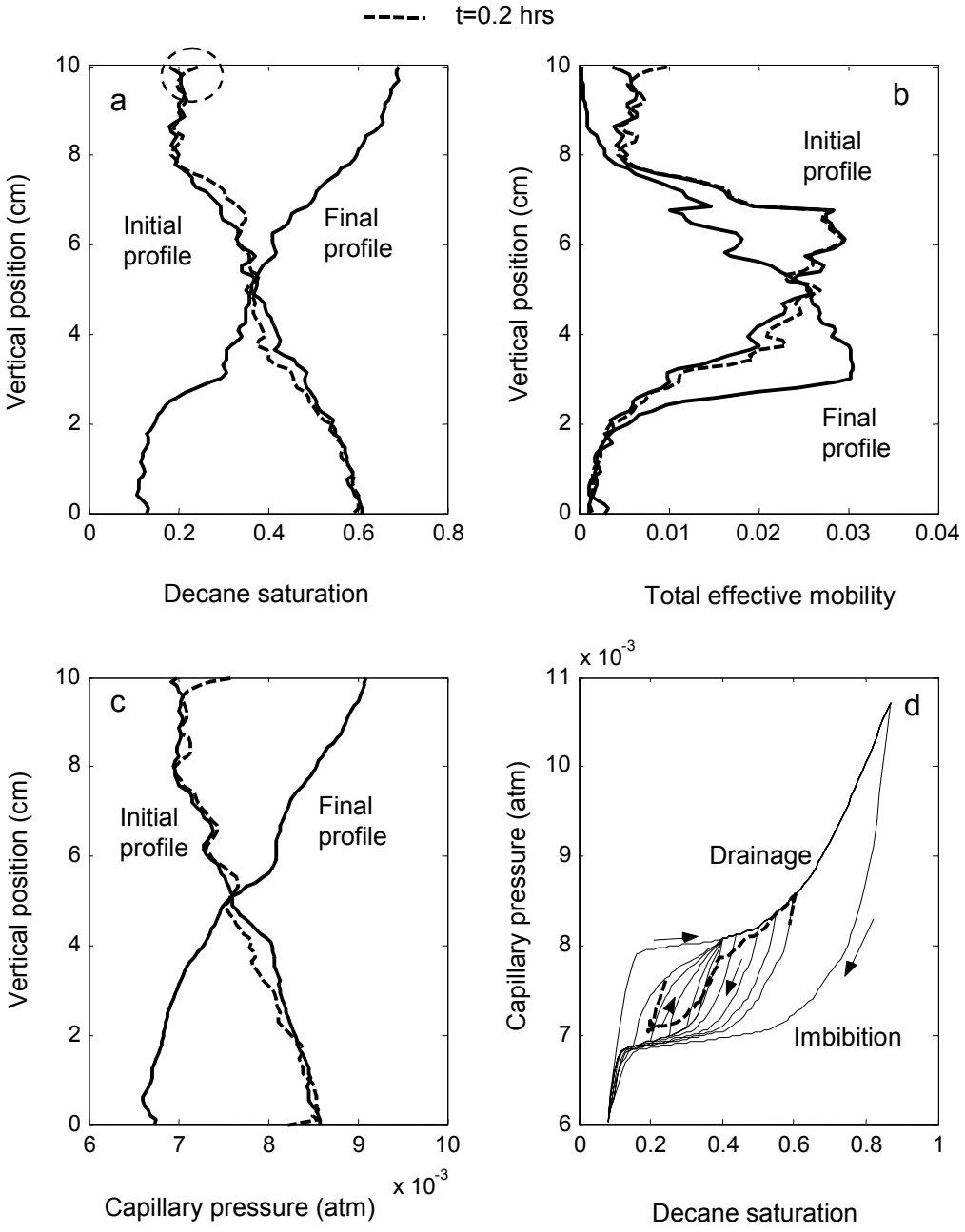

Figure 5.4b: History dependent simulation at t=0.2 hrs (Karpyn's experiment):
a. saturation profiles; b. total effective mobility profiles; c. capillary pressure profiles; d. dynamic capillary pressure curve on the capillary hysteresis loop and scanning curves.

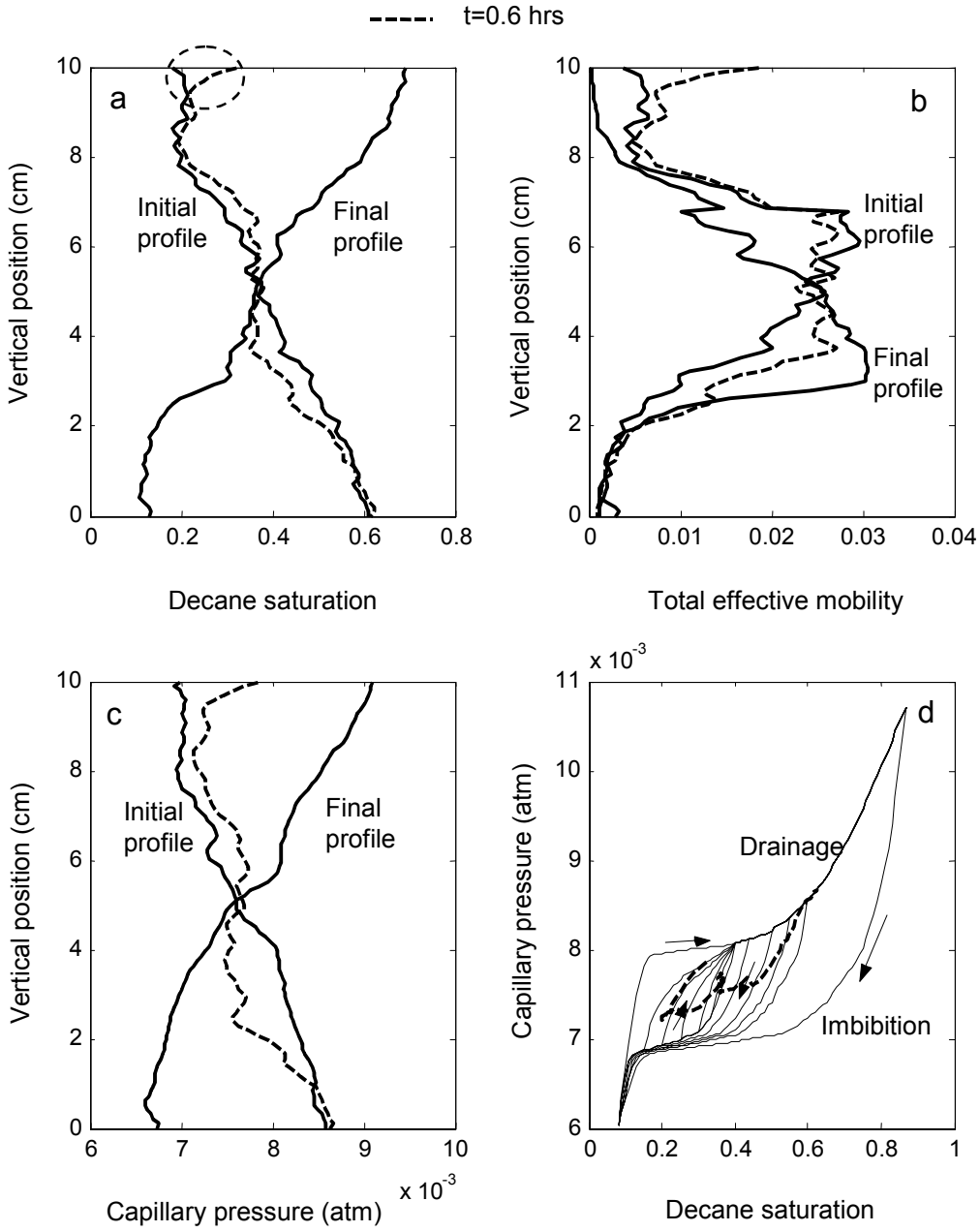

Figure 5.4c: History dependent simulation at t=0.6 hrs (Karpyn's experiment):
a. saturation profiles; b. total effective mobility profiles; c. capillary pressure profiles; d. dynamic capillary pressure curve on the capillary hysteresis loop and scanning curves.

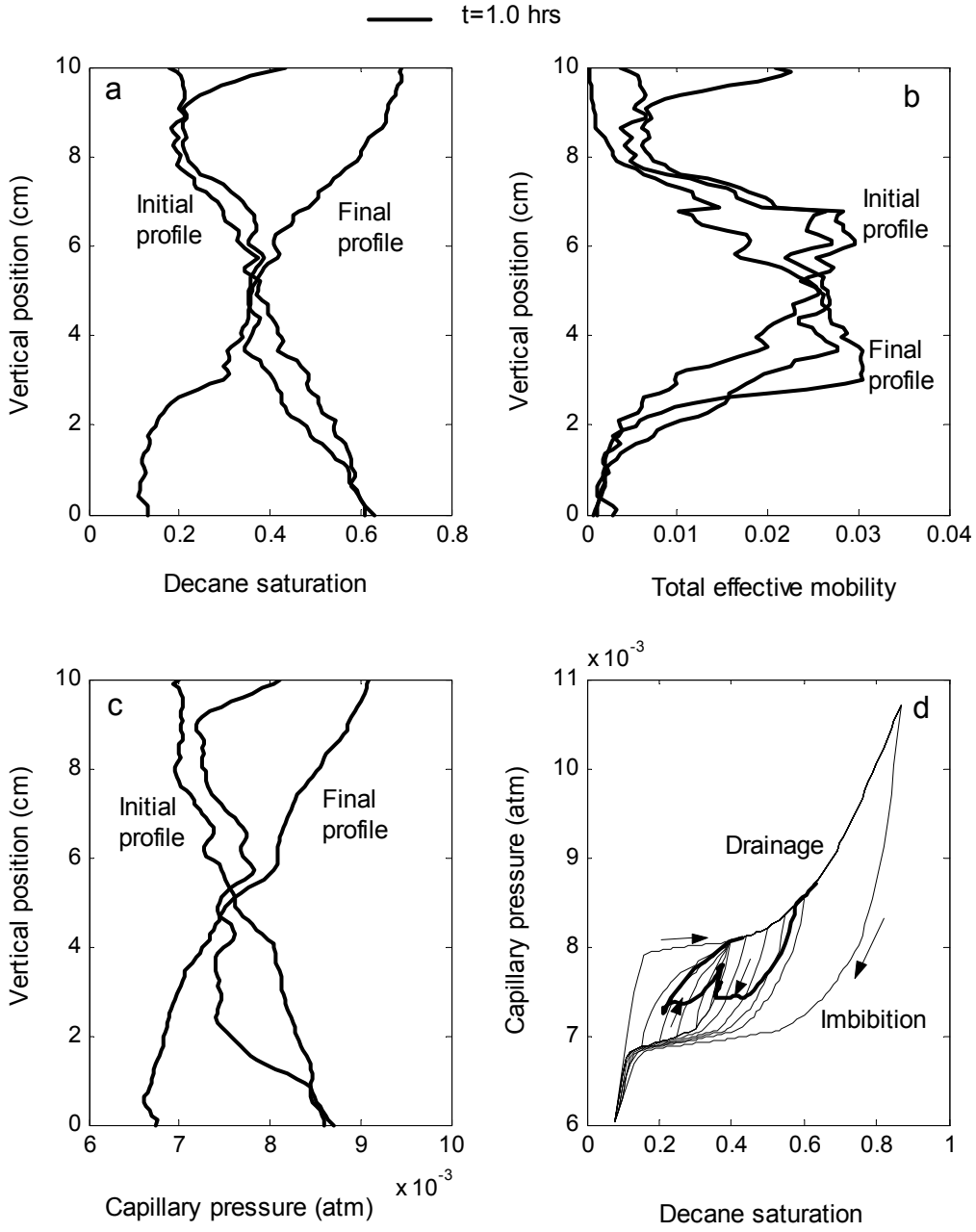

Figure 5.4d: History dependent simulation at t=1.0 hrs (Karpyn's experiment):
a. saturation profiles; b. total effective mobility profiles; c. capillary pressure profiles; d. dynamic capillary pressure curve on the capillary hysteresis loop and scanning curves.

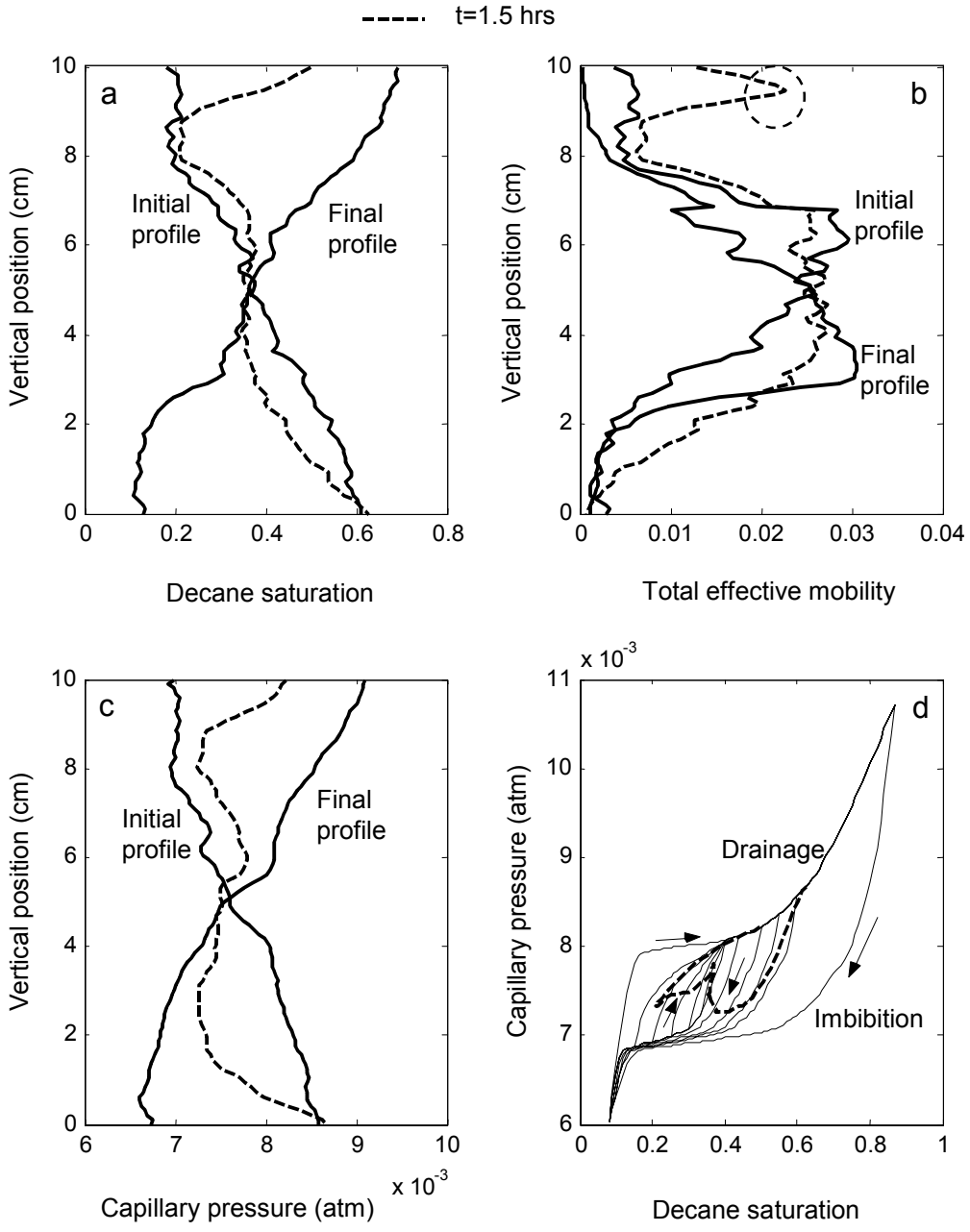

Figure 5.4e: History dependent simulation at t=1.5 hrs (Karpyn's experiment):
a. saturation profiles; b. total effective mobility profiles; c. capillary pressure profiles; d. dynamic capillary pressure curve on the capillary hysteresis loop and scanning curves.

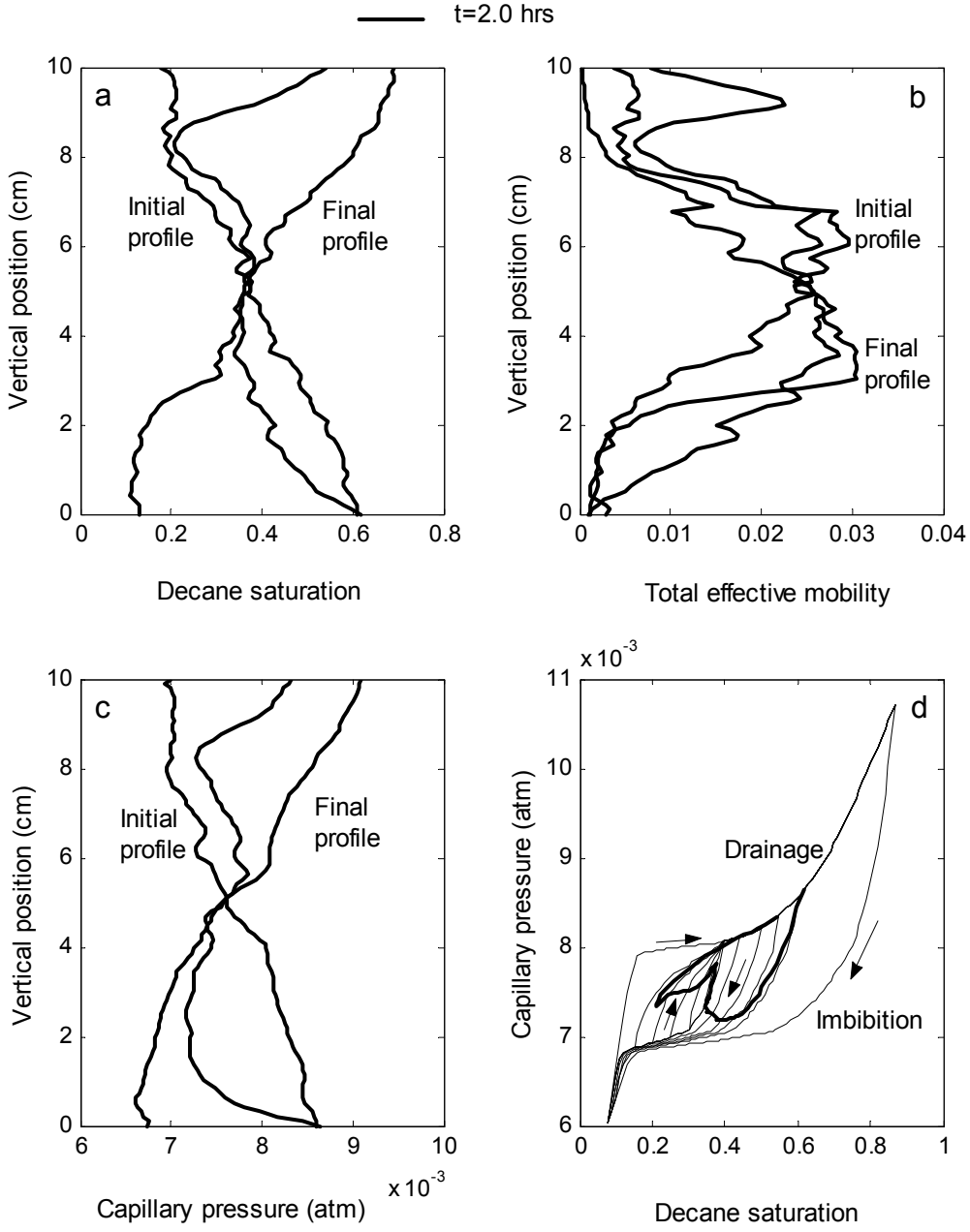

Figure 5.4f: History dependent simulation at t=2.0 hrs (Karpyn's experiment):
a. saturation profiles; b. total effective mobility profiles; c. capillary pressure profiles; d. dynamic capillary pressure curve on the capillary hysteresis loop and scanning curves.

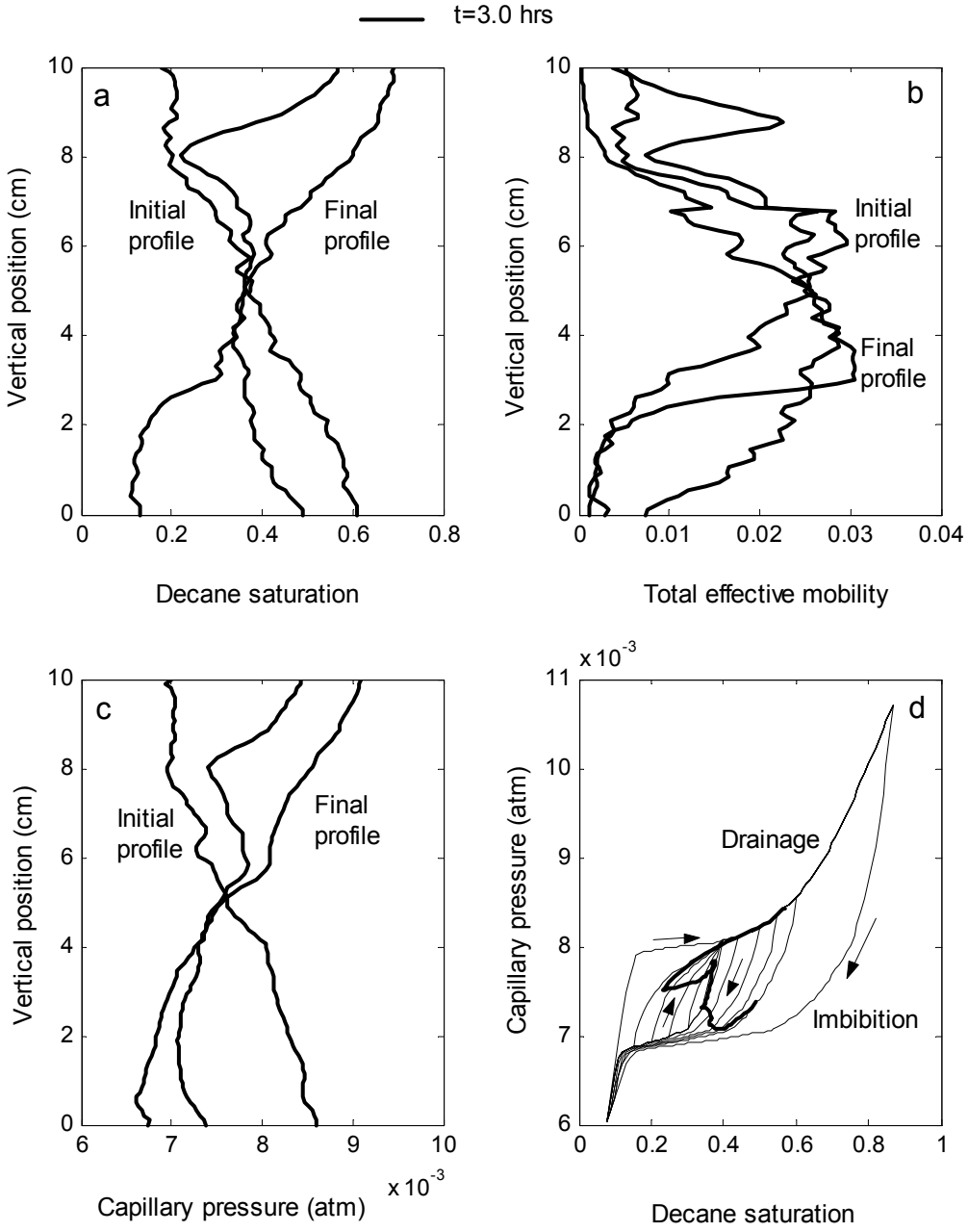

Figure 5.4g: History dependent simulation at t=3.0 hrs (Karpyn's experiment):
a. saturation profiles; b. total effective mobility profiles; c. capillary pressure profiles; d. dynamic capillary pressure curve on the capillary hysteresis loop and scanning curves.

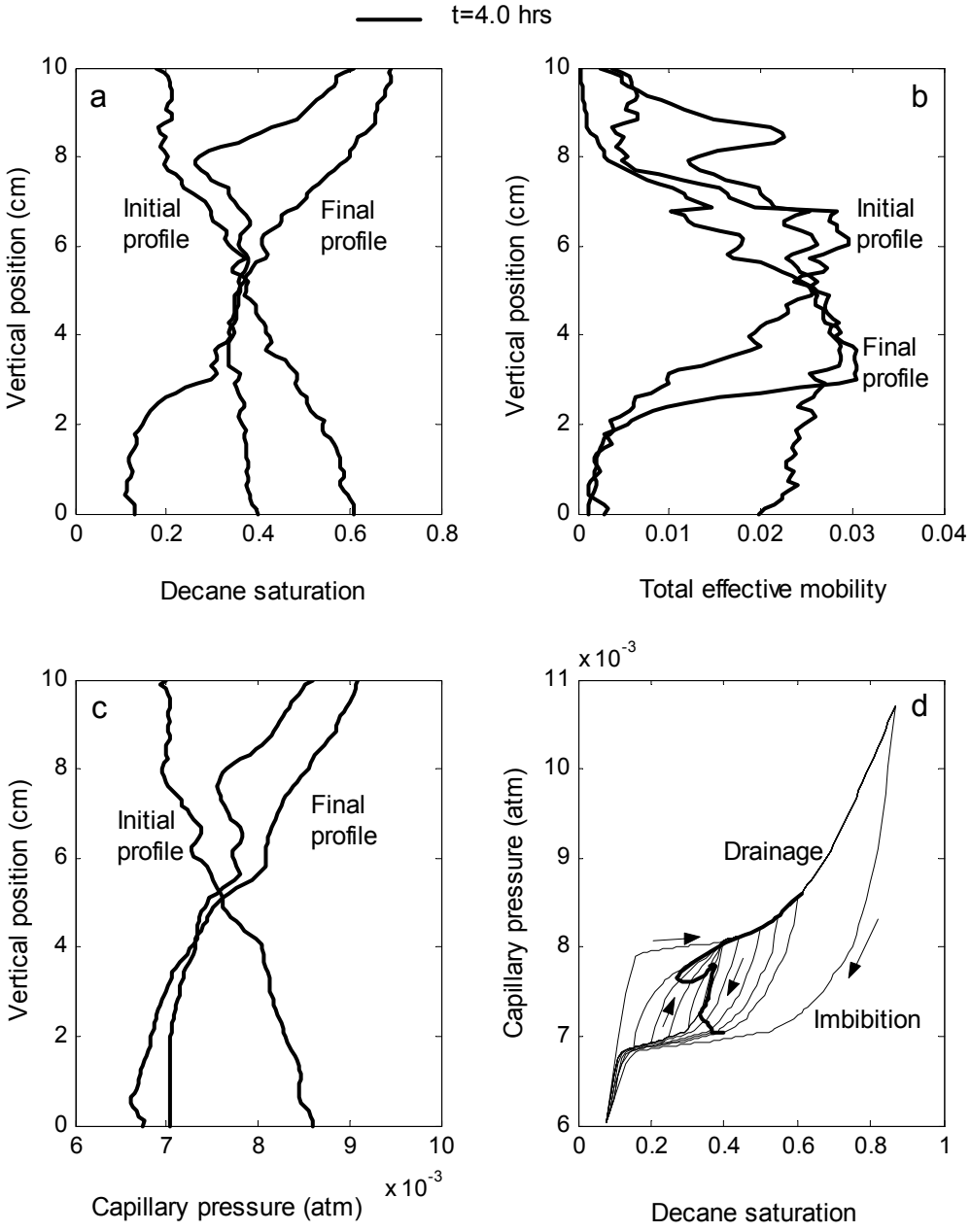

Figure 5.4h: History dependent simulation at t=4.0 hrs (Karpyn's experiment):
a. saturation profiles; b. total effective mobility profiles; c. capillary pressure profiles; d. dynamic capillary pressure curve on the capillary hysteresis loop and scanning curves.

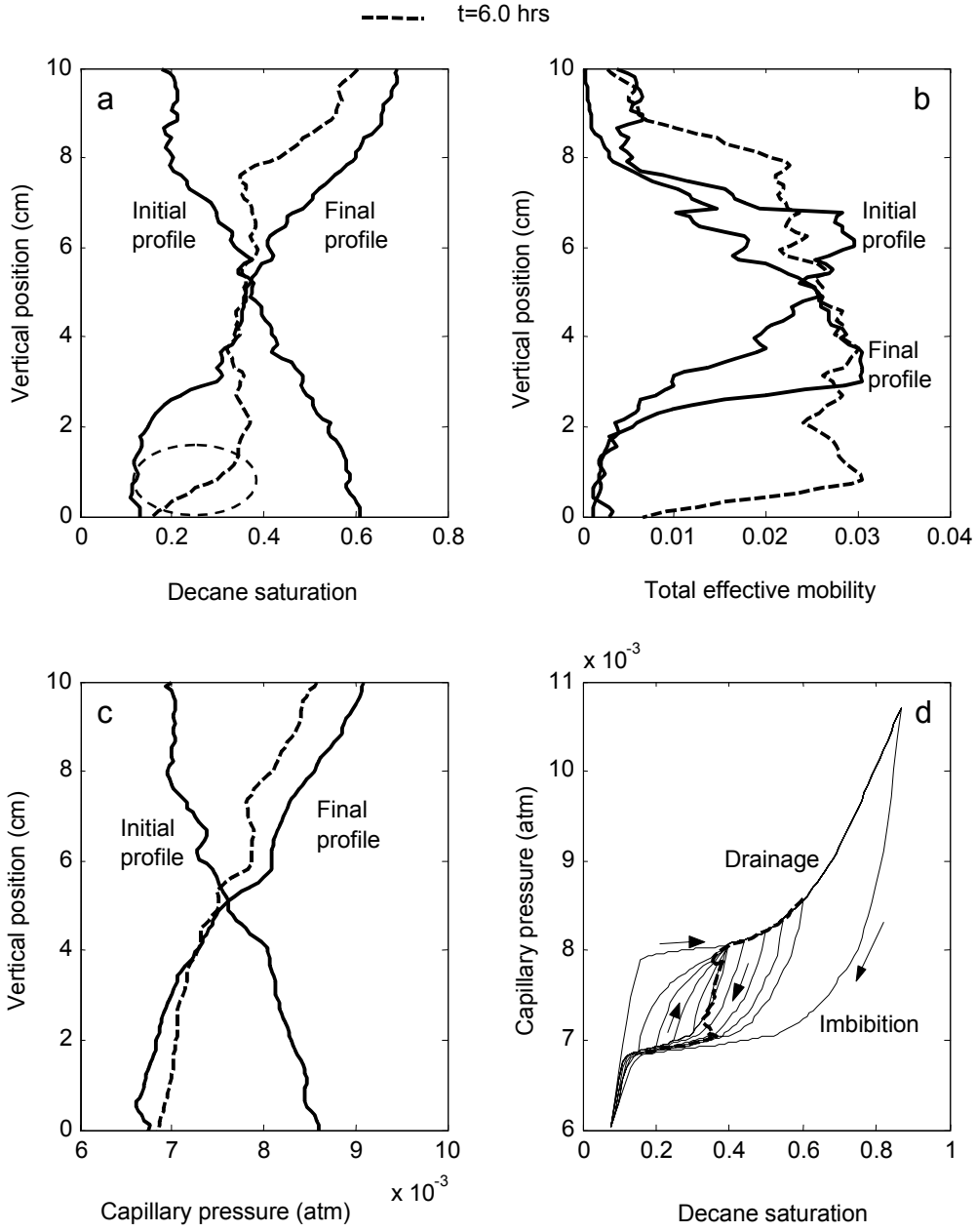

Figure 5.4i: History dependent simulation at t=6.0 hrs (Karpyn's experiment):
a. saturation profiles; b. total effective mobility profiles; c. capillary pressure profiles; d. dynamic capillary pressure curve on the capillary hysteresis loop and scanning curves.

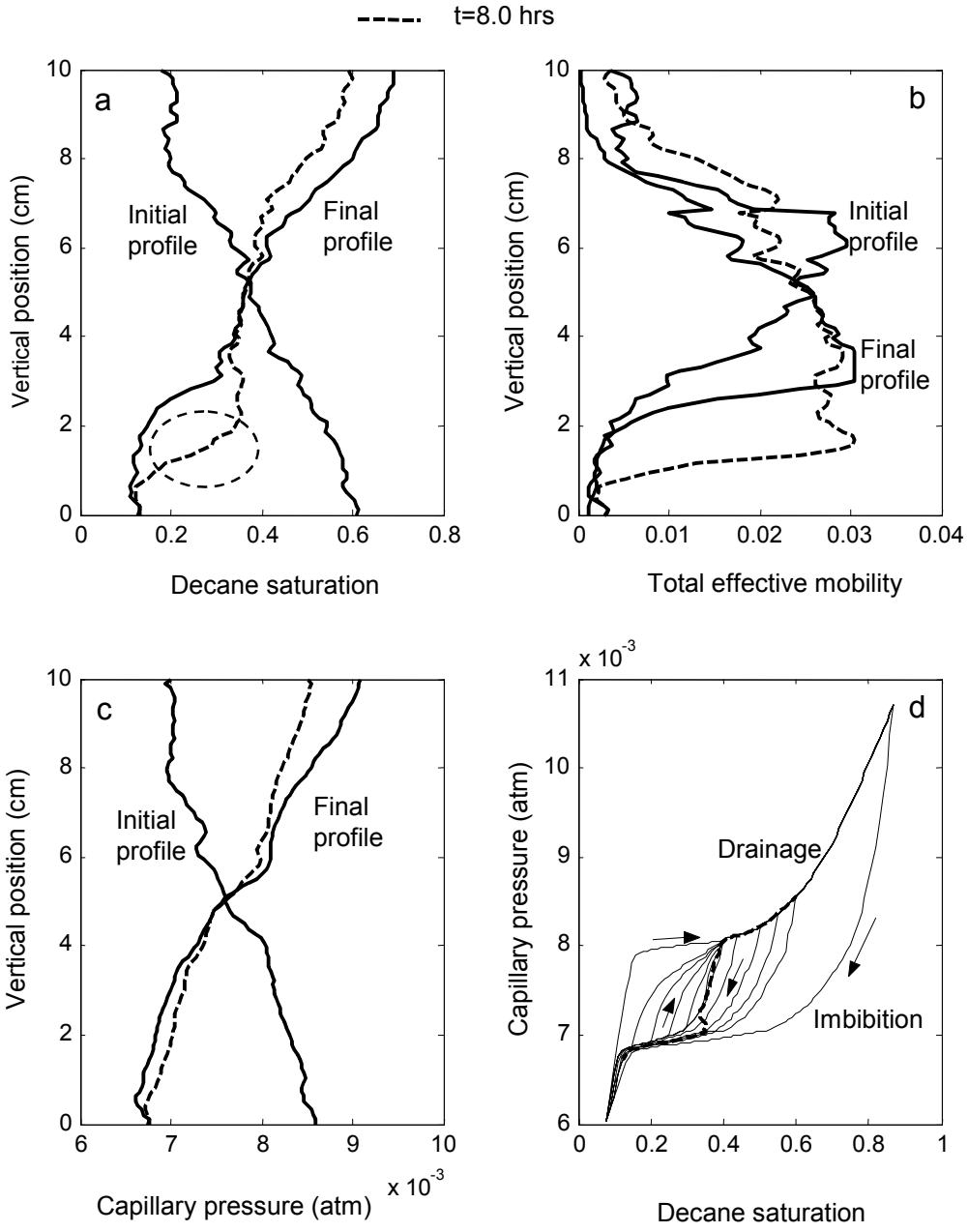

Figure 5.4j: History dependent simulation at t=8.0 hrs (Karpyn's experiment):
a. saturation profiles; b. total effective mobility profiles; c. capillary pressure profiles; d. dynamic capillary pressure curve on the capillary hysteresis loop and scanning curves.

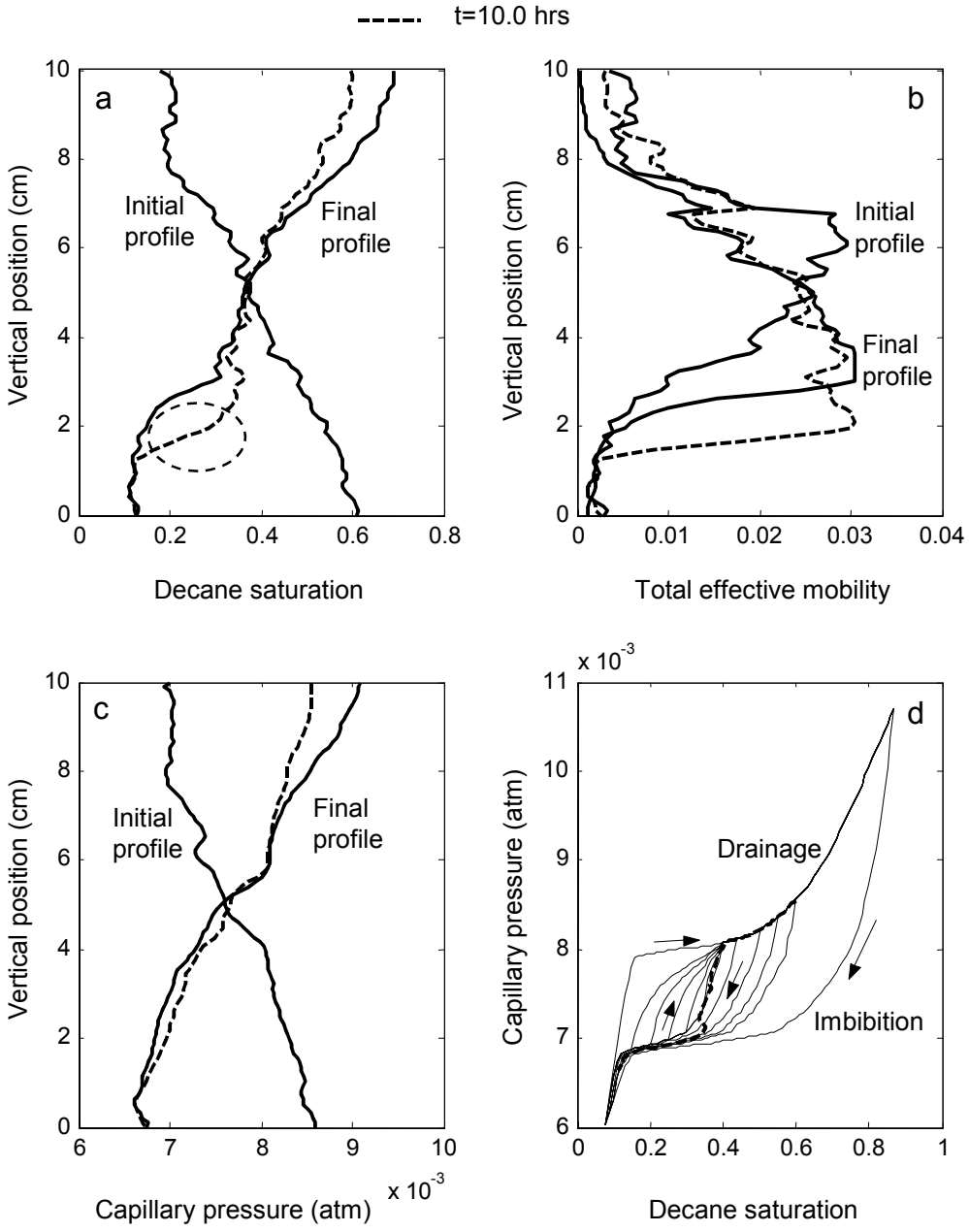

Figure 5.4k: History dependent simulation at t=10.0 hrs (Karpyn's experiment):
a. saturation profiles; b. total effective mobility profiles; c. capillary pressure profiles; d. dynamic capillary pressure curve on the capillary hysteresis loop and scanning curves.

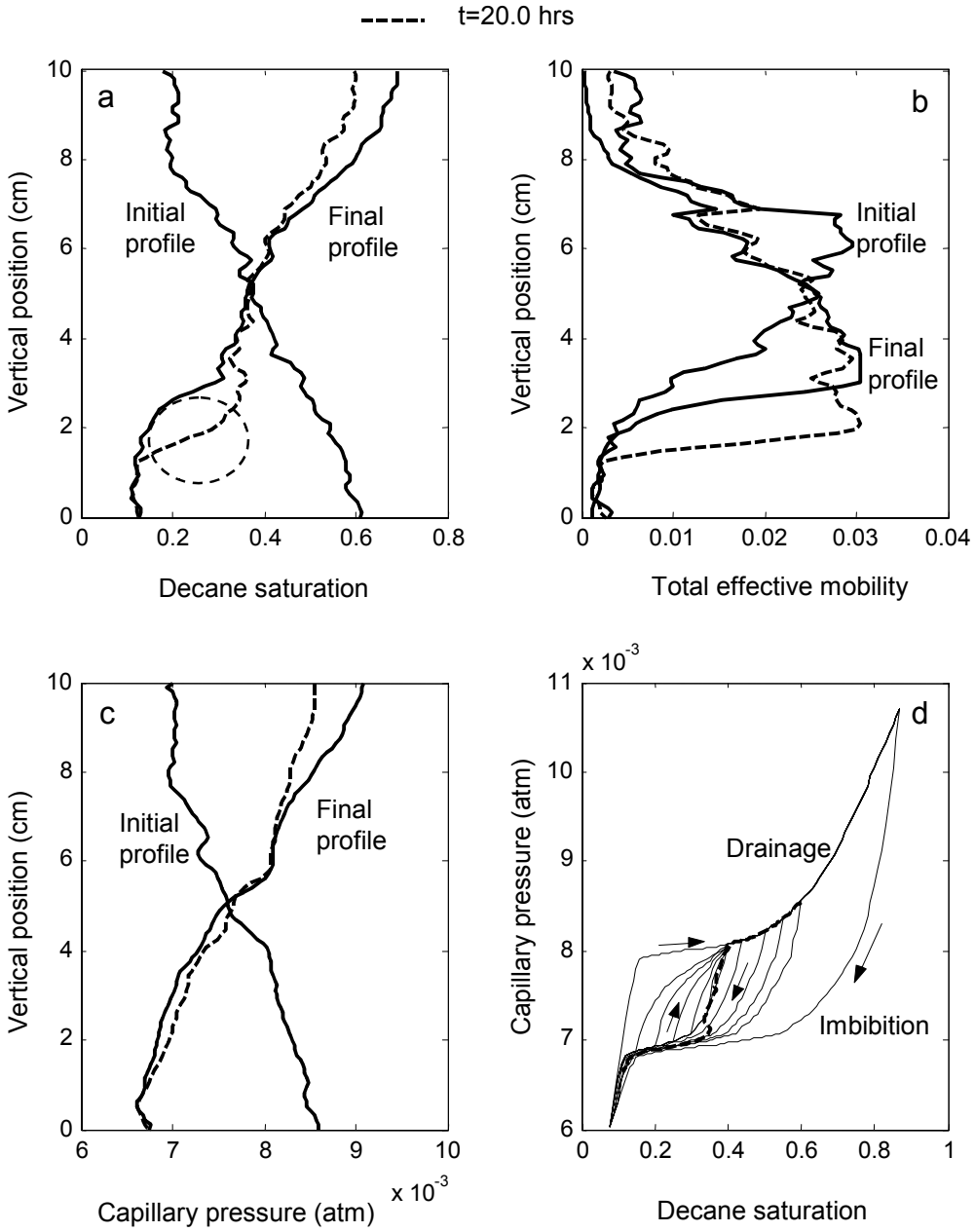

Figure 5.4l: History dependent simulation at t=20.0 hrs (Karpyn's experiment):
a. saturation profiles; b. total effective mobility profiles; c. capillary pressure profiles; d. dynamic capillary pressure curve on the capillary hysteresis loop and scanning curves.

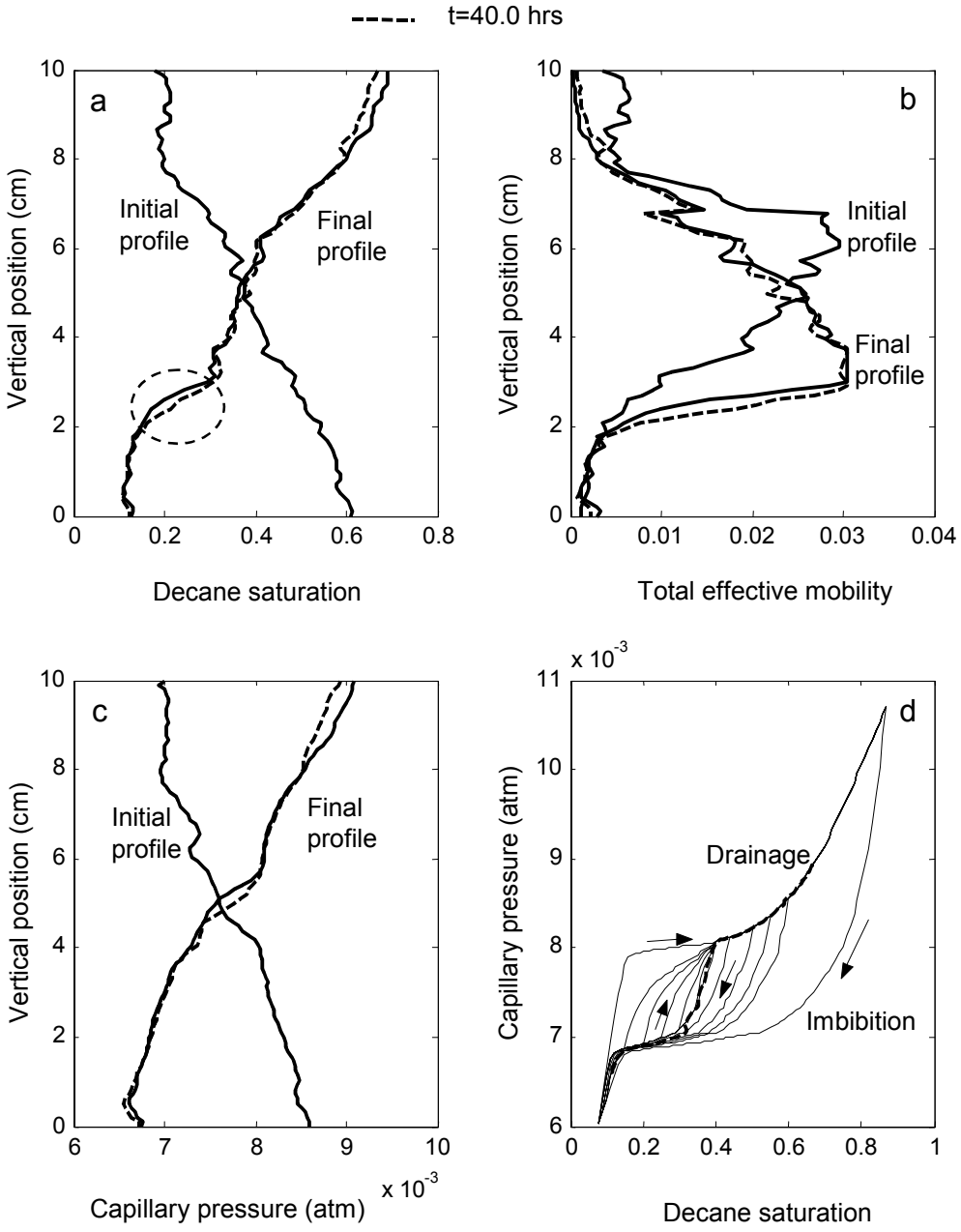

Figure 5.4m: History dependent simulation at t=40.0 hrs (Karpyn's experiment): a. saturation profiles; b. total effective mobility profiles; c. capillary pressure profiles; d. dynamic capillary pressure curve on the capillary hysteresis loop and scanning curves.

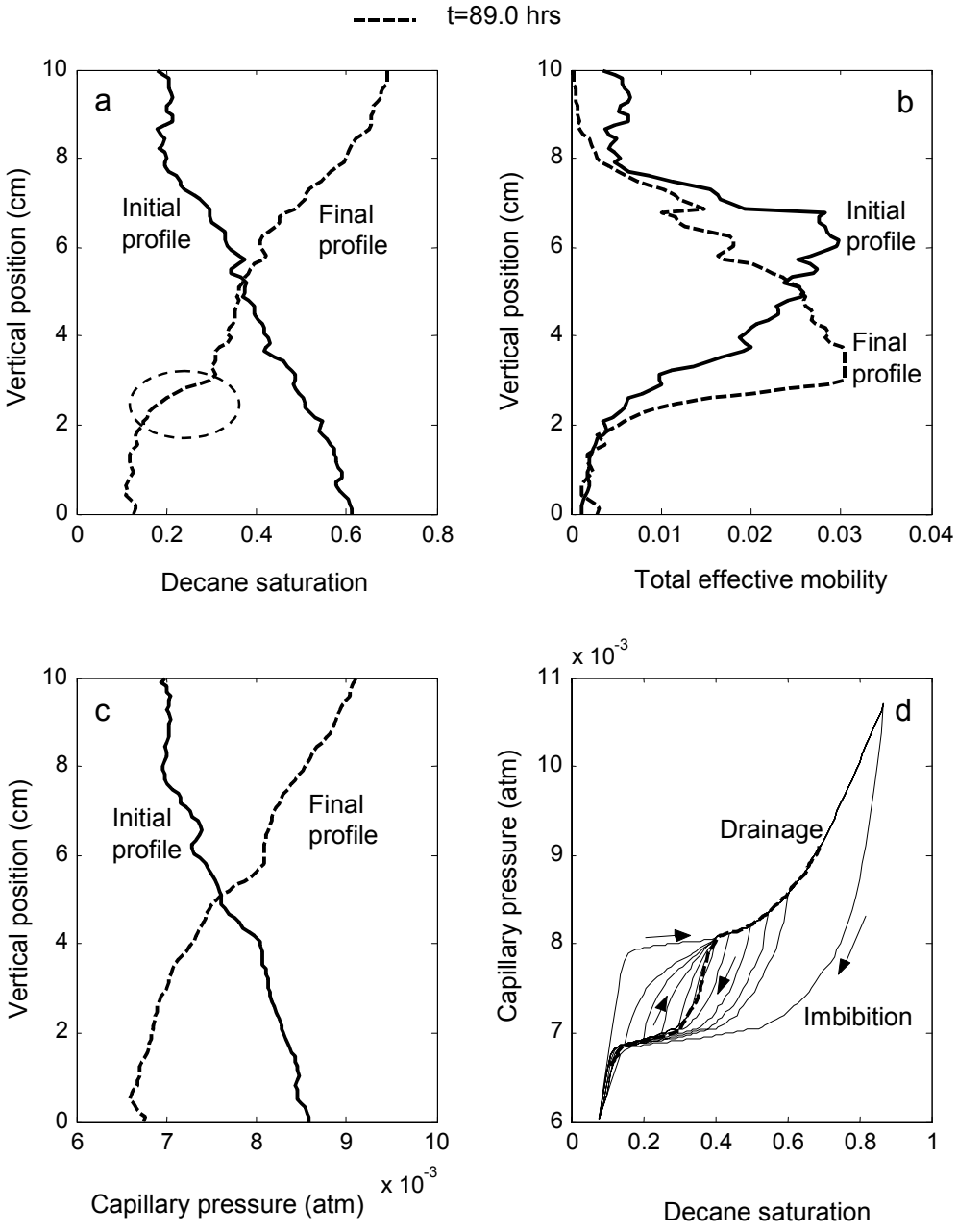

Figure 5.4n: History dependent simulation at t=89.0 hrs (Karpyn's experiment): a. saturation profiles; b. total effective mobility profiles; c. capillary pressure profiles; d. dynamic capillary pressure curve on the capillary hysteresis loop and scanning curves.

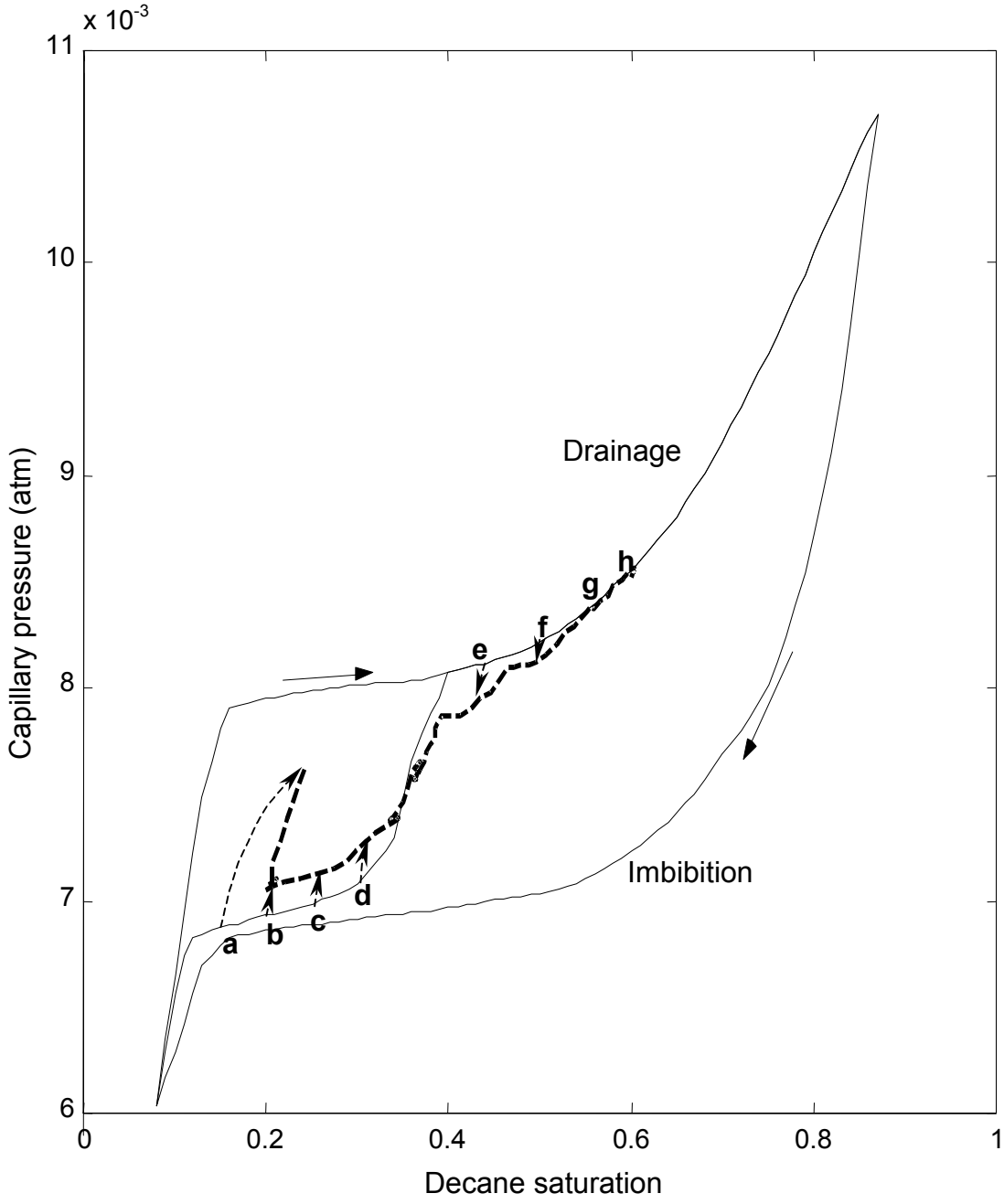

Figure 5.5a: Dynamic capillary pressure curve with its trajectories at t=0.2 hrs (Karpyn's Experiment).

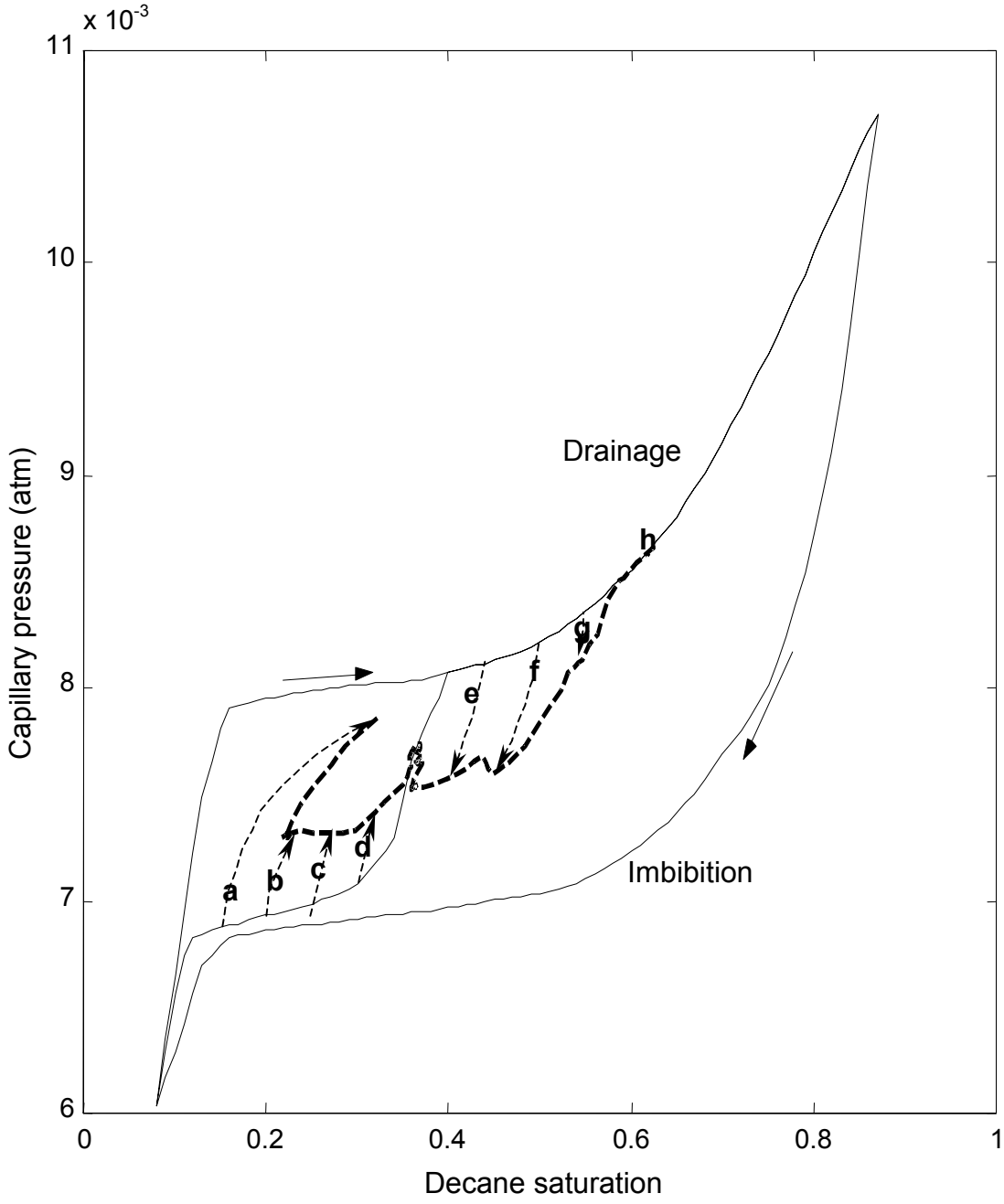

Figure 5.5b: Dynamic capillary pressure curve with its trajectories at t=0.6 hrs (Karpyn's Experiment).

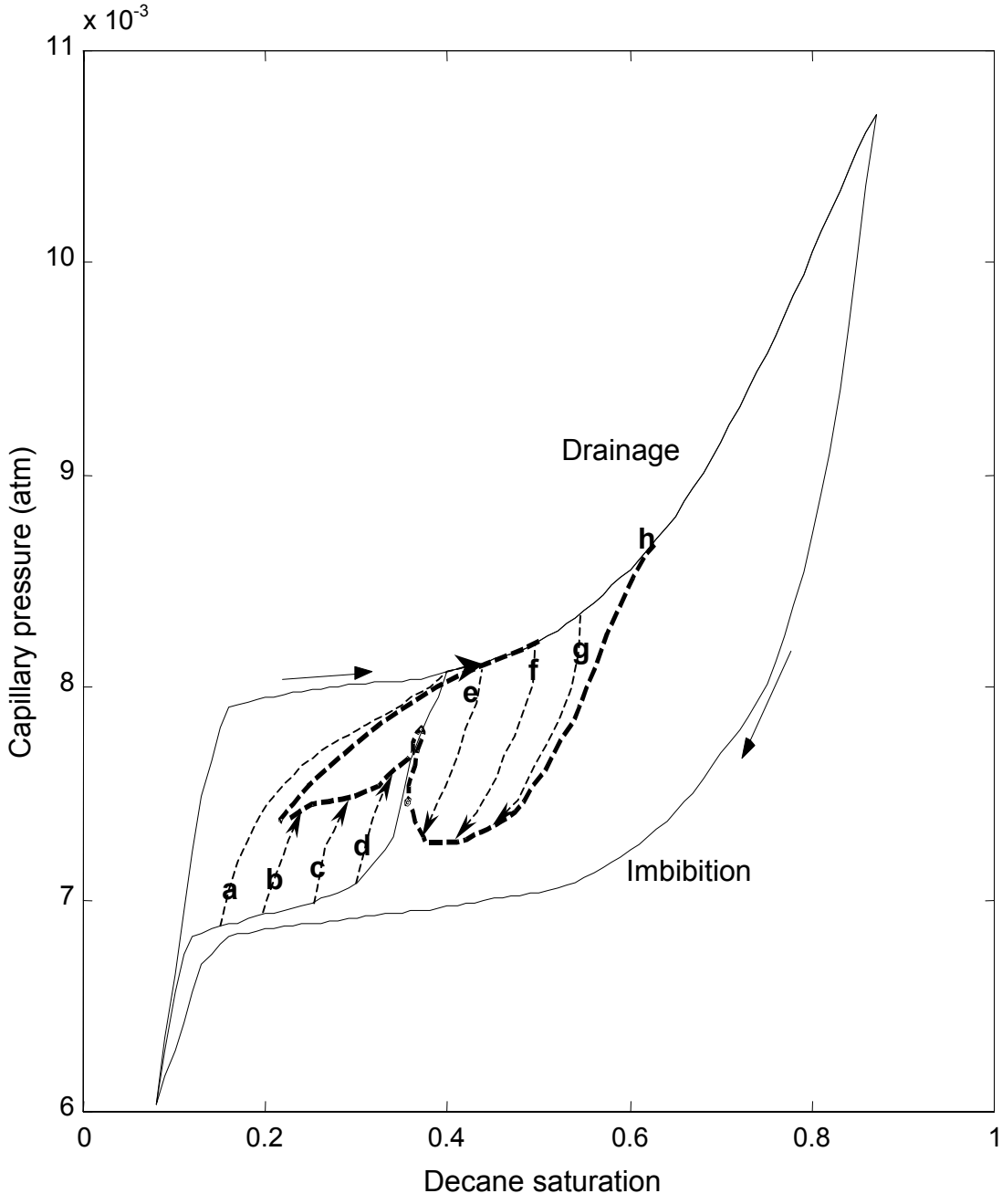

Figure 5.5c: Dynamic capillary pressure curve with its trajectories at t=1.0 hrs (Karpyn's Experiment).

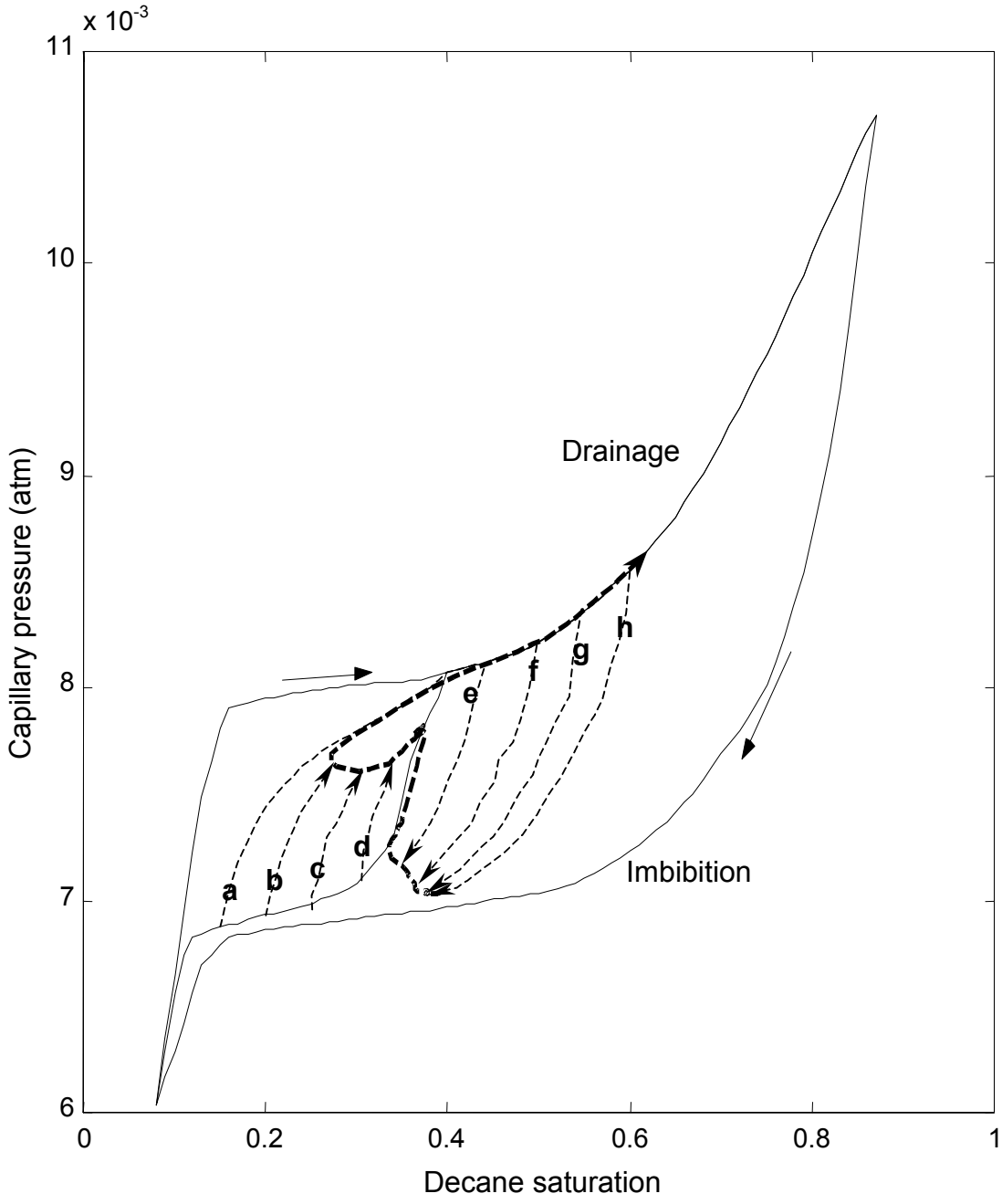

Figure 5.5d: Dynamic capillary pressure curve with its trajectories at t=4.0 hrs (Karpyn's Experiment).

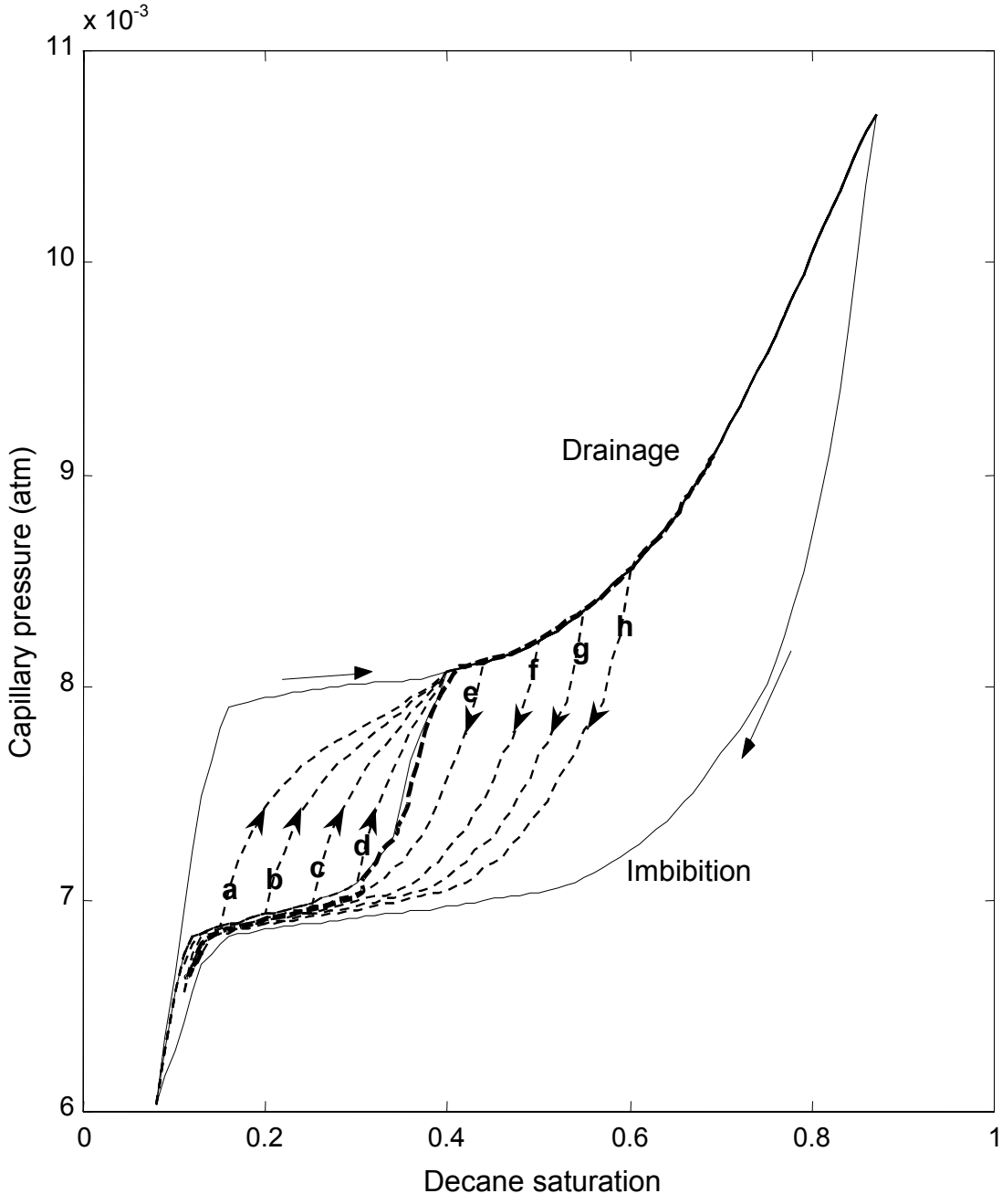

Figure 5.5e: Dynamic capillary pressure curve with its trajectories at t=89.0 hrs (Karpyn's Experiment).

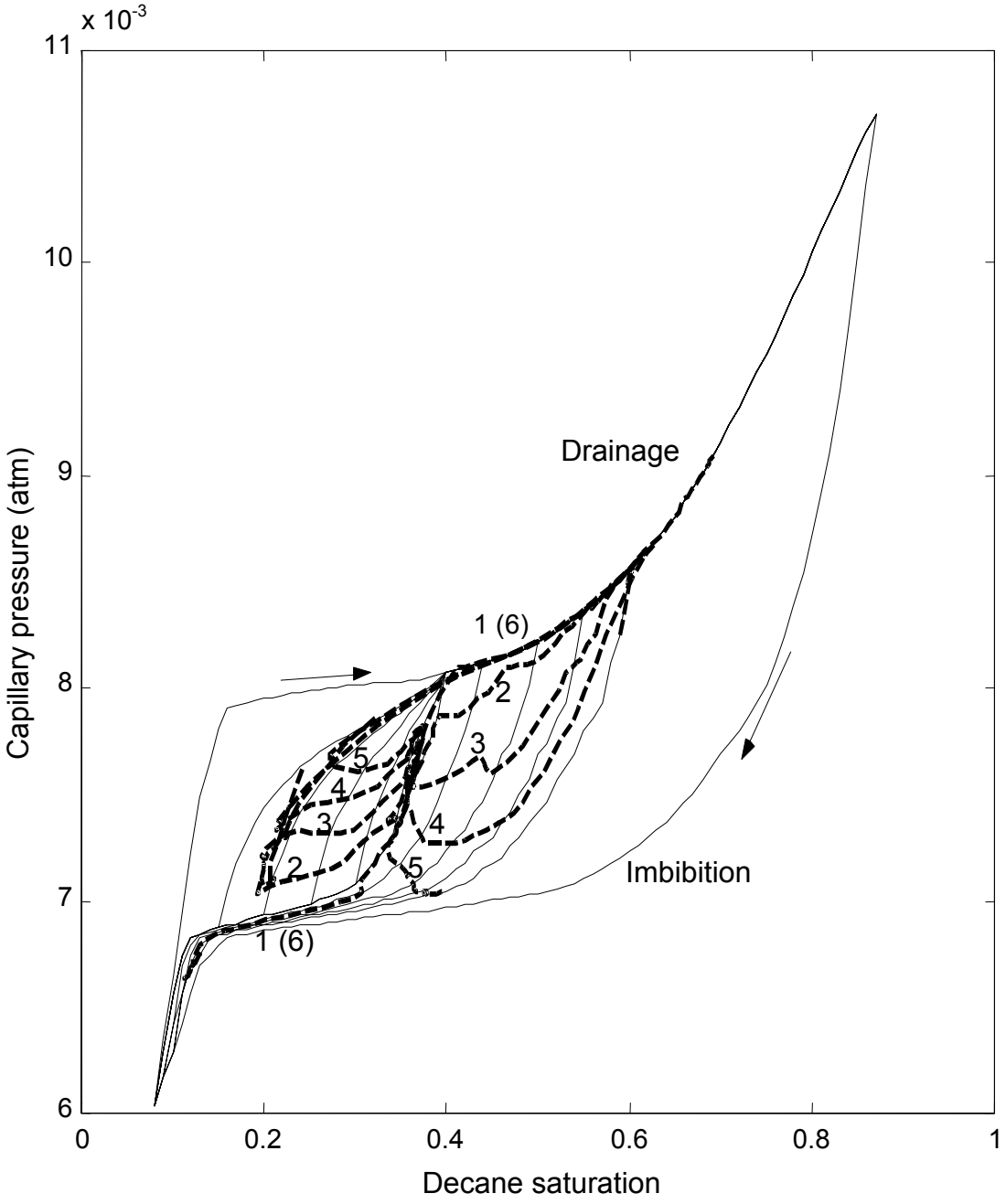

Figure 5.6: Dynamic capillary pressure curves at different times (Karpyn's Experiment).
1.initial condition; 2.t=0.2 hrs; 3.t=0.6 hrs;
4.t=1.0 hrs; 5.t=4.0 hrs; 6.t=89.0 hrs;

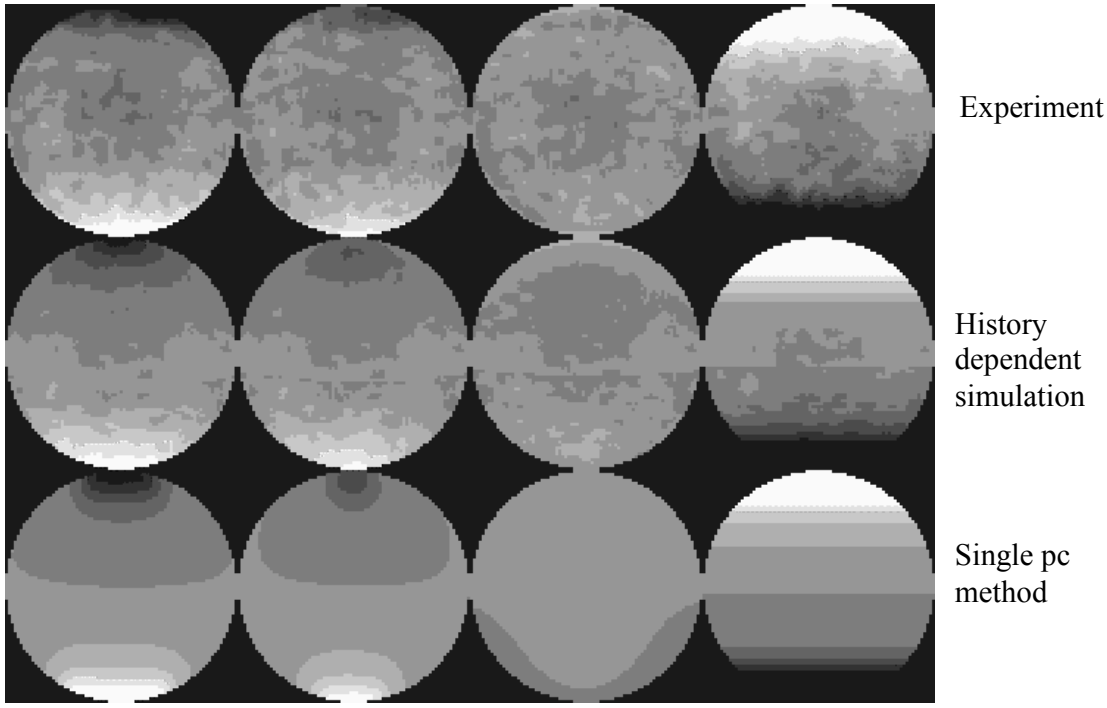

Figure 5.7: Comparison of saturation distribution images between the experiments (first row) and the two simulations. The third row images are obtained from single pc simulation and the middle row images are from history dependent simulation.

5.4 Factors Influencing the Formation of Fluid Banks.

The formation of fluid banks was observed both in Karpyn's experiments and in Briggs'. In Karpyn's experiments, there was also a decane bank at late time at the bottom of the core. Fluid banks form only in regions with high wetting phase saturation. Several factors contribute to the formation of fluid banks.

a) The shape of the capillary pressure curves. The shape of the capillary pressure curves plays an important role in bank formation. The positions of the bank correspond to flat zones (low gradient) in the capillary pressure curves (**Figures 5.4**). For example, in the early time of Karpyn's experiment Stage 2, the upper part of the sample follows the family of drainage-scanning curves. These curves sharply increase and flatten down to asymptotically approach the drainage capillary pressure curve. Therefore, in a short time, these points approach the flat zone of the capillary pressure curve. In the flat zone, the capillary force does not have much impact on the flow process, because its gradient, which is the driving force, is small. The same reason holds for the formation of the decane bank at the late time during the experiment – the lower part enters a flat zone on the imbibition capillary pressure curve. Without capillary pressure, the gravity force tends to segregate fluids by forming banks. **Figure 5.8** shows simulated saturation profiles without considering capillary pressure. The initial condition is from Barbu's experimental data. Therefore, the initial saturation profile is not very smooth. With only gravity and viscous forces, decane tends to accumulate at the top of core at a high saturation even at early time and benzyl alcohol tends to accumulate at the bottom.

In the experiments (Karpyn, Barbu and Briggs) discussed in this study, glass bead packs were used. When the wetting phase saturation increased in the system, the

relatively small pores were occupied by this wetting phase, while the non-wetting phase was in the large pores and saturation changes in this zone did not strongly affect the capillary pressure. In a naturally formed rock, the pore space is much more heterogeneous than in glass beads. Therefore, the capillary pressure gradient of this zone is supposedly larger than in the experiments, thus minimizing the tendency to form fluid banks. Briggs (1966) pointed out that no "bulge" (fluid bank) would form if the initial saturation was evenly distributed, such as Stage 1 in Karpyn's experiment. This conclusion was made based on the experimental observation from Templeton (1962). From observation of the experimental data, decane saturation of the bank (at the top of the core) is always lower than the average saturation. If the system starts with an evenly distributed saturation, the condition required to form fluids banks is never satisfied. But at the bottom of the core, it can form a shock if there is a flat capillary pressure at that position. This can be observed from the saturation profile of Karpyn's experiments (**Figures 4.28a-b**).

b) The height of the system. Counter-current flow represents a balance between capillary and gravity forces. Therefore, the height of the reservoir in which flow occurs plays an important role in counter-current flow. In Barbu's experiments, only a hint of a bank was observed at the top of the saturation profiles. Simulation of this experiment with a larger diameter core (larger height of the saturation profiles) yields an oil bank at the top. The simulated saturation profiles are shown in **Figure 5.9**. When the saturation profiles in **Figure 5.9** are cut from 1 cm to 6 cm, which then has the same diameter (height) as the core in barbu's experiment, there is a hint of the bank at the top (circle in **Figure 5.9**). The effect of the height of the core in the flowing direction can also be seen

when comparing Barbu's and Karpyn's experiments. In Karpyn's experiments, the height of the core in the flowing direction was 10 cm, which is twice of the height of barbu's core. Correspondingly, there is a fluid bank in Karpyn's experiment Stage 2, but there is only a hint in Barbu's experiments.

To prove the height effect, another simulation was implemented. In this simulation, Karpyn's core was cut from 1.67 cm from bottom, where the decane shock diminishes, to 8.13 cm from bottom. The average saturation of the cut portion is preserved. **Figure 5.10** shows the simulated saturation profiles, which are very similar to saturation profiles in Barbu's experiments. The hint of the bank is shown clearly at the top of the sample.

Briggs' cores with a larger height than karpyn's cores also exhibited fluid banks in the counter-current flow process. This also supports the observation that large heights tend to yields fluid banks in counter-current flow. In the following section, a mechanistic explanation with the aid the history dependent simulation is provided.

In the case that the core has a large height, the segregation in each stage would be complete and the results of the segregation yield three regions in the vertical position: a heavy phase zone, a transition zone, and a light phase zone, from bottom to top. In the heavy phase zone, the heavy phase has an almost constant and maximum saturation. After the core is rotated 180°, this zone is located at the top of the core.

Karpyn's experiment is used as an example. Saturation profiles, total effective mobility profiles, and the dynamic capillary pressure curves at t=0.6 hours and t=3.0 hours for Karpyn's experiments are shown in **Figure 5.11** and **Figure 5.12**, respectively. Above point **C** in the saturation profiles, the initial condition shows a close to constant

saturation at the top of the core. This region followed the same capillary pressure scanning curve in the hysteresis loop, because they have the same saturation and saturation history. The segment **AB** of the capillary pressure curve in **Figure 5.11c** corresponds to the upper wing of the bank also denoted as **AB** shown in saturation profiles in **Figure 5.11a**. This upper wing of the bank is also shown in the mobility and capillary pressure profiles in **Figure 5.11b**. The mobility profile shows an upward mobility increase in this portion, which helps the displacement in this region, but the capillary pressure profile shows a positive slope, which restrains the flow in the region. At t=3.0 hours, the capillary pressure increases up to point **A** in the capillary pressure curve in **Figure 5.12c**. The **ABC** portion of the capillary pressure curve corresponds to the upper wing of the bank shown in **Figure 5.12a**. This curve is continuous with a relatively small slope. But in the case of using single capillary pressure curve, there is a very large slope in the middle part, which restrains the saturation of the upper wing of the bank from passing through the middle point. That is the reason that the single pc method failed to simulate Karpyn's experiment saturation. The **DOE** portion of the saturation profiles for both t=0.6 hours (**Figure 5.11a**) and t=3.0 hours (**Figure 5.12a**) has almost a constant decane saturation, which results in a constant and high total effective mobility for both cases (**Figure 5.11b** and **Figure 5.12b**). On the dynamic capillary pressure curve (the thick dashed line in **Figure 5.11c**), this portion is concentrated at one spot and vertical saturation gradient is small, hence the vertical capillary pressure gradient in space is low. All the above conditions help the flow through the middle part of the sample.

c) The average saturation. A comparison of barbu's and Karpyn's experiments implies that the average saturation of the system has an impact on the formation of fluid

banks. The average decane saturation of barbu's experiments was 0.4, and in Karpyn's experiments, it was 0.52. With increasing decane saturation, fluid banks are less likely to be formed in the system. This is because there is not enough benzyl alcohol at the top to form a bank. **Figure 5.13** shows the saturation profiles obtained from two synthetic cases with different average decane saturation: Case **A** - 0.4, Case **B** - 0.55. The other parameters used in these two cases were the same as in Karpyn's experiment. The initial saturation profiles for both cases were obtained numerically by rotating the core 180° after Stage 1, which was initiated from an evenly distributed saturation profile. Case **A** shows a clear fluid bank at the top but case **B** shows only a tendency to form a bank.

d) The shape of the core. Another difference between Barbu's and Karpyn's experiments was the shape of the core. The core in barbu's experiments was round and in Karpyn's experiments it was square. Two simulations were implemented with equal parameters except that one core had a circular shape and the core had a square shape. In Stage 1 of the simulation, the initial saturation was evenly distributed. After it was rotated 180°, the final saturation profile of the Stage 1 was used as the initial saturation profile for Stage 2. The simulated saturation profiles are shown in **Figure 5.14**. The fluid bank at the top is more pronounced in the square core than that in the round core. In the round core, the absolute quantity of heavy wetting phase at the top is less than that in the square because of the shape, which reduces the chance to form a bank. Another reason is that in the round core, the heavy wetting phase diverges when it flows down and the light non-wetting phase converges to the top, which helps segregating the fluids. With the rapid segregation process, it is less likely that a bank would form in the round core.

Comparison of the two saturation profiles shows that the round core yields higher decane saturation as a function of time at the top of the core.

e) Other factors. Another possible factor that affects the formation fluid banks is the counter-current flow direction with respect to the convective co-current flow direction prior to the onset of the counter-current flow. In Barbu's experiments, the counter-current flow direction is perpendicular to the co-current flow direction but in Karpyn's experiments these two directions are the same. The convective co-current flow prior to the counter-current flow may create some preferential flow paths. The co-current flow direction prior to the counter-current flow process might affect controlling parameters such as relative permeabilities and capillary pressure. The co-current flow direction was taken into account in the simulation, but the simulation results match the experimental data. The effects of the direction of convective flow prior to the counter-current flow are currently unclear.

Because the benzyl alcohol bank has a low decane saturation, which results in a low mobility, the flow velocity at the benzyl alcohol bank is low. Consequently, the formation of fluid banks slows down the segregation process. Therefore, it is not desirable to have a fluid bank for gas storage in an aquifer. In a fractured reservoir, this may affect the spontaneous imbibition recovery process in the vertical direction. In this case, both capillarity and gravity forces will affect the recovery process.

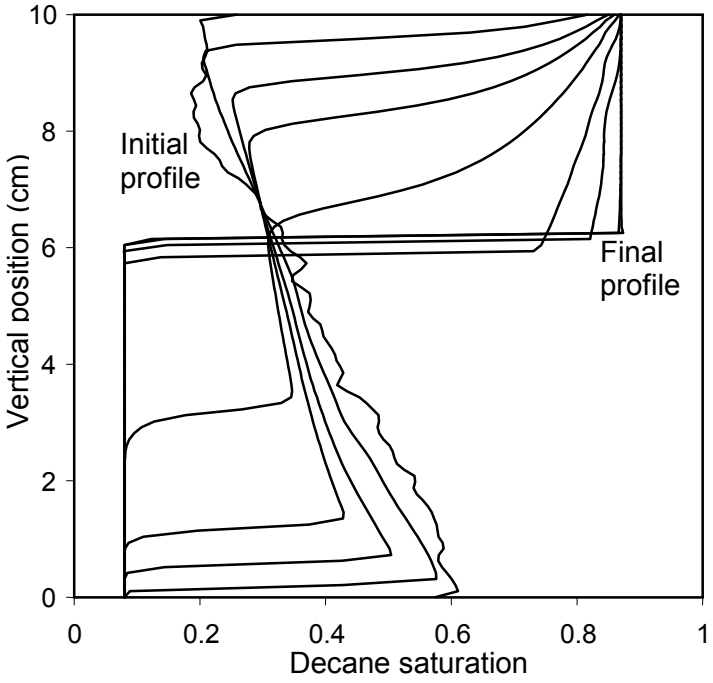

Figure 5.8: Simulated saturation profiles without capillary pressure.

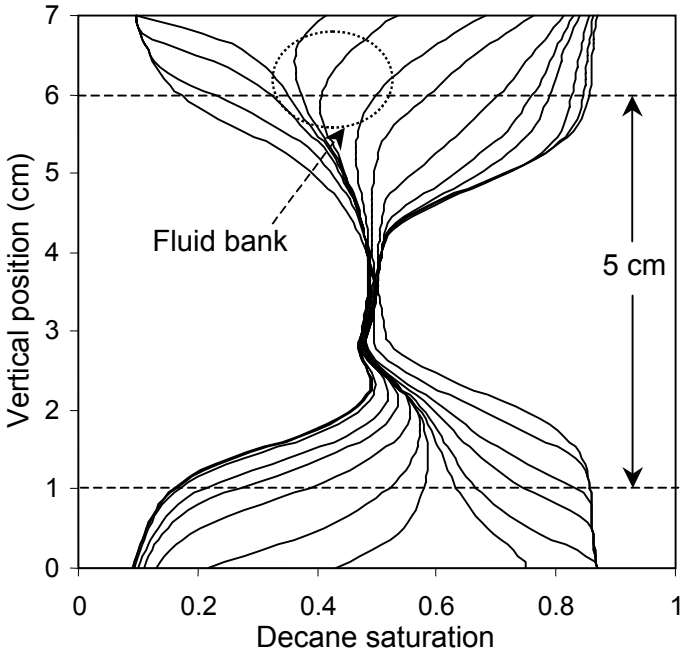

Figure 5.9: Simulated saturation profiles with a core diameter 7 cm.

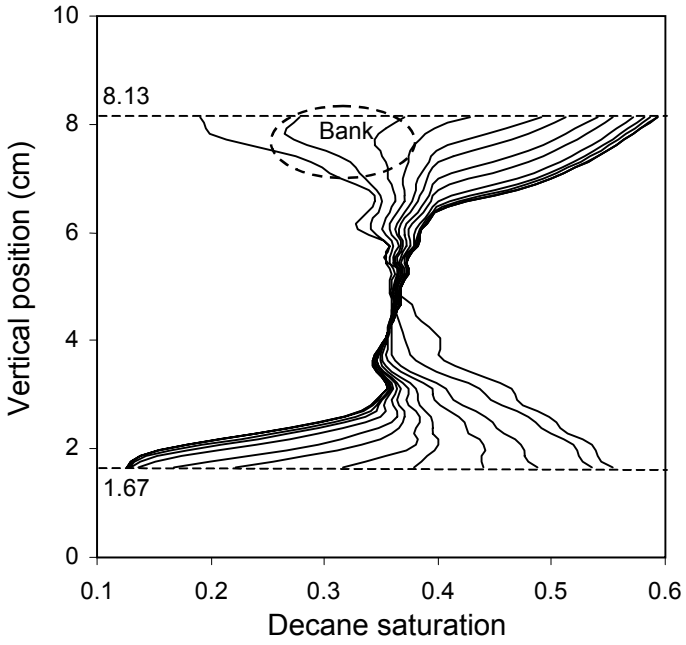

Figure 5.10: Simulated decane saturation profiles of Stage 2 in Karpyn's experiment after the core was cut from 1.67 cm (bottom) to 8.13 cm (top). The average saturation is preserved.

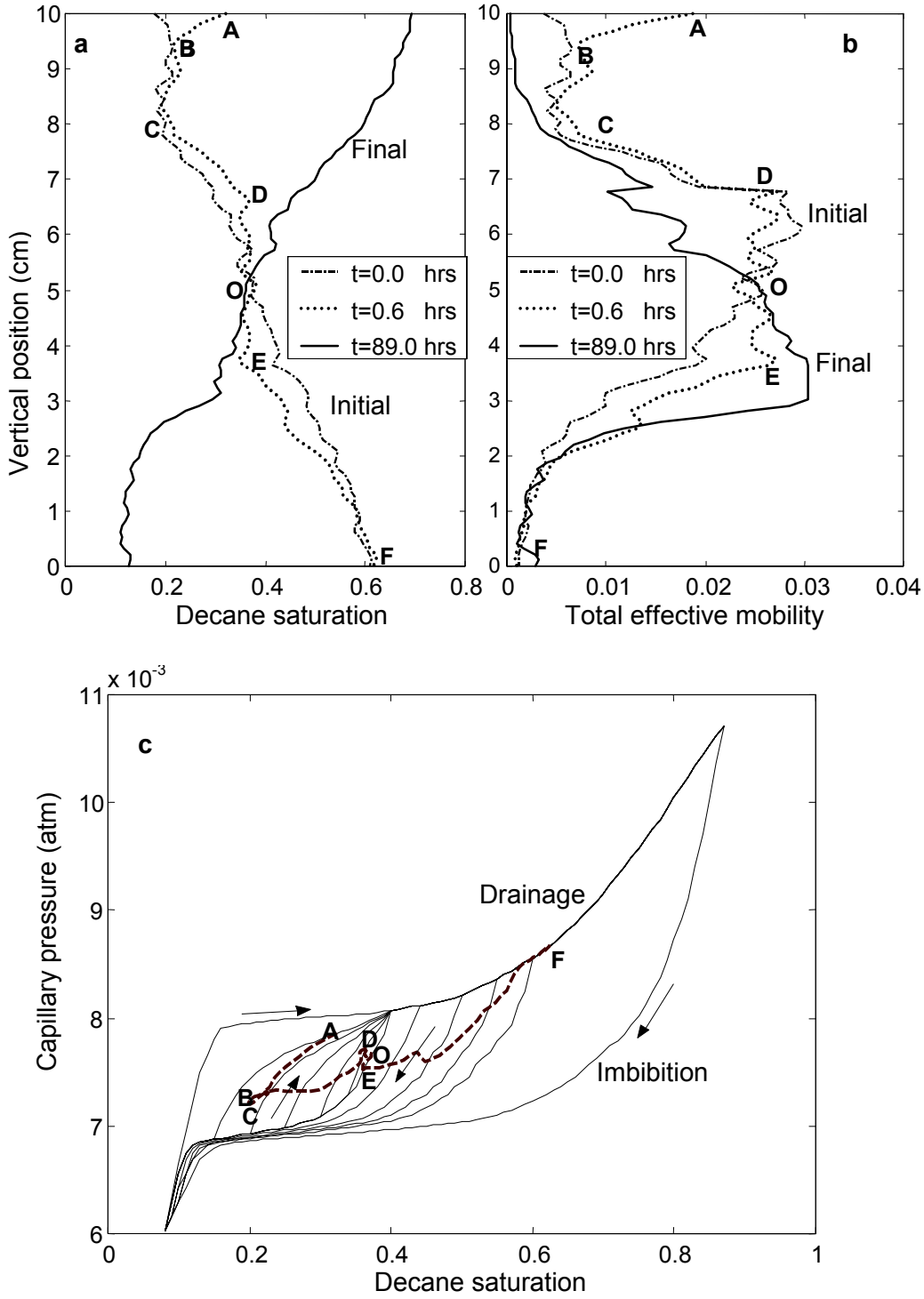

Figure 5.11: Detailed representation of the parameters for history dependent simulation at t=0.6 hrs (Karpyn's experiment): a. saturation profiles; b. total effective mobility profiles; c. capillary pressure trajectory.

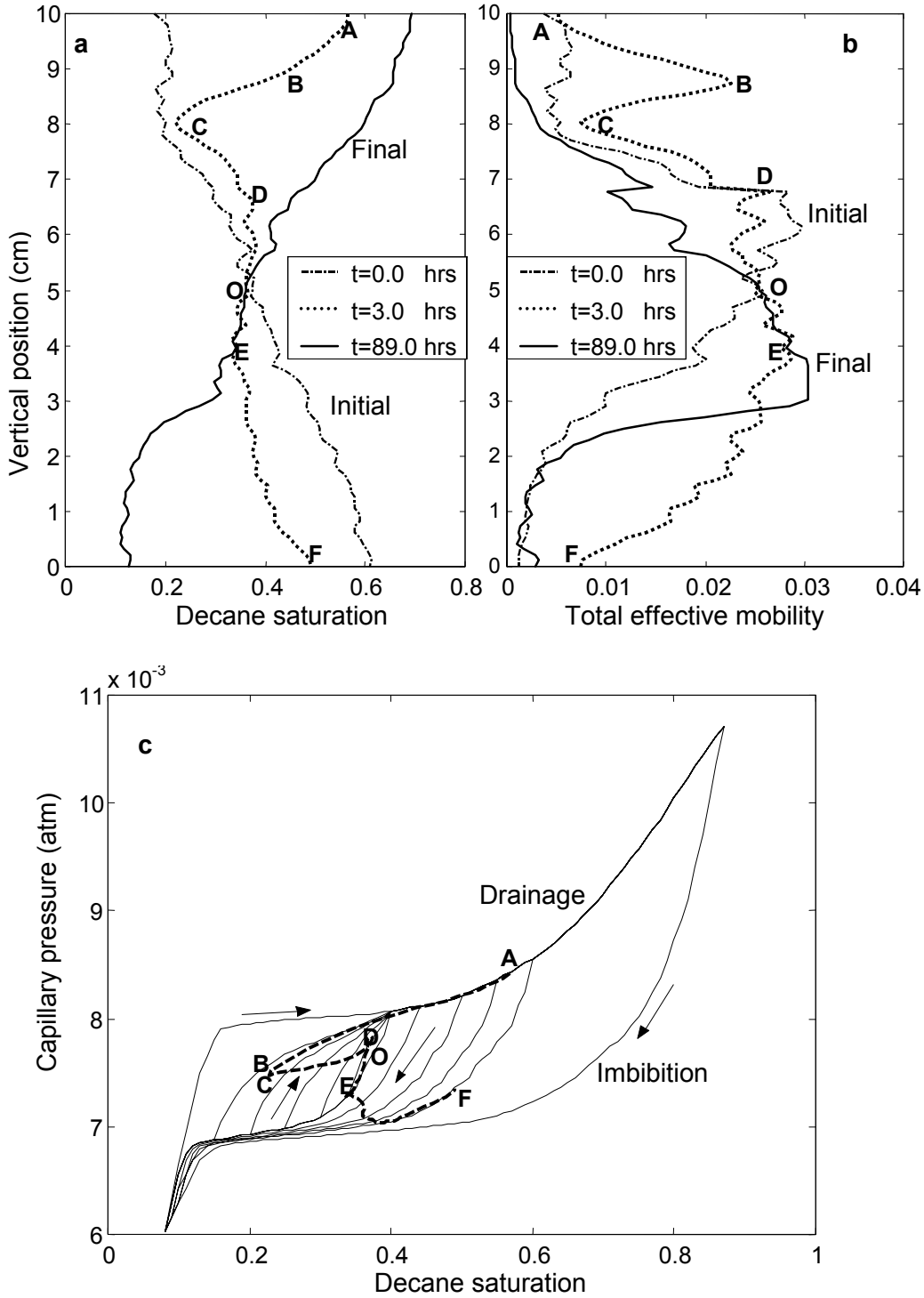

Figure 5.12: Detailed representation of the parameters for history dependent simulation at t=3.0 hrs (Karpyn's experiment): a. saturation profiles; b. total effective mobility profiles; c. capillary pressure trajectory.

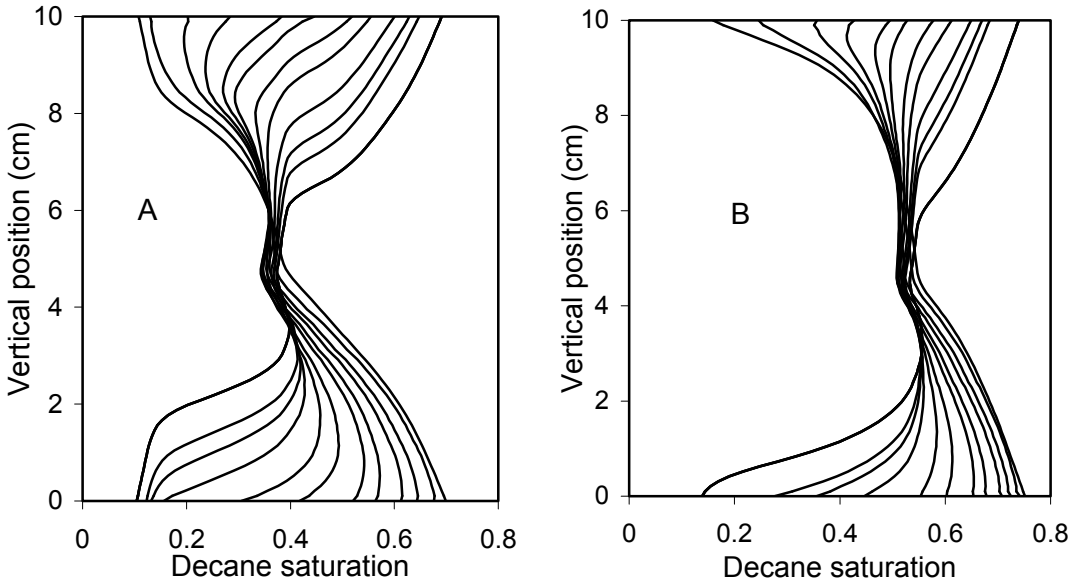

Figure 5.13: Simulated decane saturation profiles with different average decane saturation, Case A: 0.40; Case B: 0.55.

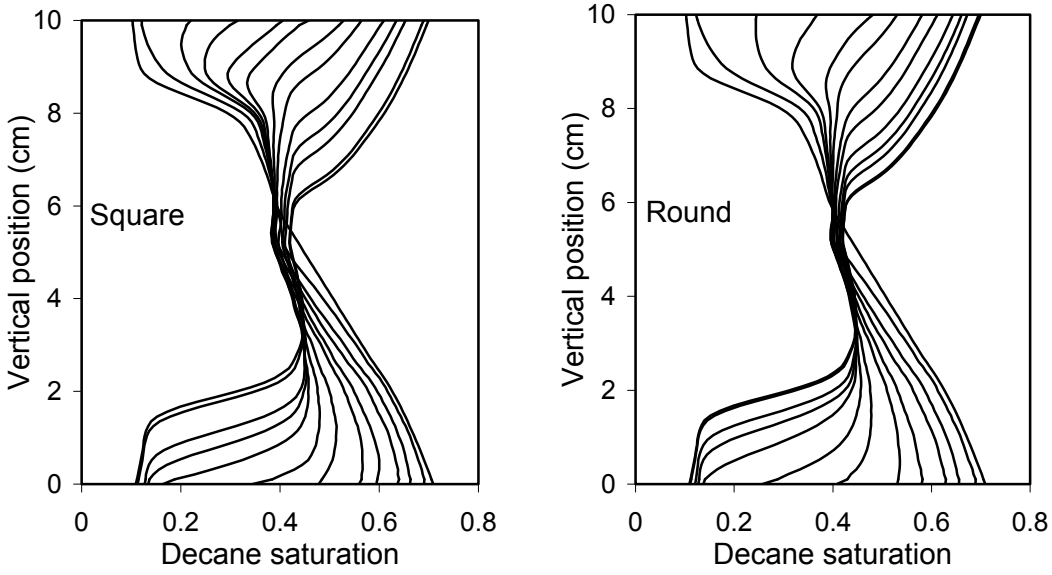

Figure 5.14: Simulated decane saturation profiles with average decane saturation 0.43. The shape of the core is different: one is square and the other is a circle.

CHAPTER 6

CONCLUSIONS

Using the method for extracting capillary pressures and relative permeabilities from experiments presented in this research, the following conclusions are made.

1. The counter-current flow can be correctly modeled only if the saturation history and capillary hysteresis are taken into account. In this method, different regions use different relative permeabilities and each cell of the core is assigned a capillary pressure curve based on its current saturation and saturation history. This general method can be applied to cases with and without fluid banks. The single pc method can only be applied to cases without fluid banks. In the case of a round core, history dependent modeling can reduce artifacts caused by the shape of the core.
2. In the history-dependent-modeling method, the capillary pressure curve of the process is dynamically changing temporally and depends on the saturation distribution and saturation history of the system. The dynamic capillary pressure curve approaches the initial one at the end of the counter-current flow process.
3. The formation of phase banks and shocks depends on many factors such as the shape of the capillary pressure curves, the height of the system, the average saturation and the shape of the core. Flat regions in the capillary pressure curves tend to help the formation of fluid banks. In Karpyn's experiments, the formation of banks at the top of the core depends on the shape of the drainage capillary pressure curve and the bank at the bottom of the core depends on the shape of the

imbibition capillary pressure curve. The height of the core has a positive impact on the formation of fluids banks. The higher the core is, the more chance it has to form a bank. Higher average non-wetting phase saturation tends to prevent the formation a bank, because there is not enough wetting phase at the top fo the core. A square core has more chance to form a bank in counter-current flow than a round core. The flow process in a round core is faster than in a square one.

4. Compared to co-current flow, the drainage relative permeabilities as well as the BA imbibition relative permeabilities are smaller in counter-current flow, but the Decane imbibition relative permeabilities might be larger. The total effective mobility of counter-current flow is always smaller than that of co-current flow.

REFERENCES

Adam Neil K.: Physics and chemistry of surfaces, 1941.

Akin S., and Birol Demiral M.R.: Effect of Flow Rate on Imbibition Three-Phase Relative Permeabilities and Capillary Pressures, SPE 38897, Proceedings of the SPE Annual Technical Conference and Exhibition, San Antonio, Texas, 5-8 October 1997.

Akin S., and Kovscek A.R.: Imbibition Studies of Low Permeability Porous Media, SPE 54590, Proceedings of SPE Western Regional Meeting, Anchorage, Alaska, 26-27 May 1999.

Al-Wadahi M.: Interfacial Tension Behavior of Water *n*-Decane and Benzyl Alcohol Mixtures, MS thesis, The Pennsylvania State University, University Park, Pennsylvania, 1994.

Al-Wadahi M., Grader A.S., and Ertekin T.: An Investigation of Three-Phase Counter-Current Flow Using X-Ray Computerized Tomography and Neuro-Simulation Modeling, SPE 63146, Proceedings of SPE Annual Technical Conference and Exhibition, Dallas, Texas, 1-4 October 2000.

Amyx J. W., Bass JR., D.M., and Whiting R.L.: Petroleum Reservoir Engineering (Physical Properties), 1960.

Archer J.S., and Wong S.W.: Use of a Reservoir Simulator to Interpret Laboratory Waterflood Data, *SPEJ,* pp 343-47, December 1973.

Babadagli T.: Scaling Co-Current and Counter-Current Capillary Imbibition for Surfactant and Polymer Injection in Naturally Fractured Reservoirs, SPE 62848,

Proceedings of the SPE/AAPG Western Regional Meeting, Long Beach, California, pp 19-23, June 2000.

Barbu A., Hicks P.J., and Grader A. S.: Experimental Three-Phase Flow in Porous Media: Development of saturated Structures Dominated by Viscous Flow, Gravity, and Capillarity, *SPEJ,* 4(4), December 1999.

Blair P.M.: Calculation of Oil Displacement by Countercurrent Water Imbibition, *SPEJ,* pp 195-202, September 1964.

Bourblaux B.J. and Kalaydjian F.J.: Experimental Study of Cocurrent and Countercurrent Flows in Natural Porous Media, *SPERE,* pp 361-68 August 1990.

Briggs J.E.: Countercurrent Gravity Segregation in Porous Media. Ph.D. Thesis, University of Michigan, 1963.

Briggs J.E., and Katz D.L.: Drainage of Water from Sand in Developing Aquifer Storage. SPE 1501, Proceedings of the 41st Annual Fall Meeting of the Society of Petroleum Engineers of AIME, Dallas, TX. U.S.A., 02-05 October 1966.

Buckley S.E. and Leverret M.C.: Mechanism of Fluid Displacement in Sands, TRANS. AIME, 146, pp 107-116, 1942.

Cardwell W.T. Jr. and Parsons R.L. Gravity Drainage Theory, TRANS. AIME 179, pp 199-210, 1949.

Chatzis I., Kantzas A., and Aullien F.A.L.: On the Investigation of Gravity-Assisted Inert Gas Injection Using Micromodels, Long Berea Sandstone Cores, and Computed-Assisted Tomography, SPE 18284, Proceedings of the SPE Annual Technical Conference and Exhibition, Houston, TX, 2-5 October 1988.

Chavent G., Cohen G., and Espy M.: Determination of Relative Permeability and Capillary Pressure by an Automatic Adjustment Method, SPE 9237, Proceedings of the SPE Annual Technical Conference and Exhibition, Dallas, 21-24 September 1980.

Corey A.T., Rathjens C.H., Henderson J.H., and Wyllie M.R.J.: Three-Phase Relative Permeability, *JPT*, pp 63-65. November 1956.

Cromwell V., Kortom D.J., and Bradley D.J.: The Use of a Medical Computed Tomography(CT) to Observe Multiphase Flow in Porous Media, SPE 13098, Proceedings of the Society of Petroleum Engineers of AIME 59th Annual Technical Conference and Exhibition, Houston, Texas, 16-19 September 1984.

Das S.K. and Butler R.M.: Countercurrent Extraction of heavy oil and Bitumen, SPE 37094, Proceedings of the SPE International Conference on Horizontal Well technology, Calgary, Canada, 18-20 November 1996.

Dumore J.M. and Schols R.S.: Drainage Capillary-pressure Functions and the influnce of Connate Water, *SPEJ*, pp 437-44, October 1974.

Enderby A.J.: The Domain Model of Hysteresis: 2. *Trans. Faraday Soc.,* Vol 52, pp 106-20, 1956.

Everett D.H., and Whitton W.I.: A General Approach to Hysteresis. *Trans. Faraday Soc.,* Vol 48 , pp 106-20, 1952.

Everett D.H., and Smith F.W.: A General Approach to Hysteresis: 2. *Trans. Faraday Soc.,* Vol 50, pp 187-97, 1954a.

Everett D.H.: A General Approach to Hysteresis: 3. *Trans. Faraday Soc.* Vol 50, pp 1077-96, 1954b.

Everett D.H.: A General Approach to Hysteresis: 4. *Trans. Faraday Soc*., Vol 51, pp 1551-57, 1955.

Fayers F.J. and Sheldon J.W.: The effect of Capillary Pressure and Gravity on Two-Phase Flow in a porous Medium, TRANS. AIME, Vol. 216, pp 147, 1959.

Ganapathy S., et al: Simulation of Heteregeneous Sandstone Experiments Characterized with CT Scanning. *SPEFE*, December 1993.

Gill P.E., Murray W., and Wright M.H.: Practical Optimization, Academic Press, New York, 1981.

Gomez S., Oliver G. and Barker W.J.: Gradient-Based History Matching with a Global Optimization Method, SPE 56756, Proceedings of the SPE Annual Technical Conference and Exhibition, Houston, Texas, 3-6 October 1999.

Grader A.S., and O'Meara Jr., D.J.: Dynamic Displacement Measurements of Three Phase Relative permeabilities Using Three Immiscible Liquids, Proceedings of the SPE Annual Meeting, pp 325-338, Houston, Texas, October 1988.

Hagoort J.: Oil Recovery by Gravity Drainge, *SPEJ*, pp 139-150, June 1980.

Hicks P.J., NaRayanan K. R., and Deans H.A.: An Experimental Study of Miscible Displacements in Heterogeneous Cabonate Cores Using X-Ray CT. *SPEFE*, March 1994.

Hove A.O., Ringin J.K., and Read P.A.: Visualization of Laboratory Corefloods with the Aid of Computed Tomography. SPE 13654, Proceedings of the SPE California Regional Meeting, held in Bakersfield, California, 27-29 March 1985.

Hove A.O., Nilsen V., and Leknes J.: Visualization of Xanthan Flood Behavior in Core Samples by Means of X-Ray Tomography, *SPEFE*, November 1990.

Jasti J.K., Jesion G., and Feldkmap L.: Microscopic Imaging of Porous Media with X-ray Computer Tomography, *SPEFE*, September 1993.

Jennings J.W., McGregor D.S., and Morse R.A.: Simultaneous Determination of Capillary Pressure and Relative Permeability by History Matching, SPE 14418, *SPEFE*, pp 322-328, June 1988.

Johnson E.F., Bossler B.P., and Naumann V.O.: Calculations of Relative Permeability from Displacement Experiment, TRANS. AIME, 216, pp 370-372, 1959.

Kantzas A.: Investigation of Physical Properties of Porous Rocks and Fluid Flow Phenomena in Porous Media Using Computed Assisted Tomography, *In Situ*, 14(1), pp 77-132, 1990.

Karpyn Z.: Counter-Current Flow In Porous Media at Residual Wetting Phase Saturation: Experiments and Analysis, MS thesis, The Pennsylvania State University, University Park, Pennsylvania, 2001.

Kerig P.D., and Watson A.T.: A New Algorithm for Estimating Relative Permeabilities From the Displacement Experiments, *SPERE*, pp 103-112, February 1987.

Killough J.E.: "Reservoir Simulation with History-Dependent Saturation Functions," *SPEJ*, February 1976.

King R.L., Stiles J.H.Jr., and Waggoner J.M.: A Reservoir Study of the Kawkins WoodbineField, SPE 2972, Proceedings of the SPE Annual Meeting, Houston, 4-7 October 1970.

Kleppe J., Delaplace, P., Lenormand R., Hamon G., and Chaput E.: "Representation of Capillary Pressure Hysteresis in Reservoir Simulation," SPE 38899, Proceedings

of the SPE Annual Technical Conference and Exhibition, San Antonio, Texas, U.S.A., 5-8 October 1997.

Kruger W.D.: Determining Areal Permeability Distribution by Calculations, *JPT,* pp 691-96, June 1961.

Lenormand R., Kalaydjin F., Bieber M.T., and Lombard J.M.: Use of a Multifractal Approach for Multiphase flow in Heterogeneous Porous Media: Comparision with CT-Scanning Experiment. SPE 20475, Proceedings of the SPE Annual Technical Conference and Exhibition, New Orleans, LA, 23-26 September 1990.

Leverett M.C.: Capillary Behavior in Porous Solids, TRANS. AIME, 1941.

Liu D., Castanier L.M. and Brigham W.E.: Analysis of Transient Foam Flow in 1D Porous Media with CT, SPE 20071, Proceedings of the 60th California Regional Meeting Ventura, California, 4-6 April 1990.

MacMillan D.J.: Automatic History Matching of Laboratory Corefloods to Obtain Relative-Permeability Curves, *SPERE,* pp 85-91, February 1987.

Mattax C.C. and Kyte J.R.: Imbibition Oil Recovery from Fractured, Water-Drive Reservoir, *SPEJ*, pp 177-184, June 1962.

Mokrys I. J. and Butler R.M.: The Rise of Interfering Solvent Chambers: Solvent analog Model of Steam-Assisted Gravity Drainage. *JCPT*, Vol32, No.3, March 1993.

Morrow N.R. and Harris C.C.: "Capillary Equilibrium in Porous Materials," *SPEJ*, March 1965.

Morrow N.R.: "Physics and Thermodynamics of Capillary," in "Flow through Porous media" edited by ACS, Washington, D.C., 1970.

Nasr T.N., Law D.H.-S., Golbeck H. and Korpany G.: Counter-current Aspect of the SAGD Process. *JCPT*, Vol 39, No.1, January 2000.

Nordtvedt J.E., Mejia G., Yang P-H and Watson A.T.: Estimation of Capillary Pressure and Relative Permeability Functions From Centrifuge Experiments, *SPERE*, pp 292-298, November 1993.

Philip J.R.: Similarity Hypothesis for Capillary Hysteresis in Porous Materials. *J. of Geophysiscal Research*, Vol 69, No 8, 1964.

Pirson S.J.: Oil Reservoir Engineering, McGraw Hill Book Company Inc., 1958.

Poulovassilis A.: Hysteresis of Pore Water, an Application of the Concept of Independent Domains. *Soil Sci.* Vol. 93, pp 405, 1962.

Richardson J.G., Sabgree J.B., and Sneider: Oil Recovery by Gravity Segregation, *JPT,* pp 581-582, June 1989.

Richmond P.C., and Watson A.T.: Estimation of Multiphase Flow Function from Displacement Experiments, (*SPERE,* 1989), SPE 18569, 1988.

Rojas F., Kornhauser I., Felipe C., and Cordero S.: Everett's Sorption Hysteresis Domain Theory Revisited from the Point of View of the Dual Site-Bond Model of Disordered Media, *J. of Molecular Catalysis A: Chemical*, Vol 167, pp141-155, 2001.

Romero C.E., Carter J.N., Zimmerman R.W., and Gringarten A.C.: Improved Reservoir Characterization through Evolutionary Computation, SPE 62942, Proceedings of the SPE Annual Technical Conference and Exhibition, Dallas, Texas, 1-4 October 2000.

Sheldon J.W., Zondek B. and Cardwell W.T. Jr: One-Dimentional Incompressible, Noncapillary, Two-Phase Fluid Flow in a Porous Medium. TRANS. AIME Vol. 216, pp 290, 1959.

Siddiqui S., Hicks Jr., P.J. and Grader A.S.: Verification of Buckley-Leverett Three-Phase Theory Using Computerized Tomography, *Journal of Petroleum Science and Engineering*, 15, pp 1-21, 1996.

Stone H.L.: Estimation of the Three-Phase Relative Permeability and Residual Oil Data, *JCPT*, Vol. 14, No. 4, October-December 1973.

Tan T.: Representation of Hysteresis in Capillary Pressure for Reservoir Simulation Models, *JCPT,* 29, 4, July-August 1990.

Templeton E.E., Nielsen R.F. and Stahl C.D.: A Study of Gravity Counterflow Segregation, *SPEJ*, pp 185-193, June 1962.

Terwilliger P.L., Welsy L.E., Howard Hall N., Bridges P.M. and Morse R.A.: An Experimental and Theoretical Investigation of Gravity Drainage Performance, TRANS. AIME, 192, pp 285-296, 1951.

van Laarhoven P.J.M. and Aarts E.H.L.: Simulated Annealing: Theory and Applications, D. Reidel Publishing Company, 1987.

Walsh P. and Moon G.M.: An Analysis of Gravity-Dominated, Immiscible Flows in Dipping Reservoir, SPE 21651, Proceedings of the Production Operations Symposium, Oklahoma, 7-9 April 1991.

Wang S.Y., Ayral S.,: Computed-Assisted Tomography for the Observation of Oil Displacement in Porous Media. *SPEJ*, pp 53-55, February 1984.

Washburn phys. Rev. 17 (3) pp 273, 1921.

Watson A.T., Kerig P.D., Richmond P.C., and Tao T-M.: An Improved Method for Estimating Relative Permeability from the Displacement Experiments, SPE 15064, Proceedings of the 56th California Regional Meeting of the Society of Petroleum Engineers, Oakland, CA, 2-4 April 1986.

Welge H. J.: Displacement of Oil from Porous Media by Water and Gas, TRANS. AIME 198, pp 314-316, 1950.

Welge H. J.: A Simplified Method for Computing Oil Recovery by Gas or Water Drive, TRANS. AIME, 195, pp 314-316, 1952.

Wellington S.L. and Vinegar H.J.: CT Studies of Surfactant- Induced CO2 Mobility Control, SPE 14393, Proceedings of the 60th Annual Technical Conference and Exhibition of the Society of Petroleum Engineers, Las Vegas, NV, 22-25 September 1985.

Wellington S.L. and Vinegar H.J.: X-Ray Computerized Tomography, *JPT*. August 1987.

Withjack E.M., Akervoll I.: Computed Studies of 3-D Miscile Displacement Behavior in laboratory Five-Spot Model, SPE 18096, Proceedings of the 63rd Annual Technical Conference and Exhibition of the Society of Petroleum Engineers, Houston, Tx, 2-5 October 1988.

Wu Z.: A Newton-Raphson Iterative Scheme for Integrating Multiphase Production Data into Reservoir Models, SPE 62846, Proceedings of the SPE/AAPG Western Regional Meeting, Long Beach, California, 19-23 June 2000.

Wyckoff R.D., and Botset H.G.: “Flow of Gas Liquid Mixtures through Sand, *Physics*, pp 325, 1936.

Yamamoto J., Satoh T., Ishii H., and Okatsu k.: An Analysis of CO2 WAG Coreflood by Use of X-Ray CT, SPE 38068, Proceedings of the SPE Asia Pacific Oil and Gas Conference, Kuala Lumpur, Malaysia, 14-16 April 1997.

Yang P-H., and Watson A.T.: Automatic History Matching with Variable-Metric Methods, SPE 16977, Proceedings of the 62nd Annual Technical Conference and Exhibition of the Society of Petroleum Engineers, Dallas, TX , 27-30 September 1987.

Yang P-H. and Watson A.T.: A Bayesian Methodology for Estimating Relative Permeability Curves, *SPERE*, pp 259-265, May 1991.

APPENDIX A

The following file (RUN.DATA) is an Eclipse data file, which include six parts: RUNSPEC, GRID, PROPS, REGIONS, SOLUTION, and SUMMARY in sequence.

The RUNSPEC specifies the problem dimensions, phases present and all kinds of switches etc.

GRID gives the geometry of the computational grid, and the properties such as porosity, absolute permeability) for each grid block.

PROPS gives the the tables of the rock and fluid properties as a function of pressure or saturation. Such properties include density, viscosity, relative permeability, capillary pressure etc.

REGIONS option splits the grid blocks into different regions and each region shares some common properties. For history dependent simulation, each grid block is assigned a different capillary pressure curve and relative permeability cure.

SOLUTION specifies the initial conditions of the reservoir including pressure and saturation.

SUMMARY is a part that specifies what data will be written out. The report and the data used in history matching are generated from this section.

RUN.DATA

```
-- ECLipse data file
RUNSPEC                              LAB     14:00 25 MAR 99
THREE PHASE RUN FILE
= NDIVIX NDIVIY NDIVIZ QRDIAL NUMRES QNNC MXAQN MXAQC QPORO QPERM NFSEG
    1   79     79     F     1     F   0     0     F     F     0 /
= OIL WAT GAS DGAS VOIL API PLY BRI NOTRC NWTRC NGTRC MISC GI SOLV SFT
  T   T   T   T    F   F   F   F   0     0     0     F   F   F   F   /
= UNIT CONVENTION
    'LAB  '                          /
= NRPVT NPPVT NTPVT NTROCC QROCKC QRCREV QROCKH QVE2D SURFT MDIFF QCOAL
  100   100   1     1      F      F      F      F      F      F      F /
= NSS NTS DIRK REVK VEOP HYST SCAL SDIR SREV NSEND NTEND 2PT NSMIS NTMIS
 100 6241 F    T    F    F    F    F    T    30     1   F    30    1 /
= NDRXVD NTEQUL NDPRVD QUIESC QTHPRS QREVTH QMOBIL NTTRVD NSTRVD
  100     1    100      F      F      T      F      1     30     /
= NTFIP  QGRAID QINTRP QTDISP NTFREG QTDISK NRFREG NMFIPR NETRAC
   1      F      F      F      0      F      0      1      0     /
= NWMAXZ NCWMAX NGMAXZ NWGMAX MAXLGR MAXCLS MCOARS LSTACK
    0      0      0      0      0      0      0     10    /
= QEXGOP NWFRIC NUPCOL
    F      0      3                    /
= MXMFLO MXMTHP MXMWFR MXMGFR MXMALQ NMMVFT
    0      0      0      0      0      0     /
= MXSFLO MXSTHP NMSVFT
    0      0      0                    /
= NANAQU NCAMAX NIFTBL NRIFTB NSUMMX
    0      0      0      0     3000          /
=   DAY   MONTH  YEAR
    1    'JAN'  2000                   /
= QSOLVE NSTACK QFMTOU QFMTIN QUNOUT QUNINP NGDISK IDYNAM QOPT9P NDMAIN
    T     50     F      F      F      F      0      0      F      1 /

NOECHO

GRID

INCLUDE                              LAB   10:59 24 MAY 95
 'ACTNUM.INP'  /

INCLUDE                              LAB   21:43 10 SEP 98
 'DXV.INP                    ' /

INCLUDE                              LAB   21:46 10 SEP 98
 'DYV.INP                     ' /

INCLUDE                              LAB   21:55 10 SEP 98
 'DZ.INP                     ' /

INCLUDE                              LAB   21:56 10 SEP 98
 'TOPS.INP                    ' /

INCLUDE                              LAB   10:59 24 MAY 95
```

```
 'PERMX.INP'  /

INCLUDE                              LAB   11:00 24 MAY 95
 'PORO.INP'  /

COPY
'PERMX' 'PERMY' /
/

COPY                                 LAB   22:02 10 SEP 98
'PERMY   ' 'PERMZ   ' ,  ,    ,  ,    ,  ,    /
/

MESSAGES
  9* 10000/


OLDTRANR

INIT

RPTGRID                              LAB   14:47 20 JUN 95
   0   0   0   0   0    0   0   0   0   0    0   0   0   0   0
   0   0   0   0   0    0   0   0   0   0    0   0   0   0   0
   0   0   0   0   0    0   0   0   0   0    0   0   0  /


PROPS

DENSITY    1 TABLES   20 P NODES   20 R NODES    LAB     15:55 21 OCT 98
 1.02650  1.03770  0.74160 /

--EHYSTR
-- 0.1 4 1.0 0.1 BOTH RETR DRAIN/

INCLUDE                              LAB   15:24  9 SEP 98
 'PVTO.INP                  ' /

INCLUDE                              LAB   11:25 13 JUN 95
 'PVDG.INP                   ' /

PVTW       1 TABLES   20 P NODES   20 R NODES    LAB     16:00 21 OCT 98
 3.0000000   1.00506   .4000E-04   1.00506    0.00E+00 /

INCLUDE                              LAB   16:02 29 SEP 98
 'SWFN                       ' /

INCLUDE                              LAB   18:46 29 MAY 95
 'SGFN                       ' /

INCLUDE                              LAB   18:46 29 MAY 95
 'SOF3                     ' /

ROCK       1 TABLES   20 P NODES   20 R NODES    LAB     16:06 21 OCT 98
```

```
 3.00000      .4000E-05 /

RPTPROPS                          LAB     16:27 21 OCT 98
  /

REGIONS
INCLUDE
'EQUALS                    ' /

SOLUTION
PRESSURE                          LAB     16:03 21 OCT 98
6241*3.0
/

PBUB                              LAB     16:03 21 OCT 98
6241*3.0
/

INCLUDE                           LAB   00:10 11 SEP 98
 'SWAT.INP                  ' /

INCLUDE                           LAB   00:12 11 SEP 98
 'SGAS.INP                ' /

SUMMARY

RPTONLY

SEPARATE

RUNSUM

RPTSMRY                           LAB   11:30 16 SEP 98
   9   /

SCHEDULE

DRSDT                             LAB   16:07 14 SEP 98
  0.00000000  'ALL ' /

RPTSCHED                          LAB     17:07 30 JUN 99
  'SGAS'  /

TUNING                            LAB   14:25 23 OCT 98
 0.01667  0.01667  0.01667     1*
    1*       1*       1*       1*       1*
/
    1*       1*       1*       1*
    1*       1*       1*       1*
    1*       1*       1*
/
 1*  1*  80  1*  1*  1*     1*       1*       1*       1*
/
```

```
TSTEP                                LAB     15:05 26 MAR 99
 0.3000  0.2000  0.1667  0.13333
 0.2667  0.1833  0.2500  0.21667
/

TUNING                               LAB   14:25 23 OCT 98
 0.167    0.167    0.167      1*
   1*       1*       1*       1*       1*
/
   1*       1*       1*       1*
   1*       1*       1*       1*
   1*       1*       1*
/
 1*  1*  80  1*  1*  1*    1*       1*       1*       1*
/

TSTEP
 1.50  3.0167  2.0833   1.8333  2.100
/

TUNING                               LAB   14:25 23 OCT 98
 10.000   10.000   10.000      1*
   1*       1*       1*       1*       1*
/
   1*       1*       1*       1*
   1*       1*       1*       1*
   1*       1*       1*
/
 1*  1*  80  1*  1*  1*    1*       1*       1*       1*
/

TSTEP
 10.9667   12.000   36.000
/

RPTRST                               LAB   11:21 17 SEP 98
  'BASIC=2'  'POT'  /

END
```

APPENDIX B

The following files are program codes that used for history matching process. work.bat is a C-shell program and it is the center the process. It is work.bat that combine Eclipse and the optimization methods together to proceed the history matching process.

The general idea is the following: work.bat first calls some programs to generate data files (initial guess) for the simulator – Eclipse and then it calls Eclipse. After Eclipse finishes, it extracts data from the output of the simulator and put them into some optimization programs to generate new parameters fro Eclipse. This is called one iteration. Each after each iteration, the saturation distribution from the simulator is compared with the experimental one. The iteration process keeps going till these two saturation distribution matches.

Header.h is a header file that specifies the variables that all the programs need. The use of this header file makes it easy to keep the variables consistent. It is also easy to make changes for these variables.

gen_pcs.c is C program that is used to generate the capillary scanning curves from the capillary pressure hysteresis loop.

gen_krpc.c is C program that is used to generate relative permeability and organize the capillary pressure curves into an input file for Eclipse.

gen_J.c is the optimization program, compare the saturation distribution of the experiments and the one generated by Eclipse and then generate new parameters for the next iteration .

work.bat

```
#!/bin/csh -f

set flag = 0

111:

#Check STOP file
if -e STOP then
  /bin/rm -f STOP
else
endif

#cp cof_init.inp cof.inp
#cp cof.inp data.cof
#cp data.blank data.J
cp data.blank data.dJ
cp data.blank data.dsat

gen_pcs
gen_krpc 99

##############################
#Run Eclipse File
@eclipse RUN
#Extract Saturation Map
cat RUN.PRT | grep "(\*\, " | cut -c14-30  | sed s/\-----/\0.0/g >data.sat1
#Remove Junk files
/bin/rm -f RUN_*.*
/bin/rm -f RUN.DBG
/bin/rm -f RUN.GRID
/bin/rm -f RUN.IN*
/bin/rm -f RUN.R*
/bin/rm -f RUN.S*
##############################

gen_J 99

if -e STOP goto 999

#start outer loop
set count = 10000
while ($count)
```

```
if -e RESTART goto 111

#start inner loop
set icount = 8
set index = 0
while ($icount)
gen_krpc $index

#Run Eclipse File
@eclipse RUN
#Extract Saturation Map
cat RUN.PRT | grep "(\*\, " | cut -c14-30  | sed s/\-----/\0.0/g >data.sat1
#Remove Junk files
/bin/rm -f RUN_*.*
/bin/rm -f RUN.DBG
/bin/rm -f RUN.GRID
/bin/rm -f RUN.IN*
/bin/rm -f RUN.R*
/bin/rm -f RUN.S*

gen_J $index

@ index++
@ icount--
end
#end inner loop

mv cof.inp cof0.inp

gen_cof $count

@ count--

if -e PAUSE set flag = 1
while ($flag)
 if -e PAUSE then
  set flag = 1
 else
  set flag = 0
  break
 endif
end
#end of flag

cp data.blank data.dJ
```

```
cp data.blank data.dsat
gen_krpc 99

##############################
#Run Eclipse File
@eclipse RUN
#Extract Saturation Map
cat RUN.PRT | grep "(\*\, " | cut -c14-30  | sed s/\-----/\0.0/g >data.sat1
#Remove Junk files
/bin/rm -f RUN_*.*
/bin/rm -f RUN.DBG
/bin/rm -f RUN.GRID
/bin/rm -f RUN.IN*
/bin/rm -f RUN.R*
/bin/rm -f RUN.S*
##############################

gen_J 99

if -e STOP goto 999

end
#end outer loop

999: echo "The program is done!"

echo
```

Header.h

```
#define NZ 79
#define NY 79
#define Ncof 8
#define NT 16
#define NTXNZ 1185
#define NPC 6241
#define step 0.1
#define DELTA 0.0001
#define DELTA_J 0.00001
#define theta 1.0
#define eps 1.0E-9
#define lamda 0.1
#define sor 0.1
#define sgr 0.08
#define swr 0.03
#define sg_tran 0.55
#define N_TRAN 40
#define sh 0.2
```

gen_pcs.c

```
float tbl_lkup(x0,y0,n,x)
int n;
float *x0,*y0;
float x;
{int i,j;
 float y;
 if (x<=x0[0]) y=y0[0];
 else if (x>x0[n-1]) y=y0[n-1];
 else
  for(i=1;i<n;i++)
   {if(x<x0[i])
     {
      y=(y0[i]-y0[i-1])/(x0[i]-x0[i-1])*(x-x0[i-1])+y0[i-1];
      return(y);
     }
    else if (x==x0[i])
     {
      y=y0[i];
      return(y);
     }
   }
}


#include <stdio.h>
#include <math.h>
#include "header.h"

main(argc,argv)
int argc;
char *argv[];
{
  char c;
  int i,j,k,j_hyst,Nsg,TRAN,j_sgi;
  float sg0[100],pcgo01[100],pcgo02[100];
  float sg[100],pcgo[NPC][100],pcgo1[100],pcgo2[100],pcgo3[100];
  float sginit,F,sh3;
  float so,soHYST,soMAX,sgmax,sgi,sgd,sg_s;

  FILE *fpin,*fpout,*fpSWFN,*fpEQUALS;

  Nsg=(int)((1.0-sor-swr-sgr)*100)+1;
```

```
fpin=fopen("pcgo.dat","r");
if(fpin==NULL)
{
  printf("Open file pcgo.dat ERROR !!!\n");
  exit(1);
}

for(i=0;i<32;i++)
  fscanf(fpin,"%f %f %f",&sg0[i],&pcgo02[i],&pcgo01[i]);
fclose(fpin);

sg[0]=sgr;
pcgo1[0]=pcgo01[0];
pcgo2[0]=pcgo02[0];

for(i=1;i<Nsg;i++)
{
 sg[i]=sg[i-1]+0.01;
 pcgo1[i]=tbl_lkup(sg0,pcgo01,32,sg[i]);
 pcgo2[i]=tbl_lkup(sg0,pcgo02,32,sg[i]);
}

fpin=fopen("sginit.txt","r");
if(fpin==NULL)
{
  printf("Open file sginit.txt ERROR !!!\n");
  exit(1);
}

sh3=0.2;
j_hyst=(int)((sg_tran-sgr)*100);
for(j=0;j<=j_hyst;j++)
{
 so=1.0-swr-sg[j];
 soHYST=1.0-swr-sg[j_hyst];
 soMAX=1.0-swr-sgr;
 F=(1.0/(so-soHYST+sh3)-1.0/sh3)/(1.0/(soMAX-soHYST+sh3)-1.0/sh3);
 pcgo3[j]=pcgo1[j]-F*(pcgo1[j]-pcgo2[j]);
}
for(j=j_hyst+1;j<Nsg;j++)
 pcgo3[j]=pcgo1[j];

for(i=0;i<NZ;i++)
 for(k=0;k<NY;k++)
 {
```

```
 fscanf(fpin,"%f",&sginit);
 j_hyst=(int)((sginit-sgr)*100);

 if(sginit<=sg_tran-0.07)
 {
  for(j=0;j<j_hyst;j++)
   pcgo[i*NY+k][j]=pcgo3[j];

  for(j=j_hyst;j<Nsg;j++)
  {
   so=1.0-swr-sg[j];
   soHYST=1.0-swr-sg[j_hyst];
   F=(1.0/(soHYST-so+sh)-1.0/sh)/(1.0/(soHYST-sor+sh)-1.0/sh);
   pcgo[i*NY+k][j]=pcgo3[j]+F*(pcgo1[j]-pcgo3[j]);
  }
 }
 else if(sginit<=sg_tran&&sginit>=sg_tran-0.07)
  {
   for(j=0;j<Nsg;j++)
    pcgo[i*NY+k][j]=pcgo3[j];
  }
 else
 {
  sg_s=tbl_lkup(pcgo2,sg,Nsg,pcgo1[j_hyst]);
  for(j=0;j<j_hyst;j++)
  {
   sgi=sgr+(sg_s-sgr)/(sg[j_hyst]-sgr)*(sg[j]-sgr);
   j_sgi=(int)((sgi-sgr)*100);
   pcgo[i*NY+k][j]=pcgo2[j_sgi];
  }

  for(j=j_hyst;j<Nsg;j++)
   pcgo[i*NY+k][j]=pcgo1[j];
 }
}

fpout=fopen("pcgos.dat","w");
if(fpout==NULL)
{
 printf("Open file pcgos.dat ERROR !!!\n");
 exit(1);
}

/*  for(i=0;i<NZ;i++)
  if(sginit>sg_tran) break;
```

```
fprintf(fpout,"%d \n",i);*/

for(j=0;j<Nsg;j++)
{
 fprintf(fpout,"%5.2f ",sg[j]);
 fprintf(fpout,"%10.7f ",pcgo1[j]);
 for(i=0;i<NPC;i++)
  fprintf(fpout,"%10.7f ",pcgo[i][j]);
 fprintf(fpout,"%10.7f ",pcgo2[j]);
 fprintf(fpout,"\n");
}

fpSWFN=fopen("SWFN","w");
if(fpSWFN==NULL)
{
  printf("Open file SWFN ERROR !!!\n");
  exit(1);
}

fprintf(fpSWFN,"SWFN\n");
for(i=0;i<NPC;i++)
{
 fprintf(fpSWFN,"\n");
 fprintf(fpSWFN,"%f 0.000 1.0\n",swr);
 fprintf(fpSWFN,"%f 1.000 1.0\n",1-sgr-sor);
 fprintf(fpSWFN,"/\n");
}

fpEQUALS=fopen("EQUALS","w");
if(fpEQUALS==NULL)
{
  printf("Open file EQUALS ERROR !!!\n");
  exit(1);
}

fprintf(fpEQUALS,"EQUALS\n");
for(i=0;i<NZ;i++)
 for(j=0;j<NY;j++)
  fprintf(fpEQUALS,"'SATNUM' %d 1 1 %d %d %d  d/\n",i*NY+j+1,j+1,j+1,i+1,i+1);
fprintf(fpEQUALS,"/\n");

fclose(fpin);
fclose(fpout);
fclose(fpSWFN);
}
```

gen_krpc.c

```
#include <stdio.h>
#include <math.h>
#include "header.h"

main(argc,argv)
int argc;
char *argv[];
{
 int i,j,k,n,flag,index,Nsg;
 float a1,b1,c1,d1,a2,b2,c2,d2,temp;
 float sg[100],pcgo[NPC][100];
 float cof[Ncof],kro1[100],krg1[100],kro2[100],krg2[100];
 char c;

 FILE *fpin,*fpSGFN,*fpSOF3,*fp_pcgo;

 Nsg=(int)((1.0-sgr-sor-swr)*100.0)+1;
 sscanf(*++argv,"%d ",&index);

 fpin=fopen("pcgos.dat","r");
 if(fpin==NULL)
 {
  printf("Open file pcgo.dat ERROR !!!\n");
  exit(1);
 }

 for(j=0;j<Nsg;j++)
 {
  fscanf(fpin,"%f ",&sg[j]);
  fscanf(fpin,"%f ",&temp);
  for(i=0;i<NPC;i++)
   fscanf(fpin,"%f ",&pcgo[i][j]);
  fscanf(fpin,"%f ",&temp);
 }

 fpin=fopen("cof.inp","r");
 if(fpin==NULL)
 {
  printf("Open file cof.inp ERROR !!!\n");
  exit(1);
 }
```

```
for(i=0;i<Ncof;i++)
  fscanf(fpin,"%f ",&cof[i]);

if(index<Ncof) cof[index]+=DELTA;

fpSGFN=fopen("SGFN","w");
if(fpSGFN==NULL)
{
  printf("Open file SGFN ERROR !!!\n");
  exit(1);
}

fpSOF3=fopen("SOF3","w");
if(fpSOF3==NULL)
{
  printf("Open file SOF32D ERROR !!!\n");
  exit(1);
}

a1=cof[0];
b1=cof[1];
c1=cof[2];
d1=cof[3];

a2=cof[4];
b2=cof[5];
c2=cof[6];
d2=cof[7];

kro1[0]=a1*pow(1.0-sg[0]-swr-sor,b1);
krg1[0]=0.0;

kro2[0]=a2*pow(1.0-sg[0]-swr-sor,b2);
krg2[0]=0.0;

for(i=1;i<Nsg-1;i++)
{
 kro1[i]=a1*pow(1.0-sg[i]-swr-sor,b1);
 krg1[i]=c1*pow(sg[i]-sgr,d1);

 kro2[i]=a2*pow(1.0-sg[i]-swr-sor,b2);
 krg2[i]=c2*pow(sg[i]-sgr,d2);
}

i=Nsg-1;
```

```
 kro1[i]=0.0;
 krg1[i]=c1*pow(sg[i]-sgr,d1);

 kro2[i]=0.0;
 krg2[i]=c2*pow(sg[i]-sgr,d2);

 fprintf(fpSGFN,"SGFN\n");
 fprintf(fpSOF3,"SOF3\n");

for(i=0;i<=N_TRAN;i++)
 for(k=0;k<NY;k++)
 {
  fprintf(fpSGFN,"\n");
  fprintf(fpSOF3,"\n");

  for(j=0;j<Nsg;j++)
  {
   fprintf(fpSGFN,"%5.3f %10.6f %10.6f\n",sg[j],krg1[j],pcgo[i*NY+k][j]);
   fprintf(fpSOF3,"%5.3f %10.6f %10.6f\n",1.0-swr-sg[Nsg-j-1],   \
                          kro1[Nsg-j-1],kro1[Nsg-j-1]);
  }
  fprintf(fpSGFN,"/\n");
  fprintf(fpSOF3,"/\n");
 }

for(i=N_TRAN+1;i<NZ;i++)
 for(k=0;k<NY;k++)
 {
  fprintf(fpSGFN,"\n");
  fprintf(fpSOF3,"\n");

  for(j=0;j<Nsg;j++)
  {
   fprintf(fpSGFN,"%5.3f %10.6f %10.6f\n",sg[j],krg2[j],pcgo[i*NY+k][j]);
   fprintf(fpSOF3,"%5.3f %10.6f %10.6f\n",1.0-swr-sg[Nsg-j-1],  \
                          kro2[Nsg-j-1],kro2[Nsg-j-1]);
  }
  fprintf(fpSGFN,"/\n");
  fprintf(fpSOF3,"/\n");
 }

 fclose(fpin);
 fclose(fpSGFN);
 fclose(fpSOF3);
}
```

gen_J.c

```
float tbl_lkup(x0,y0,n,x)
int n;
float *x0,*y0;
float x;
{int i,j;
 float y;
 if (x<=x0[0]) y=y0[0];
 else if (x>x0[n-1]) y=y0[n-1];
 else
  for(i=1;i<n;i++)
   {if(x<x0[i])
     {
      y=(y0[i]-y0[i-1])/(x0[i]-x0[i-1])*(x-x0[i-1])+y0[i-1];
      return(y);
     }
    else if (x==x0[i])
     {
      y=y0[i];
      return(y);
     }
   }
}


#include <stdio.h>
#include <math.h>
#include "header.h"

main(argc,argv)
int argc;
char *argv[];
{
  char c;
  int i,j,k,j_hyst,Nsg,TRAN,j_sgi;
  float sg0[100],pcgo01[100],pcgo02[100];
  float sg[100],pcgo[NPC][100],pcgo1[100],pcgo2[100],pcgo3[100];
  float sginit,F,sh3;
  float so,soHYST,soMAX,sgmax,sgi,sgd,sg_s;

  FILE *fpin,*fpout,*fpSWFN,*fpEQUALS;
```

```
Nsg=(int)((1.0-sor-swr-sgr)*100)+1;

fpin=fopen("pcgo.dat","r");
if(fpin==NULL)
{
  printf("Open file pcgo.dat ERROR !!!\n");
  exit(1);
}

for(i=0;i<32;i++)
  fscanf(fpin,"%f %f %f",&sg0[i],&pcgo02[i],&pcgo01[i]);
fclose(fpin);

sg[0]=sgr;
pcgo1[0]=pcgo01[0];
pcgo2[0]=pcgo02[0];

for(i=1;i<Nsg;i++)
{
 sg[i]=sg[i-1]+0.01;
 pcgo1[i]=tbl_lkup(sg0,pcgo01,32,sg[i]);
 pcgo2[i]=tbl_lkup(sg0,pcgo02,32,sg[i]);
}

fpin=fopen("sginit.txt","r");
if(fpin==NULL)
{
  printf("Open file sginit.txt ERROR !!!\n");
  exit(1);
}

sh3=0.2;
j_hyst=(int)((sg_tran-sgr)*100);
for(j=0;j<=j_hyst;j++)
{
 so=1.0-swr-sg[j];
 soHYST=1.0-swr-sg[j_hyst];
 soMAX=1.0-swr-sgr;
 F=(1.0/(so-soHYST+sh3)-1.0/sh3)/(1.0/(soMAX-soHYST+sh3)-1.0/sh3);
 pcgo3[j]=pcgo1[j]-F*(pcgo1[j]-pcgo2[j]);
}
for(j=j_hyst+1;j<Nsg;j++)
 pcgo3[j]=pcgo1[j];

for(i=0;i<NZ;i++)
```

```
for(k=0;k<NY;k++)
{
 fscanf(fpin,"%f",&sginit);
 j_hyst=(int)((sginit-sgr)*100);

 if(sginit<=sg_tran-0.07)
 {
  for(j=0;j<j_hyst;j++)
   pcgo[i*NY+k][j]=pcgo3[j];

  for(j=j_hyst;j<Nsg;j++)
  {
   so=1.0-swr-sg[j];
   soHYST=1.0-swr-sg[j_hyst];
   F=(1.0/(soHYST-so+sh)-1.0/sh)/(1.0/(soHYST-sor+sh)-1.0/sh);
   pcgo[i*NY+k][j]=pcgo3[j]+F*(pcgo1[j]-pcgo3[j]);
  }
 }
 else if(sginit<=sg_tran&&sginit>=sg_tran-0.07)
  {
   for(j=0;j<Nsg;j++)
    pcgo[i*NY+k][j]=pcgo3[j];
  }
 else
 {
  sg_s=tbl_lkup(pcgo2,sg,Nsg,pcgo1[j_hyst]);
  for(j=0;j<j_hyst;j++)
  {
   sgi=sgr+(sg_s-sgr)/(sg[j_hyst]-sgr)*(sg[j]-sgr);
   j_sgi=(int)((sgi-sgr)*100);
   pcgo[i*NY+k][j]=pcgo2[j_sgi];
  }

  for(j=j_hyst;j<Nsg;j++)
   pcgo[i*NY+k][j]=pcgo1[j];
 }
}

fpout=fopen("pcgos.dat","w");
if(fpout==NULL)
{
  printf("Open file pcgos.dat ERROR !!!\n");
  exit(1);
}
```

```
/*  for(i=0;i<NZ;i++)
   if(sginit>sg_tran) break;
  fprintf(fpout,"%d \n",i);*/

  for(j=0;j<Nsg;j++)
  {
   fprintf(fpout,"%5.2f ",sg[j]);
   fprintf(fpout,"%10.7f ",pcgo1[j]);
   for(i=0;i<NPC;i++)
    fprintf(fpout,"%10.7f ",pcgo[i][j]);
   fprintf(fpout,"%10.7f ",pcgo2[j]);
   fprintf(fpout,"\n");
  }

  fpSWFN=fopen("SWFN","w");
  if(fpSWFN==NULL)
  {
    printf("Open file SWFN ERROR !!!\n");
    exit(1);
  }

  fprintf(fpSWFN,"SWFN\n");
  for(i=0;i<NPC;i++)
  {
   fprintf(fpSWFN,"\n");
   fprintf(fpSWFN,"%f 0.000 1.0\n",swr);
   fprintf(fpSWFN,"%f 1.000 1.0\n",1-sgr-sor);
   fprintf(fpSWFN,"/\n");
  }

  fpEQUALS=fopen("EQUALS","w");
  if(fpEQUALS==NULL)
  {
    printf("Open file EQUALS ERROR !!!\n");
    exit(1);
  }

  fprintf(fpEQUALS,"EQUALS\n");
  for(i=0;i<NZ;i++)
   for(j=0;j<NY;j++)
    fprintf(fpEQUALS,"'SATNUM' %d 1 1 %d %d %d
%d/\n",i*NY+j+1,j+1,j+1,i+1,i+1);
  fprintf(fpEQUALS,"/\n");

  fclose(fpin);
```

```
  fclose(fpout);
  fclose(fpSWFN);
}
```

Vita

Gaoming Li Born in ShanDong province, China. He got his BS and MS from The University of Petroleum, China, in 1996 and 1999, respectively. During his college life, he earned several scholarships including National Science and Technology Scholarship, Sun Engineering Scholarship, Offshore Well Logging Company Scholarship etc. His team won the third place in a National Applied Mathematical Modeling Contest (ShanDong Section). In the graduate school of the University of Petroleum, he actively participated several team projects. In August 1999, he came to the Pennsylvania State University, and started his Ph.D. study in Petroleum and Natural Gas Engineering.